



Sudan University of Science and Technology
College of Graduate Studies

**Characterization of White Matter Lesions on Brain
Magnetic Resonance Images Using Texture Analysis**

توصيف اصابات النسيج الأبيض في صور الرنين المغنطيسي للمخ
باستخدام التحليل الملمسي

*Thesis Submitted in Fulfillment of Requirements for Ph.D. Degree in
Diagnostic Radiological Imaging*

By:

Sarah Suliman Mohammed Elhassan

Supervisor:

Prof. Dr. Mohammed Elfadil Mohammed

2021

الآية

بِسْمِ اللّٰهِ الرَّحْمٰنِ الرَّحِیْمِ
﴿وَقُلْ رَبِّ زِدْنِي عِلْمًا﴾

صدق الله العظيم

(سورة طه الآية: 144)

DEDICATION

WITH MY LOVE AND APPRECIATION I DEDICATE THIS

THESIS TO:

My grandmother soul.

My father MR: **SULIMAN ALERAGI.**

My mother MRS: **EIGBAL MOBARAK.**

My sisters: **TAYSEER & AMNA.**

My brothers: **MAHMOUD & MOHAMMED.**

All my friends, family and to all people those I love and respect.

Acknowledgements

Firstly and always thanks Allah. Secondly great thanks to our supervisor prof. Mohammed Elfadil Mohammed for his great efforts that he made to finish this research successfully.

Many thanks extend to the Antalya medical center staff for their help and support.

Finally, thanks for all those who helped me in the preparation of this thesis specially Mr. Mohammed Suliman .

Abstract

Texture analysis studies have been increasingly explored in neuroradiology in the recent years, as it enabling diseases characterization and quantification of disease distribution. The aim of this study was to characterize white matter lesions on the brain in MR images using texture analysis. This analytical study had been conducted at Antalya medical center in the period from October 2018 to March 2021 by using study of 1646 brain MR images selected conveniently for patients having Glioma, Multiple Sclerosis (MS) and Small Vessels Diseases (SVD) , then these images entered to interactive data language program to extract the textural features from the normal tissues and the white matter lesions, then these extracted features entered to statistical package social science for analysis. And the results reveal that; the best textural features for discrimination of the Glioma from the normal tissues in all MR imaging sequences were the mean, entropy, Gray-Level Nonuniformity and Run-Length Nonuniformity. While for the MS plaques the features were the mean, variance, entropy and Run Percentage textural features. Also the best features for differentiation the SVD from normal tissues in all MRI sequences were the mean, variance, energy, entropy, Gray-Level Nonuniformity and Run Percentage. In conclusion texture analysis statistics successfully discriminate the white matter lesions from normal brain tissues in all MRI sequences, firstly when using the first order statistics on the Glioma, MS and SVD the imaging sequence that shows the highest sensitivity in discrimination the lesion from normal tissues were T2=98.2%, T1+C=99.3% and T1+C=97.5% respectively; and when using the higher order statistics the highest sensitivity were in T1+C=93.6%, T1+C=99.3% and T1=97.5% correspondingly.

المستخلص

تم استخدام دراسات تحليل الملمسي بشكل متزايد في الصور الاشعاعية للجهاز العصبي في السنوات الأخيرة ، حيث إنها تتيح توصيف الامراض والتقدير الكمي للأمراض. كان الهدف من هذه الدراسة هو توصيف أمراض النسيج الابيض في المخ في صور الرنين المغنطيسي باستخدام التحليل الملمسي . أجريت هذه الدراسة التحليلية في مركز أنطاليا الطبي في الفترة من أكتوبر 2018 إلى مارس 2021, في عينة تتكون من 1646 صورة رنين مغنطيسي للدماغ تم اختيارها بشكل ملائم من مرضى لديهم ورم الدبقي, التصلب المتعدد و أمراض الأوعية الدموية الصغيرة ، تم إدخال هذه الصور في برنامج لغة البيانات التفاعلية لاستخراج السمات التركيبية من الأنسجة الطبيعية و أمراض المادة البيضاء ، ثم أدخلت هذه القرائات المستخرجة إلى برنامج الحزمه الاحصائيه للعلوم الاجتماعيه لتحليلها. ولقد أوضحت النتائج أن أفضل الميزات التركيبية للتمييز بين الورم الدبقي من الأنسجة الطبيعية في جميع انواع صور الرنين المغنطيسي هي الوسط ، الانتروبيا ، عدم اتساق اترج الرامادي و عدم اتساق ميل المدى. بينما بالنسبة للتصلب المتعدد ، كانت الميزات هي الوسط ، التباين ، الانتروبيا و النسبة المئوية للمدى. كما أن أفضل ميزات لتفريق أمراض الأوعية الدموية الصغيرة عن الأنسجة الطبيعية في جميع انواع صور الرنين المغنطيسي هي المتوسط ، التباين ، الطاقة ، الانتروبيا ، عدم اتساق اترج الرامادي و النسبة المئوية للمدى. اذا نجحت إحصائيات تحليل النسيج في التمييز بين امراض النسيج الابيض من أنسجة المخ الطبيعية في جميع تسلسلات التصوير بالرنين المغنطيسي ، أولاً عند استخدام إحصائيات الدرجة الأولى على الورم الدبقي والتصلب المتعدد و أمراض الأوعية الدموية الصغيرة, نوع صور الرنين المغنطيسي الذي يظهر أعلى حساسية في التمييز بين الامراض و الأنسجة السليمة هو $T2=98,2\%$ ، $T1+C=99,3\%$ و $T1+C=97,5\%$ على التوالي ؛ وعند استخدام إحصائيات الرتبة الأعلى ، كانت أعلى حساسية في $T1+C=93,6\%$ ، $T1+C=99,3\%$ و $T1=97,5\%$ على التوالي.

Table of contents

Contents	Pages
الأية	I
Dedication	II
Acknowledgement	III
Abstract	IV
Abstract in Arabic	V
Table of Contents	VI
List of Abbreviations	VIII
Chapter One	
1.1 Introduction	1
1.2 Problem of the study	2
1.3 Objectives	2
1.4 Significance of the study	3
1.5. Overview of the study	3
Chapter Two	
2.1 Anatomy	4
2.2 Physiology of the nervous system	16
2.3 Pathology that characterized on this thesis	17
2.4 MRI physics	22
2.5 MRI Techniques	29
2.7 Texture analysis	32
2.8 Previous studies	35

Chapter Three	
3.1 Materials	42
3.1.1 Study design	42
3.1.2 Study area and duration	42
3.1.3 Study population ³	42
3.1.4 Sample size and type	42
3.1.5 Equipment and software programs used in the study	42
3.2 Method of data collection and analysis	43
3.3 Ethical considerations	44
Chapter Four	
4. Results	45
Chapter Five	
5.1 Discussion	79
5.2 Conclusion	88
5.3 Recommendations	90
References	91
Appendices	95

List of Abbreviations

Abbreviation	Means
1H	Hydrogen
ADEM	Acute Disseminated Encephalomyelitis
ANN	Artificial Neural Network
B0	the magnetic field strength
CE	Contrast Enhanced
CIS	Clinical Isolated Syndrome
CNS	Central Nerves System
CSF	Cerebro Spinal Fluid
CT	Computed Tomography
DICOM	Digital Imaging And Communication In Medicine
EDSS	Expanded Disability Status Scale
EPI	Echo Planer Imaging
FLAIR	Fluid Attenuation Inversion Recovery
FSE	Fast Spin Echo
GLCM	Gray-Level Co-Occurrence Matrix
GLN	Gray-Level Nonuniformity
GLRLM	Gray-Level Run-Length Matrix
GRE	Gradient Echo
HGRE	High Gray-Level Run Emphasis
HN	Histogram Normalization
IDL	Interactive Data Language
LDA	Linear Discriminant Analysis
LGRE	Low Gray-Level Run Emphasis
LR	Logistic Regression
LRE	Long Run Emphasis
LRHGE	Long Run High Gray-Level Emphasis
LRLGE	Long Run Low Gray-Level Emphasis
LWM	Lesion White Matter
MHz	Mega Hertz
MRI	Magnetic Resonance Imaging
MS	Multiple Sclerosis
Mz	Magnetization
NAWM	Normal Appearing White Matter
NWM	Normal White Matter
PCA	Patient –Controlled Analgesia
PD	Proton Density

RF	Radio Frequency
RLN	Run-Length Nonuniformity
ROC	Receiver operating characteristic
ROI	Region Of Interest
RP	Run Percentage
SE	Spin Echo
SPSS	Statistical Package Social Science
SRE	Short Run Emphasis
SRLGE	Short Run Low Gray-Level Emphasis
SRHGE	Short Run High Gray-Level Emphasis
SS	Single Shot
SVD	Small Vessels Diseases
SVM	Support Vector Machines
T1	T1-weighted MR Imaging
T1+C	T1-weighted with contrast MR Imaging
T2	T2-weighted MR Imaging
TIFF	Tagged Image File Format

Chapter One

Introduction

1.1 Introduction

The white matter of the brain composed of tracts, which consists of bundles of myelinated axons which wrapped in a myelin sheath; a fatty substance having a creamy white color (Forbes, 2017).

There are many potential causes of white matter diseases (hyperintensities) including ischemic, inflammatory, demyelinating, infectious, metabolic, toxic and malignant (Forbes, 2017).

Neuroradiology, specially magnetic resonance imaging (MRI) helps in the detecting and diagnosis of the brain lesions, as it offers different types of images according to different physical factors and tissue characteristics e.g: T1-weighted, T2-weighted and fluid attenuation inversion recovery (FLAIR) sequences, also it provide a good soft tissue differentiation and resolution (Forbes, 2017) and (Kornienko and Pronin, 2008).

These imaging protocols can be directed to assess the white matter and assist in narrowing the differential diagnosis which is wide and depends on location, appearance and changes over time, which is detected by the Radiologist (Nicolae, 2016). It also can be evaluated using Texture analysis methods which enabling disease characterization and quantification of disease distribution, these techniques may provide information that is not visible to human eye (Alastair, 2002).

The aim of this thesis is to characterize white matter lesions in MR images by using texture analysis, as texture analysis studies have been produced more often the recent years on central nerves system lesions as it give a quantitative result (Kornienko and Pronin, 2008).

1.2 Problem of the study:

Generally in radiology the pathology or any abnormality will be diagnosed by the radiologist, as abnormal area depending on their visual perception which is subjective and affected by many factors. This situation may lead some times not giving an efficient diagnosis for diseases that appears alike in the white matter of the brain. Therefore texture analysis can provide second opinion for the radiologist to diagnose white matter pathologies, with some confidence as well as it will draw his attention to the area of interest.

1.3 Objectives:

1.3.1 General objective:

The general objective of this study is to characterize white matter lesions in MR images using texture analysis.

1.3.2 Specific objectives:

- To extract texture feature for the white matter and the grey matter from MR images using first and higher order statistics.
- To extract texture feature for each lesion (Glioma, Multiple Sclerosis (MS) and Small Vessels Diseases (SVD)) from MR images using first and higher order statistics.
- To classify the extracted feature for each pathology into two classes including normal white matter, grey matter and the lesion using K-means through Euclidian distance.
- To generate a classification map from the classified features.
- To apply linear discriminate analysis to generate model for linear classification on MR Images .
- To calculate the sensitivity and accuracy for each pathology .
- To use to discriminate analysis in differentiation between all diseases included on this study on the MR images .

1.4 Significance of the study:

This study is to highlight the application of image analysis, using image processing techniques, in characterizing white matter pathologies on MR images, and hence it will facilitate quantitative approach in brain defect.

1.5 Overview of the study:

This study consists of five chapters. Chapter one is an introduction as well as statement of the problem and study objectives and significance of the study. Chapter two include literature review ,and anatomical background and previous studies. Chapter three deals with the methodology, where it provides an outline of material and methods used to acquire the data in this study, as well as the method of analysis approach. chapter four deal with the results presentaion, and finally Chapter five includes discussion of the results, conclusion and recommendations followed by references and appendices.

Chapter Two

Literature Review

2.1 Anatomy:

Anatomy of the nervous system:

The divisions of the nervous system can be classified by location or by the type of tissue supplied by the nerve cells in the division. The central nervous system (CNS) consists of the brain and spinal cord. The remaining neural structures, including 12 pairs of cranial nerves, 31 pairs of spinal nerves, autonomic nerves, and ganglia, make up the peripheral nervous system (PNS). The PNS consists of afferent and efferent neurons. Afferent (sensory) neurons conduct impulses from peripheral receptors to the CNS. Efferent (motor) neurons conduct impulses away from the CNS to the peripheral effectors (Eisenberg and Johnson, 2016). The somatic nervous system supplies the striated skeletal muscles, whereas the autonomic nervous system supplies smooth muscle, cardiac muscle, and glandular epithelial tissue (Eisenberg and Johnson, 2016).

2.1.1 Neuron:

Neurons, or nerve cells, are the specialized cells of the nervous system that conduct electrical impulses. Each neuron is composed of an axon, a cell body, and one or more dendrites (Bontrager, 2014).

Dendrites are processes that conduct impulses toward the neuron cell body. An axon is a process that leads away from the cell body. The dendrites and cell bodies make up the gray matter of the brain and spinal cord, and the large myelinated axons make up the white matter (Bontrager, 2014).

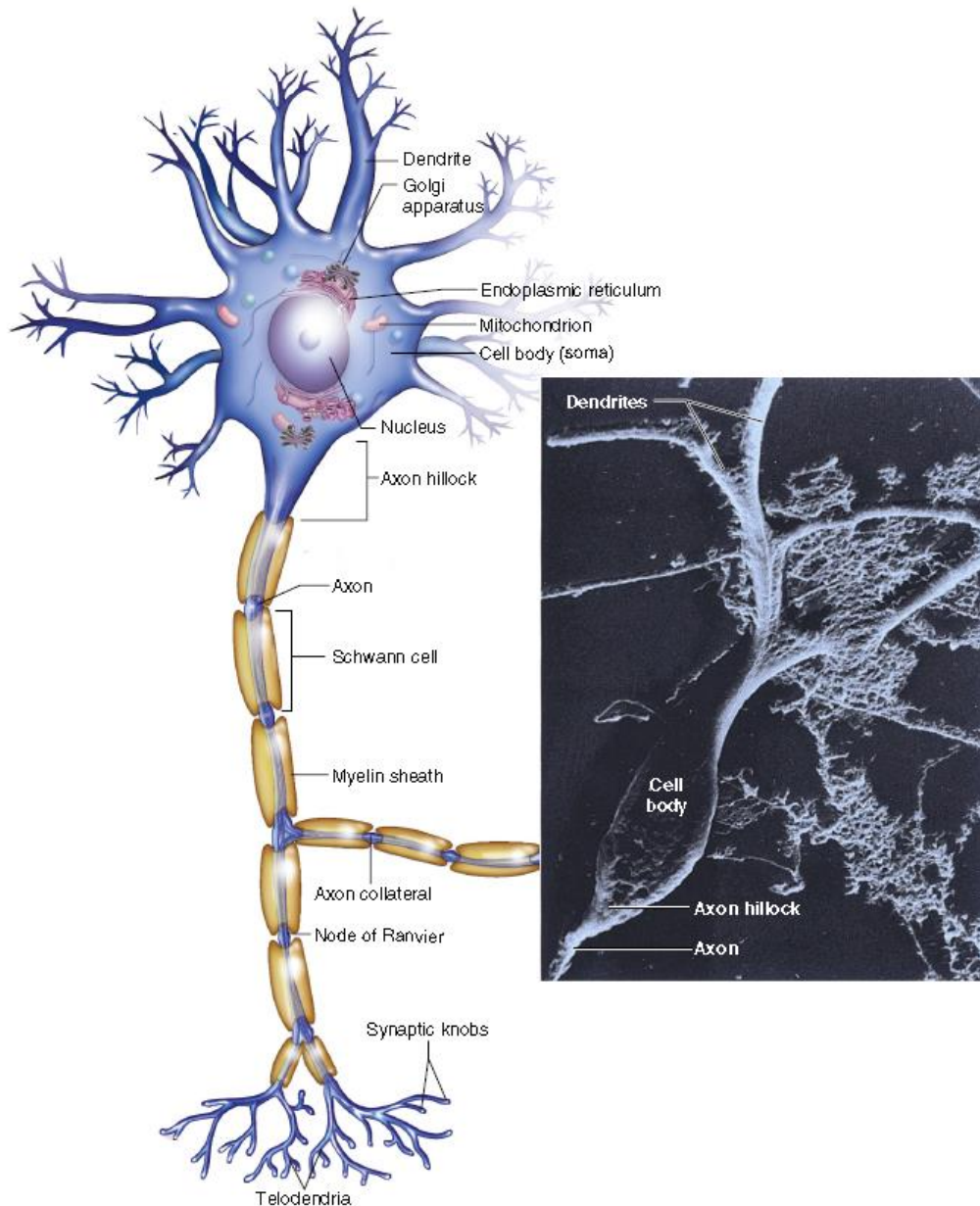


Fig (2-1): the Neuron (Eisenberg and Johnson, 2016).

2.1.2 Cerebral hemispheres:

The cerebral hemispheres fill the cranial vault above the tentorium cerebelli. Right and left hemispheres are connected by the corpus callosum and are otherwise partly separated by the median longitudinal fissure. The hemispheres consist of cortical grey matter, white matter, basal ganglia, thalamus, hypothalamus, pituitary gland and the limbic lobe. The lateral ventricles form a cavity within each ventricle (Stephanie et al, 2011).

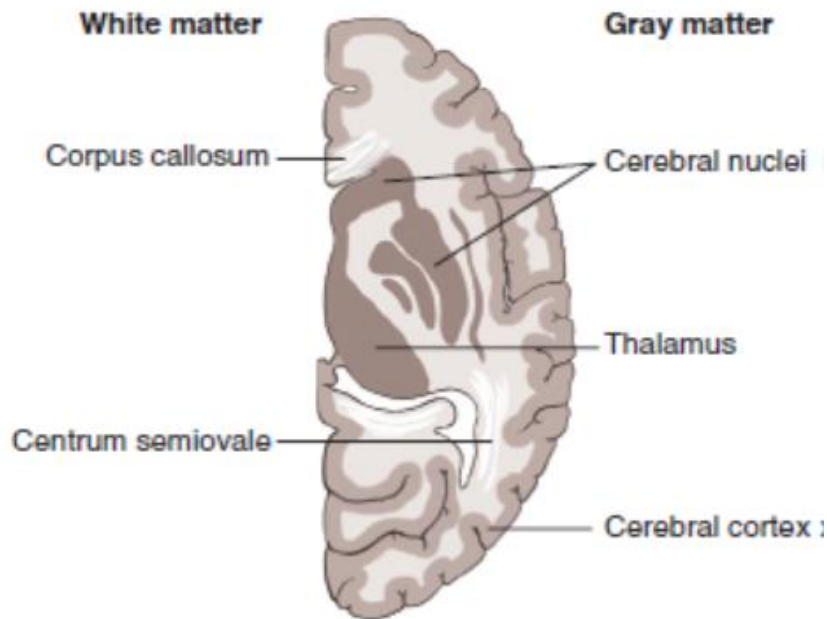


Fig (2-2): A section of brain tissue through the cerebral hemispheres (Bontrager, 2014).

2.1.2.1 Cerebral cortex:

The superolateral surface of each cerebral hemisphere has two deep sulci; these are:

The lateral sulcus, also known as the sylvian fissure, which separates the frontal and temporal lobes (Stephanie et al, 2011).

The central sulcus (of Rolando), which passes upwards from the lateral sulcus to the superior border of the hemisphere. This separates the frontal and parietal lobes (Stephanie et al, 2011).

The parieto-occipital sulcus on the medial surface of the hemisphere separates the parietal and occipital lobes. On the lateral surface of the hemispheres there is no complete sulcal separation of the parietal, temporal and occipital lobes. The boundary between the parietal and temporal lobes lies on a line extended back from the lateral sulcus. The boundary separating the parietal and temporal lobes from the occipital

lobe is a line between the superior border of the parieto-occipital sulcus and the preoccipital notch (Stephanie et al, 2011).

2.1.2.1.1 Grey Matter Structures:

The cerebral cortex itself consists of arrays of neurons (estimated to number 100 billion, each one communicating synaptically with many adjacent neurons in a system of astonishing complexity) which on Nissl staining appear to be arranged in layers. The cortex varies from 2 to 5 mm in thickness (Andreas et al, 2015).

Isocortex, as described above, has six layers, allocortex has three, with mesocortex in between, all layers being numbered from superficial to deep. Probably, equal numbers of glial cells are present in the cortex, interacting metabolically with neurons and synapses as well as with the rich network of cortical capillaries. Precise functions of glial cells are not clear-cut, but they are certainly not mere supporting cells. The surface of the cortex is formed by a continuous layer of superficial astrocyte foot processes with associated basement membrane forming the glia limitans to which is applied the pia mater, with a potential subpial space intervening (Andreas et al, 2015).

The cortical mantle over the surface of each hemisphere is folded into a series of elevated gyri separated by sulcal clefts. These form the basis of the separation into the lobes of the brain, which were originally named for the overlying skull bones. The lobar terminology represents a convenient though arbitrary system and is largely devoid of onto-genic significance. Six lobes in each hemisphere are often described: frontal, parietal, occipital, temporal, insula and limbic. With familiarity, patterns emerge from the initially bewildering array of brain convolutions allowing quite accurate identification of the major subdivisions. The inter-hemispheric fissure and Sylvian (or lateral) fissure are immediately obvious. The central sulcus is the other main landmark of the hemisphere

separating the precentral gyrus (motor) from the postcentral gyrus (sensory) and can usually be confidently identified on axial and sagittal images. From these landmarks other sulci and gyri can be sequentially identified (Andreas et al, 2015).

The deep grey matter structures principally comprise the basal ganglia, amygdala and thalamus. The basal ganglia are part of the extrapyramidal system including the caudate nucleus, globus pallidus, putamen, nucleus accumbens and substantia nigra. The globus pallidus and caudate are linked across the intervening internal capsule by a series of grey matter bridges giving a striated appearance, the origin of the term corpus striatum for this region (Andreas et al, 2015).

The thalami are paired large nuclear masses forming most of the lateral walls of the third ventricle, above and behind the hypothalamus. They often are in contact across the ventricle at the massa intermedia. The posterior border, or pulvinar, bulges convexly into the quadrigeminal cistern and overlies the medial (visual) and lateral (olfactory) geniculate bodies (Andreas et al, 2015).

2.1.2.2 White Matter:

The anatomy of the white matter of the brain has generally received little attention in the imaging literature, which is surprising given the ubiquity of white matter diseases. The medullary core of the brain is formed of bundles of axons, supporting glial cells and penetrating blood vessels. Its whitish color derives from the fatty myelin sheaths contributed by oligodendrocytes (in the periphery myelin sheaths are formed by Schwann cells) (Andreas et al, 2015).

The myelin sheath is produced by oligodendrocytes and is the component responsible for the color and the imaging characteristics of normal white matter. Myelin has a water content of about 40%, and the dry part (60%) is mainly composed of lipids (70%–85%), with a smaller

component of proteins (15%– 30%). Spinal cord myelin has an even higher lipid-to-protein ratio than the brain. The major lipid components of myelin are cerebrosides and lecithin, and the main protein elements of myelin are proteolipid protein and myelin basic protein, which are more specific to the central nervous system and may serve as antigenic targets in autoimmune processes. For the same reason, another important protein component is myelin oligodendrocyte glycoprotein, which is involved in the formation and maintenance of myelin sheaths and is located in the outermost layer of myelin, serving as a potential target for autoimmunity (Nicolae et al, 2016).

2.1.2.2.1 White matter Structures:

There are three types of fiber within the cerebral hemispheres: commissural fibers, which connect corresponding areas of the two hemispheres; association (arcuate) fibers, which connect different parts of the cortex of the same hemisphere; and projection fibers, which join the cortex to lower centers (Ryan et al, 2011).

2.1.2.2.1.1 Commissural fibers:

The corpus callosum is a large midline mass of commissural fibers, each of which connects corresponding areas of both hemispheres. It is approximately 10 cm long and becomes progressively thicker towards its posterior end. Named parts include the following:

Rostrum – this is the first part, which extends anteriorly from the anterior commissure (Ryan et al, 2011).

Genu – this is the most anterior part where it bends sharply backwards.

Trunk (body) – this is the main mass of fibers extending from the genu anteriorly to the splenium posteriorly. It lies below the lower free edge of the falx cerebri. The anterior cerebral vessels run on its superior surface.

Splenium – this is the thickened posterior end (Ryan et al, 2011).

In cross-section, fibers from the genu that arch forward to the frontal cortex on each side are called **forceps minor**, and fibers from the splenium passing posteriorly to each occipital cortex are called **forceps major**. Fibers extending laterally from the body of the corpus callosum are called the **tapetum**. These form part of the roof and lateral wall of the lateral ventricle (Ryan et al, 2011).

Anterior commissure: this is a bundle of fibers in the lamina terminalis in the anterior wall of the third ventricle. The fibers pass laterally in an arc indenting the inferior surface of the globus pallidus. The anterior commissure is part of the olfactory system and connects the olfactory bulbs, the cortex of the anterior perforated substance and the piriform areas (Ryan et al, 2011).

Habenular commissure: This small commissure is situated above and anterior to the pineal body it unites the habenular striae, which are fibers from the olfactory center that pass posteriorly along the upper surface of each thalamus and unite in a 'U' configuration in this commissure (Ryan et al, 2011).

Posterior commissure: This is situated anterior and inferior to the pineal body, it connects the superior colliculi, which are concerned with light reflexes (Ryan et al, 2011).

Hippocampal commissure: This is the commissure of the fornix (Ryan et al, 2011).

2.1.2.2.1.2 Projection fibers:

These fibers join the cerebral cortex to lower centers, Some are afferent and some efferent, They are called the internal capsule, where they lie lateral to the thalamus and the corona radiata as they fan out between the internal capsule and the cerebral cortex (Ryan et al, 2011).

Internal capsule ;This contains sensory fibers from the thalamus to the sensory cortex and motor fibers from the motor cortex to motor nuclei in

the brainstem, corticobulbar tracts and, in the spinal cord, the corticospinal (pyramidal) tracts In cross-section, the internal capsule has an anterior limb between the caudate and lentiform nuclei and a posterior limb between the lentiform nucleus and the thalamus, Both limbs meet at a right-angle called the genu, The anterior limb is composed mainly of frontopontine fibers, The genu and the anterior two-thirds of the posterior limb contain motor fibers, The most anterior fibers at the genu are those of the head Fibers to the arm, hand, trunk, leg and perineum lie progressively more posteriorly, Behind these fibers on the posterior limb and on the retro lentiform part of the internal capsule are parietopontine and occipitopontine fibers and the sensory fibers More posteriorly are the visual fibers that extend towards the occipital pole as the optic radiation Most posterior of all are the auditory fibers (Ryan et al, 2011).

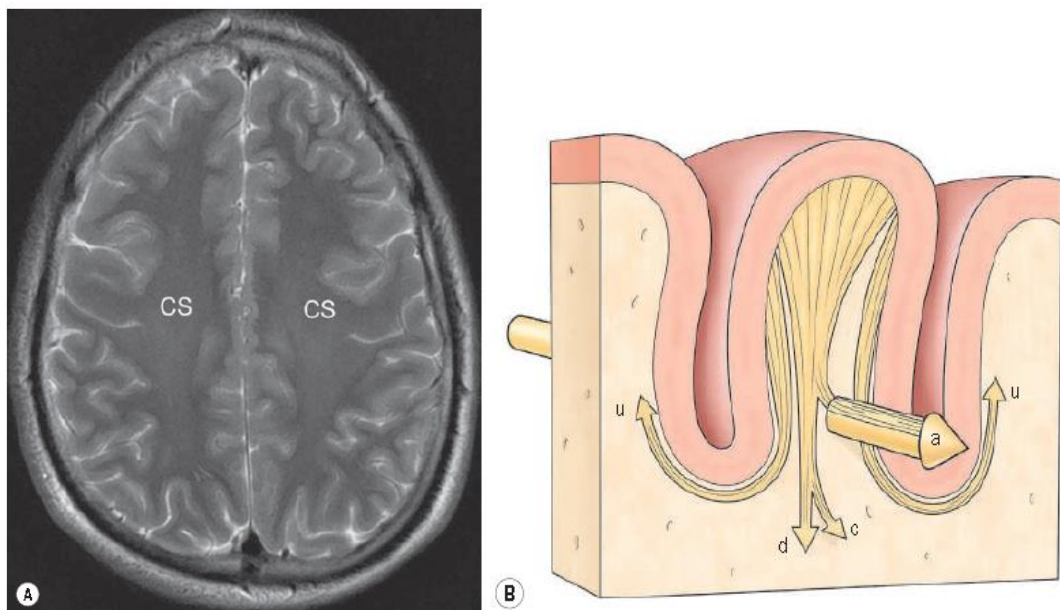


Fig (2-3): (A) Axial T2 MRI demonstrates the white matter core of the cerebral hemispheres, the centrum semi-ovale (CS). (B) Schematic demonstrating the several types of white matter tract: subcortical U-fibers (u), ascending/ descending tracts (d), association tracts (a) and commissural tracts (c) (Andreas et al, 2015).

2.1.3 Arterial Supply and venous drainage:

2.1.3.1 Arterial Supply:

The brain receives arterial blood from two main pair of vessels and their branches, the internal carotid arteries and the vertebral arteries. Many normal variations of the arterial blood supply exist (Kelley, 2007).

The Internal Carotid Arteries supply the frontal, parietal, and temporal lobes of the brain and orbital structures. These arteries arise from the bifurcation of the carotid arteries in the neck. The internal carotid artery then turns forward within the cavernous sinus, then up and backward through the dura mater, forming an S shape (carotid siphon) before it reaches the base of the brain. As the internal carotid artery exits the cavernous sinus, it branches into the ophthalmic artery just inferior to the anterior clinoid process. The internal carotid artery then runs lateral to the optic chiasm and branches into the anterior cerebral artery and the larger middle cerebral artery. The anterior cerebral artery and its branches supply the anterior frontal lobe and the medial aspect of the parietal lobe. The middle cerebral artery is by far the largest of the cerebral arteries and is considered a direct continuation of the internal carotid artery. The middle cerebral artery gives off many branches, as it supplies much of the lateral surface of the cerebrum, insula, and anterior and lateral aspects of temporal lobe; nearly all the basal ganglia; and the posterior and anterior internal capsule (Kelley, 2007).

Vertebral Arteries The vertebral arteries begin in the neck at the subclavian artery and ascend vertically through the transverse foramina of the cervical spine. The vertebral arteries curve around the atlanto-occipital joints to enter the cranium through the foramen magnum. The two vertebral arteries unite ventral to the pons, to form the basilar artery. The vertebral and basilar arteries give rise to several pairs of smaller arteries that supply the cerebellum, pons, and inferior and medial

surfaces of the temporal and occipital lobes. The four major pairs of arteries are listed in order from inferior to superior: posterior inferior cerebellar, anterior inferior cerebellar, superior cerebellar and posterior cerebral. The posterior cerebral arteries can be divided into three major segments: precommunicating or peduncular (P1), ambient (P2), and quadrigeminal (P3). The posterior communicating artery forms a connection between the posterior cerebral artery and the internal carotid artery (Kelley, 2007).

Circle of Willis: The cerebral arterial circle, or circle of Willis, is a critically important anastomosis among the four major arteries (two vertebral and two internal carotid) feeding the brain. The circle of Willis is formed by the anterior and posterior cerebral, anterior and posterior communicating, and the internal carotid arteries. The circle is located mainly in the suprasellar cistern at the base of the brain. Many normal variations of this circle may occur in individuals. The circle of Willis functions as a means of collateral blood flow from one cerebral hemisphere to another in the event of blockage (Kelley, 2007).

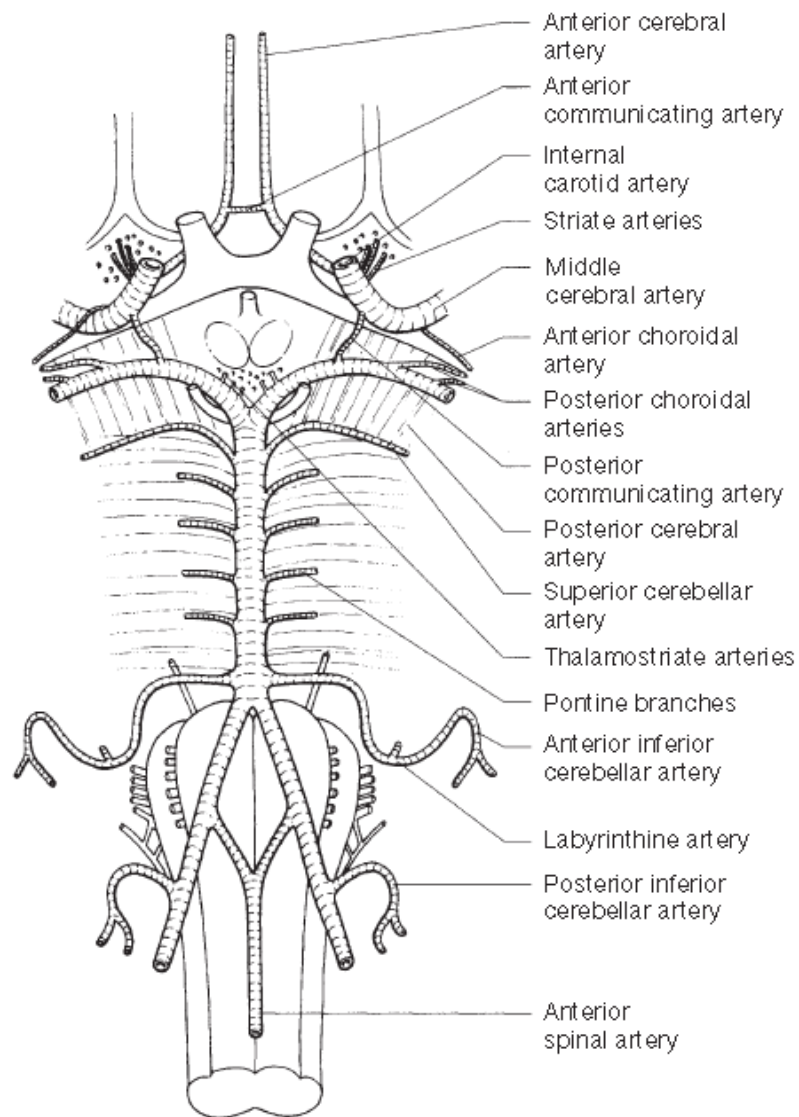


Fig (2-4): the arterial circle of Willis and arteries of the brainstem
(Stephanie et al, 2011).

2.1.3.2 Venous Drainage:

The venous system of the brain and its coverings is composed primarily of the dural sinuses, superficial cortical veins, and deep veins of the cerebrum. Dural Sinuses: The dural sinuses are very large veins located within the dura mater of the brain. All the veins of the head drain into the dural sinuses and ultimately into the internal jugular veins of the neck. The major dural sinuses include superior and inferior sagittal, straight, transverse, sigmoid, cavernous, and petrosal. The superior sagittal sinus lies in the medial plane between the falxcerebri and the calvaria. It

begins at the crista galli, runs the entire length of the falx cerebri, and ends at the internal occipital protuberance of the occipital bone. The inferior sagittal sinus, which is much smaller than the superior sagittal sinus, runs posteriorly just under the free edge of the falx cerebri the inferior sagittal sinus converges with the great cerebral vein (vein of Galen) to form the straight sinus. The straight sinus extends along the length of the junction of the falx cerebri and the tentorium cerebelli. The junction of the superior sagittal, transverse, and straight sinuses creates the large confluence of the sinuses. The transverse sinuses extend from the confluence between the attachment of the tentorium and the calvaria. As the transverse sinuses pass through the tentorium cerebelli, they become the sigmoid sinuses. The S-shaped sigmoid sinuses continue in the posterior cranial fossa to join the jugular bulbs of the internal jugular veins (Kelley, 2007).

The cavernous sinuses, located on each side of the sella and body of the sphenoid bone. Each cavernous sinus receives blood from the superior and inferior ophthalmic veins and communicates with the transverse sinuses by way of the petrosal sinuses (Kelley, 2007).

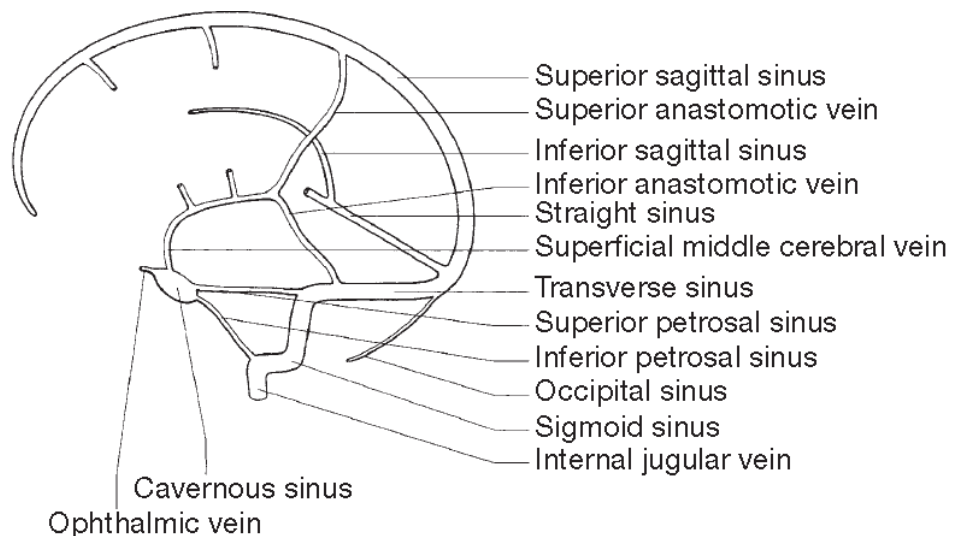


Fig (2-5): superficial cerebral veins and venous sinuses (Stephanie et al, 2011).

2.2 Physiology of the nervous system

The basic unit of the nervous system is the neuron, or nerve cell. A neuron consists of a cell body and two types of long, threadlike extensions. A single axon leads from the nerve cell body, and one or more dendrites lead toward it. Axons are insulated by a fatty covering called the myelin sheath, which increases the rate of transmission of nervous impulses (Eisenberg and Johnson, 2016).

In involuntary reactions, the impulse conduction route to and from the CNS is termed a reflex arc. Voluntary actions are commonly a reaction due to stimulation of a combination of sensors. The basic reflex arc consists of an afferent, or sensory, neuron, which conducts impulses to the CNS from the periphery; and an efferent, or motor, neuron, which conducts impulses from the CNS to peripheral effectors (muscles or glandular tissue) (Eisenberg and Johnson, 2016).

Impulses pass from one neuron to another at a junction called the synapse. Transmission at the synapse is a chemical reaction in which the termini of the axon release a neurotransmitter substance that produces an electrical impulse in the dendrites of the next axon. Once the neurotransmitter has accomplished its task, its activity rapidly terminates so that subsequent impulses pass along this same route (Eisenberg and Johnson, 2016).

The largest part of the brain is the cerebrum, which consists of two cerebral hemispheres. The outer portion of the cerebrum, termed the cortex, consists of a thin layer of gray matter where the nerve cell bodies are concentrated (Eisenberg and Johnson, 2016).

The inner area consists of white matter, which is composed of the nerve fiber tracts (Eisenberg and Johnson, 2016).

The cerebral cortex is responsible for receiving sensory information from all parts of the body and for triggering impulses that govern all motor

activity. Just posterior to the central sulcus, the cerebral cortex has specialized areas to receive and precisely localize sensory information from the PNS. Visual impulses are transmitted to the posterior portion of the brain; olfactory (smell) and auditory impulses are received in the lateral portions. The primary motor cortex is just anterior to the central sulcus. Because efferent motor fibers cross over from one side of the body to the other at the level of the medulla and spinal cord, stimulation on one side of the cerebral cortex causes contraction of muscles on the opposite side of the body. The premotor cortex, which lies anterior to the primary motor cortex, controls movements of muscles by stimulating groups of muscles that work together (Eisenberg and Johnson, 2016).

This region also contains the portion of the brain responsible for speech, which is usually on the left side in right-handed people. In addition, the cerebral cortex is the site of all higher functions, including memory and creative thought (Eisenberg and Johnson, 2016).

The two cerebral hemispheres are connected by a mass of white matter called the corpus callosum. These extensive bundles of nerve fibers lie in the midline just above the roofs of the lateral ventricles (Eisenberg and Johnson, 2016).

Deep within the white matter are a few islands of gray matter that are collectively called the basal ganglia. These structures help control position and automatic movements and consist of the caudate nuclei, the globus pallidus, and the putamen (Eisenberg and Johnson, 2016).

2.3 Pathology that characterized on this thesis:

The differential diagnosis of WM lesions is wide and depends on location, appearance and changes over time. There are many potential causes including ischaemic, inflammatory, demyelinating, metabolic, toxic and malignant. Neuroimaging protocols can be targeted to assess

the white matter and assist in narrowing the differential diagnosis. White matter changes are best seen on both T2-weighted and FLAIR sequences. The latter are particularly helpful when assessing WMH that lie close to the ventricular margin or the cortex, as nulling of signal from cerebrospinal fluid increases lesion conspicuity (Forbes, 2017).

Interpretation of magnetic resonance imaging of the brain relies on knowledge of MRI techniques as well as both the anatomy and pathophysiology of the brain and appearances on different MR sequences. There are a number of normal white matter appearances that can be confused for white matter hyperintensities (Forbes, 2017).

White matter appearances change with age and it is important to distinguish normal appearances from pathologic findings, to avoid patient anxiety and unnecessary investigations (Forbes, 2017).

2.3.1 Glioma:

The most common primary malignant brain; consist of glial cells (supporting connective tissues in the CNS) that still have the ability to multiply. They spread by direct extension and can cross from one cerebral hemisphere to the other through connecting white matter tracts, such as the corpus callosum. Gliomas have a peak incidence in middle adult life and are infrequent in persons younger than 30 years of age (Eisenberg and Johnson, 2016).

Glioblastomas are highly malignant lesions that are predominantly cerebral, although similar tumors may occur in the brainstem, cerebellum, or spinal cord. **Astrocytomas** (70% of all gliomas) are slow-growing tumors that have an infiltrative character and can form large cavities or pseudocysts (Eisenberg and Johnson, 2016).

Favored sites are the cerebrum, cerebellum, thalamus, optic chiasm, and pons (Eisenberg and Johnson, 2016).

Less frequent types of gliomas are ependymoma, medulloblastoma, and oligodendrocytoma. **Ependymomas** most commonly arise from the walls of the fourth ventricle, especially in children, and usually from the lateral ventricles in adults. **Medulloblastomas** are rapidly growing tumors, disseminating throughout the spinal fluid, which develop in the posterior portion of the vermis in children and rarely in the cerebellar hemisphere in adults. The tumor tends to spread through the subarachnoid space, with metastatic deposits occurring anywhere within the brain or spinal column. **Oligodendrocytomas** are slow-growing lesions that usually arise in the cerebrum and have a tendency to calcify (Eisenberg and Johnson, 2016).

On MR images, gliomas typically appear as masses of high signal intensity on T2-weighted images. They may be of low intensity or isointense on T1-weighted sequences. MR spectroscopy has a typical spectral pattern with a strongly increased choline peak, which indicates myelin or the breakdown of myelin (the chemical structure that goes into making white matter). In MR spectroscopy, a highly elevated choline level, a drastically lower level of N- acetylaspartate (a neuronal marker), and a drastically lower creatine/phosphocreatine ratio confirm an infiltrating glioma. Ependymomas, often partially calcified and cystic, have a heterogeneous signal intensity and show enhancement (Eisenberg and Johnson, 2016).

Edema is often seen in the adjacent subcortical white matter. After the intravenous injection of contrast material, virtually all gliomas show enhancement, with the most malignant lesions tending to be enhanced to the greatest degree. In MR spectroscopy, an elevated choline/creatine ratio suggests a malignant neoplasm. The most common pattern is an irregular ring of contrast enhancement, representing solid vascularized tumor, surrounding a central low-density area of necrosis. Contrast

enhancement also can appear as patches of increased density distributed irregularly throughout a low-density lesion or as rounded nodules of increased density within the mass (Eisenberg and Johnson, 2016).

Therapy depends on the location and histology of the tumor. Astrocytomas have a good 5-year survival rate after surgery and radiation therapy. For ependymomas of the filum terminale, surgical removal provides a favorable prognosis (Eisenberg and Johnson, 2016).

2.3.2 Multiple Sclerosis:

Multiple sclerosis is the most common demyelinating disorder; it manifests as recurrent attacks of focal neurologic deficits that primarily involve the spinal cord, optic nerves, and central white matter of the brain. The disease has a peak incidence between 20 and 40 years of age, a strong preponderance in women, and a clinical course characterized by multiple relapses and remissions. Impairment of nerve conduction caused by the degeneration of myelin sheaths leads to such symptoms as double vision, nystagmus (involuntary, rapid movement of the eyeball in all directions), loss of balance and poor coordination, shaking tremor and muscular weakness, difficulty in speaking clearly, and bladder dysfunction (Eisenberg and Johnson, 2016).

MRI is the modality of choice for demonstrating the scattered plaques of demyelination that are characteristic of multiple sclerosis. The plaques appear as multiple areas of increased signal intensity on T2-weighted images; these areas involve primarily the periventricular white matter, cerebellum, brainstem, and spinal cord. Lesions involving the optic nerve or chiasm require contrast enhancement and fat-suppression imaging (which increases the contrast difference between fat and water) to improve their detectability (Eisenberg and Johnson, 2016).

On T1-weighted images, the plaques appear as isointense or hypointense lesions that may have a beveled edge. The use of MRI sequences using

fluid-attenuated inversion recovery and fast-spin echo as well as MR spectroscopy aid in determining the extent of the disease. CT shows old inactive disease as well-defined areas of decreased attenuation in the deep white matter and periventricular regions. In the acute phase, CT performed after intravenous administration of contrast material demonstrates a mixture of nonenhancing focal areas of decreased density (representing old areas of demyelination) and enhancing regions that represent active foci (Eisenberg and Johnson, 2016).

As the disease progresses and the symptoms increase in severity, immunosuppressive agents may help limit the autoimmune attack. Antiviral drugs may slow the progress of the disease. To reduce the number and severity of attacks, some patients receive subcutaneous injections of disease-modifying immunomodulatory agents (interferon- β). The treatments can only aid in slowing the progress of multiple sclerosis; however, there is no cure (Eisenberg and Johnson, 2016).

2.3.3 Small vessel disease:

Cerebral small vessel disease (SVD) is a generic term that refers to intracranial vascular disease based on various pathological and neurological processes, as well as a syndrome referring to different clinical manifestations and neuroimaging features caused by the structural changes of vascular and brain parenchyma. It's composed of several diseases affecting the small arteries, arterioles, venules, and capillaries of the brain, and refers to several pathological processes and etiologies (Li et al, 2018).

SVD is thought to result in reduced cerebral blood flow, impaired cerebral auto-regulation and increased blood–brain barrier (BBB) permeability. However, the molecular mechanisms underlying SVD are incompletely understood. In addition, SVD is a leading cause of

functional loss, disability and cognitive decline in the elderly (Li et al, 2018).

Premature cerebrovascular disease presents as either confluent or highly discrete white matter abnormalities. Neuroimaging of SVD primarily involves visualizing a white matter hyperintensity without apparent cavitation on T2-weighted and FLAIR MRI sequences and brain atrophy (Li et al, 2018).

The ischemic white matter lesions are located more peripherally and only very rarely do they involve the corpus callosum, dorsal brainstem or cerebellar peduncles. Discrete abnormalities within the ventral pons, basal ganglia and thalami that have low T1W and high T2W signal on MRI are consistent with small vessel infarcts (Chapman, 2003).

2.4 MRI physics:

Magnetic resonance imaging it is the function of proton spin density and relaxation time (Evert, 2004).

2.4.1 Physical principal

MRI image depend on the presence of protons which is electrically charged and it rotates around its axis (spinning), this rotation generate a magnetic field around each proton (In our body these tiny bar magnets (protons) are ordered in such a way that the magnetic forces equalize) (Evert, 2004).

The proton in the hydrogen (has 1 proton and 1 electron) were used to generate MRI image because first off all we have a lot of them in the human body and secondly the gyro magnetic ratio for Hydrogen is the largest; 42.57 MHz/Tesla (Evert, 2004).

When put the hydrogen protons under the magnet they align with the magnetic field. This is happened in two ways, parallel and anti-parallel

and process or “wobble” due to the magnetic momentum of the atom (Evert, 2004).

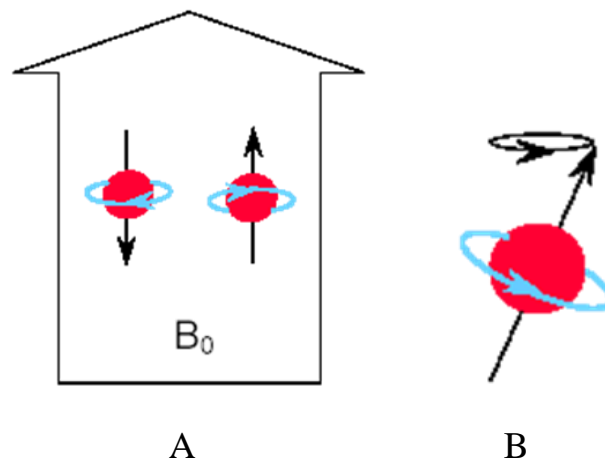


Fig (2-6): protons under the magnet they align with the magnetic field (A) and precess or “wobble”(B) (B_0 is the indication for the magnetic field of the MRI scanner) (Evert, 2004).

These protons precess at the Larmor frequency which can be calculated from the following equation:

$$\omega_0 = \gamma B_0$$

Where: ω_0 = Precessional or Larmor frequency. (MHz)
 γ = Gyro Magnetic Ratio. (MHz/T)
 B_0 = Magnetic field strength. (T)

The Larmor frequency is needed to calculate the operating frequency of the MRI system (Evert, 2004).

When protons align with the magnetic field more protons aligned parallel or low energy state than there are anti-parallel or high energy state and the number of excess protons is proportional with B_0 (Evert, 2004).

At the end there is a net magnetization (the sum of all tiny magnetic fields of each proton) pointing in the same direction as the system’s magnetic field (Evert, 2004).

2.4.2 The principal of T1, T2 and FLAIR imaging sequences can be summarized into:

2.4.2.1 T1 imaging sequence:

2.4.2.1.1 T1 recovery:

T1 recovery is caused by hydrogen nuclei giving up their energy to the surrounding environment or molecular lattice. The term *recovery* refers to the recovery of longitudinal magnetization, and *T1* relates to the fact that it is the primary relaxation process. (It is not the first process that occurs). T1 recovery takes 5–10 times longer than T2 decay. This type of relaxation is called **spin–lattice energy transfer**. Energy released by spins to the surrounding molecular lattice causes magnetic moments of hydrogen nuclei to recover their longitudinal magnetization. According to quantum theory, the number of high-energy spins decreases, and the number of low-energy spins increases as energy is lost by high-energy spins during the relaxation process. The NMV gradually realigns itself in the longitudinal plane as the proportion of spin-up and spin-down hydrogen nuclei changes (Westbrook and Talbot, 2019).

The rate of T1 recovery is an exponential process and occurs at different rates in different tissues. Longitudinal magnetization is related exponentially to recovery time. This means that most longitudinal recovery happens at the beginning of the time frame. As time progresses, gradually less and less longitudinal recovery occur until the longitudinal magnetization is fully recovered. There is a time constant associated with this exponential relationship. This is called the **T1 recovery time** and is the time it takes for 63% of the longitudinal magnetization to recover in a tissue. The T1 recovery time of a tissue is an intrinsic contrast parameter that is inherent to the tissue. The time during which T1 recovery occurs is the time between one RF excitation pulse and the

next. This is the repetition time (TR). The TR therefore determines how much T1 recovery occurs in a tissue (Westbrook and Talbot, 2019).

2.4.2.1.2 T1 contrast:

The term **T1 contrast** means that image contrast is derived from differences in the T1 recovery times of the tissues rather than any other mechanism. T1 contrast is likely to occur if vectors do not fully recover their longitudinal magnetization between each RF excitation pulse. It therefore increases if the TR is short. If the TR is longer than the relaxation times of the tissues, full recovery occurs in all tissues, and, therefore, it is not possible to produce an image that demonstrates contrast based on the differences in their T1 recovery times (Westbrook and Talbot, 2019).

2.4.2.1.3 T1 weighting

A **T1-weighted image** is one where contrast depends predominantly on the differences in the T1 recovery times between fat and water (and all the tissues with intermediate T1 recovery times) (Westbrook and Talbot, 2019).

The TR controls how far each vector recovers before the slice is excited by the next RF excitation pulse. To achieve T1 weighting, the TR must be short enough so that neither the vector in fat nor the vector in water has sufficient time to fully return to B_0 . If the TR is too long, both the vectors in fat and water return to B_0 and fully recover their longitudinal magnetization. When this occurs, T1 recovery is complete in both tissues, and the differences in their T1 recovery times are not demonstrated. T1-weighted images are used to show anatomy and pathology after administration of a contrast agent. TR controls the amount of T1 contrast. For T1 weighting, the TR must be short and the TE must also be short (Westbrook and Talbot, 2019).

2.4.2.2 T2 imaging sequence:

2.4.2.2.1 T2 decay:

T2 decay is caused by the magnetic fields of neighboring hydrogen nuclei interacting with each other. The term *decay* refers to the loss of coherent transverse magnetization, and T2 relates to the fact that it is the secondary relaxation process. This type of relaxation is termed **spin–spin relaxation** and causes dephasing of magnetic moments of the spins. Spin–spin relaxation is caused by one spin transferring energy to another spin rather than into the lattice. It occurs because hydrogen nuclei are in the same environment and experiencing the same B_0 field. Magnetic moments of all the hydrogen nuclei (spin-up and spin-down) lose phase coherence in this way (Westbrook and Talbot, 2019).

The spin whose magnetic moment is aligned in the same direction as B_0 creates a slightly larger magnetic field than is experienced by the neighboring spin. As a result, the precessional frequency of the magnetic moment of this spin increases. Conversely, the spin whose magnetic moment is aligned in the opposite direction to B_0 causes a slightly lower magnetic field than is experienced by the other spin; and its precessional frequency decreases. These small changes in frequency are sufficient to cause dephasing of magnetic moments of the spins (Westbrook and Talbot, 2019).

Spin–spin interaction is inherent to the tissue, but dephasing is also caused by inhomogeneities in the B_0 field. Inhomogeneities are areas within the magnetic field that do not exactly match the external magnetic field strength. Some areas have a magnetic field strength slightly less or slightly higher than the main magnetic field (Westbrook and Talbot, 2019).

If a hydrogen nucleus lies in an area of inhomogeneity with higher field strength, the precessional frequency of its magnetic moment increases,

i.e. it speeds up. However, if a hydrogen nucleus lies in an area of inhomogeneity with lower field strength, the precessional frequency of its magnetic moment decreases, i.e. it slows down. This relative acceleration and deceleration of magnetic moments due to magnetic field inhomogeneities, and differences in the precessional frequency in certain tissues, causes immediate dephasing of the magnetic moments of the spins. The rate of T2 decay is an exponential process and occurs at different rates in different tissues. There is more coherent transverse magnetization at the beginning of the time-frame and, as time progresses, there is less coherent transverse magnetization until all the magnetic moments dephase. There is a time constant associated with this exponential relationship. It is called the **T2 decay time** and is the time it takes for 63% of the transverse magnetization to dephase (37% is left in phase) in a tissue. The T2 decay time of a tissue is an intrinsic contrast parameter that is inherent to the tissue. The time during which this occurs is the time between an RF excitation pulse and when signal is collected in the receiver coil. The echo time (TE) therefore determines how much T2 decay occurs in a tissue when signal is collected (Westbrook and Talbot, 2019).

2.4.2.2.2 T2 contrast:

The term **T2 contrast** means that image contrast is derived from differences in the T2 decay times of the tissues rather than any other mechanism. T2 contrast is likely to occur if vectors dephase and there is a difference in coherent transverse magnetization in each tissue. It therefore increases if the TE is long. Magnetic moments of the hydrogen nuclei dephase at different rates, so if the TE is long, it is possible to produce an image that demonstrates differences in their T2 decay times. If the TE is short, then little dephasing occurs, and therefore it is not

possible to produce images that demonstrate differences in T2 decay times of the tissues (Westbrook and Talbot, 2019).

2.4.2.2.3 T2 weighting:

A **T2-weighted image** is one where contrast predominantly depends on the differences in the T2 decay times between fat and water (and all the tissues with intermediate T2 decay times). The TE controls the amount of T2 decay that occurs before signal is received. To achieve T2 weighting, the TE must be long enough to give the vectors in both fat and water time to dephase. If the TE is too short, neither the vector in fat nor the vector in water has had time to dephase, and, therefore, the differences in their T2 decay times are not demonstrated. T2-weighted images are used to image pathology because most pathology has high water content and is therefore relatively hyperintense on T2-weighted images. TE controls the amount of T2 contrast. For T2 weighting, the TE must be long and the TR must also be long (Westbrook and Talbot, 2019).

Although T2-weighted images often have a lower SNR than T1-weighted images (due to the longer TE), the ability to distinguish pathology from normal tissue is often much greater because of the high signal of pathology compared with low signal of surrounding anatomy, i.e. the CNR is higher (Westbrook and Talbot, 2019).

Contrast agent; the purpose of administering contrast agents is to increase CNR between pathology (which enhances) and normal anatomy (which does not) (Westbrook and Talbot, 2019).

2.4.2.3 Mechanism of production fluid attenuated inversion recovery (FLAIR) sequence:

FLAIR is another variation of the inversion recovery sequence. In FLAIR, an inversion time corresponding to the recovery of the vector in cerebrospinal fluid from full inversion to the transverse plane is selected.

This inversion time nulls signal from cerebrospinal fluid because there is no longitudinal magnetization present in cerebrospinal fluid. As there is no longitudinal component of cerebrospinal fluid when the 90° RF excitation pulse is applied, there is no transverse component after excitation, and signal from cerebrospinal fluid is nulled. FLAIR is used to suppress high cerebrospinal fluid signal in T2 weighted images so that the pathology adjacent to cerebrospinal fluid is seen more clearly. An inversion time of 1700–2200 ms usually achieves cerebrospinal fluid suppression (although this varies slightly at different field strengths and is calculated by multiplying the T1 relaxation time of cerebrospinal fluid by 0.69) (Westbrook and Talbot, 2019).

2.5 MRI Techniques

2.5.1 Equipment:

Head coil (quadrature or multi-coil array), immobilization pads and straps, ear plugs, high-performance gradients for EPI, diffusion and perfusion imaging (Westbrook, 2008).

2.5.2 Patient positioning:

The patient lies supine on the examination couch with their head within the head coil. The head is adjusted so that the inter-pupillary line is parallel to the couch and the head is straight. The patient is positioned so that the longitudinal alignment light lies in the midline, and the horizontal alignment light passes through the nasion. Straps and foam pads are used for immobilization (Westbrook, 2008).

2.5.3 Suggested protocol

Sagittal SE/FSE/incoherent (spoiled) GRE T1

Medium slices/gap are prescribed on each side of the longitudinal alignment light from one temporal lobe to the other. The area from the

foramen magnum to the top of the head is included in the image (Westbrook, 2008).

Axial/oblique SE/FSE PD/T2

Medium slices/gap are prescribed from the foramen magnum to the superior surface of the brain. Slices may be angled so that they are parallel to the anterior–posterior commissure axis. This enables precise localization of lesions from reference to anatomy atlases (Fig (2-7)). Many sites have replaced the PD sequence with FLAIR (Westbrook, 2008).

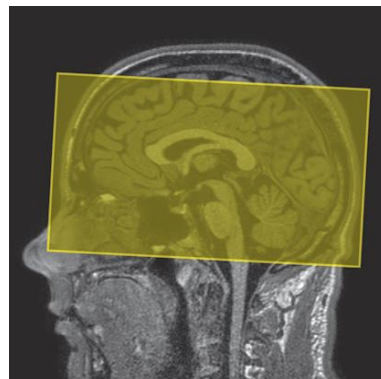


Fig (2-7): Sagittal SE T1 weighted midline slice of the brain showing slice prescription boundaries and orientation for axial/oblique imaging (Westbrook, 2008).

Coronal SE/FSE PD/T2

As for Axial PD/T2, except prescribe slices from the cerebellum to the frontal lobe (Fig (2-8)) (Westbrook, 2008).

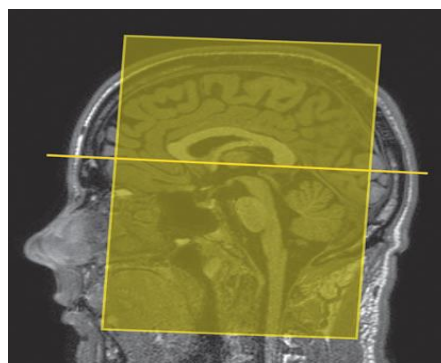


Fig (2-8): Sagittal SE T1 weighted image showing slice prescription boundaries and orientation for coronal imaging (Westbrook, 2008).

2.5.4 Additional sequences

Axial/oblique FLAIR/EPI (Fig(2-9))

Slice prescription as for Axial/oblique T2. This sequence provides a rapid acquisition with suppression of CSF signal. It may be useful when examining periventricular or cord lesions such as MS plaques (Westbrook, 2008).

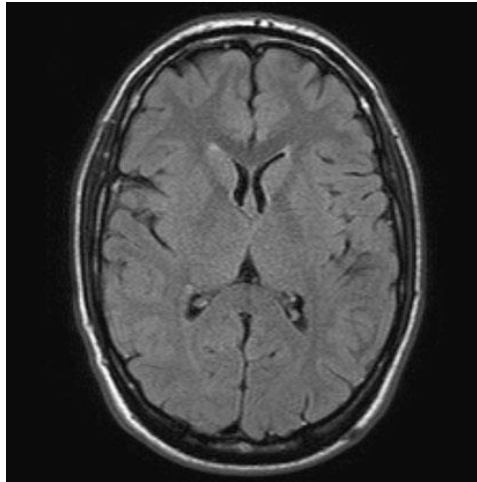


Fig (2-9): Axial/oblique FLAIR image of the brain. Periventricular abnormalities will have high signal intensity in contrast to the low signal of CSF which has been nulled using a long TI (Westbrook, 2008).

Axial/oblique/Coronal/oblique IR-FSE T2

Slice prescription as for Axial/oblique/Coronal/oblique FSE T2.

This sequence often provides images with high contrast between grey matter and white matter. A TI selected to null the signal from white matter (about 300 ms) can be used to increase the grey/white contrast in the hippocampal region. Images may be video-inverted so that white matter appears white and the grey matter appears grey. This is sometimes useful to increase the conspicuity of white matter lesions, which have low signal intensity when using this technique (Westbrook, 2008).

2.7 Texture analysis:

Texture can be defined as the relationship between the pixels; therefore it can pick up the microscopic structures and hence it is superior to visual perception which is solely subjective. Texture can be calculate using a window of appropriate size that depict the underlined textures using features vector that correlated with the classes of interest for successful classification and segmentation of the underline textures through a suitable classifier (e.g. k-means, linear discriminate analysis, neural network, etc...).Texture is an important characteristic for the analysis of many types of images. It can be seen in all images from multi spectral scanner images obtained from aircraft or satellite platforms (which the remote sensing community analyzes) to microscopic images of cell cultures or tissue samples (which the biomedical community analyzes).

Despite its importance and ubiquity in image data, a formal approach or precise definition of texture does not exist (Haralick, 1979).

Image texture, defined as a function of the spatial variation in pixel intensities (gray values), is useful in a variety of applications and has been a subject of intense study by many researchers. One immediate application of image texture is the recognition of image regions using texture properties. Texture is the most important visual cue in identifying these types of homogeneous regions. This is called texture classification (Haralick, 1979).

Image analysis techniques have played an important role in several medical applications. In general, the applications involve the automatic extraction of features from the image which is then used for a variety of classification tasks, such as distinguishing normal tissue from abnormal tissue. Depending upon the particular classification task, the extracted features capture morphological properties, color properties, or certain textural properties of the image (Clausi et. al., 2002).

Texture is a combination of repeated patterns with a regular frequency. In visual interpretation texture has several types, for example, smooth, fine, coarse etc., which are often used in the classification of forest types. Texture analysis can also be defined as the classification or segmentation of textural features with respect to the shape of a small element, density and direction of regularity. In the case of digital image, it is difficult to treat the texture mathematically because texture cannot be standardized quantitatively and the data volume is so huge (Clausi et. al., 2002).

2.7.1 Texture Analysis Types:

At present; statistical, structural-, transform-, and spectral-based TAs are the most common agnostic methods used (Soni et al, 2019).

2.7.2 .Feature Estimation

Numerous approaches to the quantification and characterization of image texture have been proposed, with most textural features falling under 3 general categories: syntactic, statistical, and spectral (Kassner, 2010).

2.7.2.1. Structural texture analysis:

Structural (model-based) methods such as fractal analysis provide information about the self-symmetry of the objects (Soni et al, 2019).

2.7.2.2. Statistical Features:

Statistical based TA depends on the pixel values, distribution, and spatial interrelationship in the defined ROI (Soni et al, 2019).

First-order statistical TA is a histogram representation of image intensities in a predefined ROI and calculates mean, median, percentile, SD, skewness entropy, uniformity, and kurtosis. Mean is a measure of central tendency (average brightness), SD depicts dispersion from the mean, skewness reflects asymmetry of the histogram, kurtosis depicts the pointedness of the histogram (visual contrast), and entropy reflects the irregularity of the imageintensity distribution. The more heterogeneous the tumor, the higher the entropy is (Soni et al, 2019).

Second-order or higher order statistical TA quantifies the image pattern on the basis of the spatial relationship or co-occurrence of the pixel value. It consists of several methods, including the 2 most common ones: gray-level co-occurrence matrix (GLCM) and gray-level run-length matrix (GLRLM). The GLCM measures the frequency of pixel pair distribution at a predefined distance,² usually measured in 4 directions (0° , 45° , 90° , and 135°) for 2D and in 13 directions for 3D. GLCM features include homogeneity, inverse difference moment (IDM), dissimilarity, correlation, energy, and entropy. GLRLM observes the run of a specific pixel value over a chosen direction and consists of gray level nonuniformity, run-length nonuniformity, short-run emphasis, and long-run emphasis. Both GLCM and GLRLM are calculated in different directions and averaged to make them rotationally invariant. GLCM may be measured over different pixel distances (for example, from 1 to 5), and similarly, GLRLM is computed over different run lengths to compute different texture features from the same ROI. GLCM and GLRLM over short distance and run provide fine texture, and over longer distance and run provide coarse texture (Soni et al, 2019).

The first- and second-order statistical methods are used most commonly. First-order statistical methods provide global information, and second-order statistical methods provide additional information regarding the transition among pixel values (Soni et al, 2019).

2.7.2.3. Spectral Features:

Spectral methods include wavelet, Gabor, and Fourier transforms and are based on transforming the spatial information of the image into spatial frequencies. Co-occurrence or run-length features may lack the sensitivity to identify larger scale or more coarse changes in spatial frequency. Wavelet functions, for example, can be designed to evaluate spatial frequencies at multiple scales and have found a natural

application to texture analysis. Readers will recognize the close relative of the wavelet transform, the Fourier transform, which can identify the spatial frequencies present in signal intensity but cannot delineate temporal changes in frequency content and presumes that all signals reflect a superposition of sinusoids. Sometime localization can be imparted to Fourier analysis by means of the windowed or “short-time” method, which allows for the Fourier transform to be performed on sequential portions of the entire signal intensity, each of a set length or “window.” The wavelet transform provides even more flexibility by enabling us to trade some degree of spatial-frequency resolution for the ability to localize this frequency content in time (Kassner, 2010).

2.8 Previous studies:

Jing in 2008 enrolled a comparative study the difficulty of using magnetic resonance imaging (MRI) to support early diagnosis of multiple sclerosis (MS) stems from the subtle pathological changes in the central nervous system (CNS). In this study, texture analysis was performed on MR images of MS patients and normal controls and a combined set of texture features were explored in order to better discriminate tissues between MS lesions, normal appearing white matter (NAWM) and normal white matter (NWM). Features were extracted from gradient matrix, run-length (RL) matrix, gray level co-occurrence matrix (GLCM), autoregressive (AR) model and wavelet analysis, and were selected based on greatest difference between different tissue types. The results of the combined set of texture features were compared with our previous results of GLCM-based features alone. The results of this study demonstrated that : (1) with the combined set of texture features, classification was perfect (100%) between MS lesions and NAWM (or NWM), less successful (88.89%) among the three tissue types and worst

(58.33%) between NAWM and NWM; (2) compared with GLCM-based features, the combined set of texture features were better at discriminating MS lesions and NWM, equally good at discriminating MS lesions and NAWM and at all three tissue types, but less effective in classification between NAWM and NWM. This study suggested that texture analysis with the combined set of texture features may be equally good or more advantageous than the commonly used GLCM-based features alone in discriminating MS lesions and NWM/NAWM and in supporting early diagnosis of MS.

Loizou 2014 on his study he investigates the application of texture analysis methods on brain T2-white matter lesions detected with magnetic resonance imaging (MRI) for the prognosis of future disability in subjects diagnosed with clinical isolated syndrome (CIS) of multiple sclerosis (MS). Methods: Brain lesions and normal appearing white matter (NAWM) from 38 symptom at untreated subjects diagnosed with CIS as well as normal white matter (NWM) from 20 healthy volunteers, were manually segmented, by an experienced MS neurologist, on transverse T2-weighted images obtained from serial brain MR imaging scans (0 and 6—12 months). Addition all clinical information in the form of the Expanded Disability Status Scale (EDSS), a scale from 0 to 10, which provides a way of quantifying disability in MS and monitoring the changes overtime in the level of disability, were also provided. Shape and most importantly different texture features including GLCM and laws were then extracted for all above regions, after image intensity normalization. Results: The findings showed that: (i) there were significant differences for the texture futures extracted between the NAWM and lesions at 0 month and between NAWM and lesions at 6—12 months. However, no significant differences were found for all texture features extracted when comparing lesions temporally at 0 and

6—12 months with the exception of contrast (gray level difference statistics-GLDS) and difference entropy (spatial gray level dependence matrix-SGLDM); (ii) significant differences were found between NWM and NAWM for most of the texture features investigated in this study; (iii) there were significant differences found for the lesion.

Sarah in 2016 the aim of their study was to characterize of MS plaques in MR images using texture analysis features which enabling disease characterization and quantification of disease, it consisted from 50 MR brain images for patient having multiple sclerosis. The results reveal that the MS areas were very different from the rest of the tissues on FLAIR images with classification accuracy of 91.2% and on T2 images with classification accuracy of 89.5 %. And classification between the MS plaques and SVD are very different with classification accuracy of 100% between both of them (no interference) on FLAIR images. And in T2 and FLAIR images the MS plaques have a mean higher than the grey matter and the white matter, also the entropy textural feature on MS and normal brain tissues on FLAIR and T2 images has successfully differentiate between them on both sequences. While energy had discriminate between the MS plaques and brain tissue on FLAIR images but on T2 images there is a interference between the MS and white matter.

Qurat in 2010 Studied classification and segmentation of brain tumor using texture analysis. Methods: consists of multiple phases. First phase consists of texture feature extraction from brain MR images. Second phase classify brain images on the bases of these texture feature using ensemble base classifier. After classification tumor region is extracted from those images which are classified as malignant using two stage segmentation process. Segmentation consists of skull removal and tumor extraction phases. Quantitative results show that our proposed system

performed very efficiently and accurately. We achieved accuracy of classification beyond 99%. Segmentation results also show that brain tumor region is extracted quite accurately.

Maria in 2017 studied the application of texture analysis to study small Vessel Disease and Blood–Brain Barrier integrity. The aim of his study was to evaluate the alternative use of texture analysis for evaluating the role of blood–brain barrier (BBB) in small vessel disease (SVD).

Methods: he used brain magnetic resonance imaging from 204 stroke patients, acquired before and 20 min after intravenous gadolinium administration. We segmented tissues, white matter hyperintensities (WMH) and applied validated visual scores. He measured textural features in all tissues pre- and post-contrast and used ANCOVA to evaluate the effect of SVD indicators on the pre-/post-contrast change, Kruskal–Wallis for significance between patient groups and linear mixed models for pre-/post-contrast variations in cerebrospinal fluid (CSF) with Fazekas scores. **Results:** Textural “homogeneity” increase in normal tissues with higher presence of SVD indicators was consistently more overt than in abnormal tissues. Textural “homogeneity” increased with age, basal ganglia perivascular spaces scores ($p < 0.01$) and SVD scores ($p < 0.05$) and was significantly higher in hypertensive patients ($p < 0.002$) and lacunar stroke ($p = 0.04$). Hypertension (74% patients), WMH load (median = $1.5 \pm 1.6\%$ of intracranial volume), and age (mean = 65.6 years, SD = 11.3) predicted the pre/ post-contrast change in normal white matter, WMH, and index stroke lesion. CSF signal increased with increasing SVD post-contrast. Conclusion: A consistent general pattern of increasing textural “homogeneity” with increasing SVD and post-contrast change in CSF with increasing WMH suggests that texture analysis may be useful for the study of BBB integrity.

Doaa in 2003 studied the three dimensional texture analyses in MRI: a preliminary evaluation in gliomas the discrimination of tumor boundaries from normal tissue, as well as the evaluation of tissue heterogeneity and tumor grading often continue to pose a challenge in MRI. Although yielding promising results in various fields of medical imaging, two- dimensional (2D) texture analysis in MRI has, until now, demonstrated a lack of specificity in brain tumor classification. A new three-dimensional (3D) approach using Cooccurrence Matrix analysis is proposed to increase the sensitivity and specificity of brain tumor characterization. A preliminary comparative evaluation of 2D and 3D texture analysis was performed on T1-weighted MRI of seven gliomas for characterization of solid tumor, necrosis, edema and surrounding white matter. With 3D compared to 2D method, a better discrimination is obtained between necrosis and solid tumor as well as between edema and solid tumor. Using both methods, peritumoral white matter overlaps with edema, but is completely separated from far homo-lateral matter. This latter shows a complete overlapping with contra-lateral matter. The 3D texture analysis approach could provide a new tool for tumor grading and treatment follow-up, as well as for surgery or radiation therapy planning.

Tian et al in 2018 in there study regarding radiomics strategy for Glioma grading using texture features from multiparametric MRI, Patients' ages between LGG and HGG groups were significantly different ($P < 0.01$). For each patient, 420 texture and 90 histogram parameters were derived from 10 VOIs of multiparametric MRI. SVM models were established using 30 and 28 optimal features for classifying LGGs from HGGs and grades III from IV, respectively. The accuracies/AUCs were 96.8%/0.987 for classifying LGGs from HGGs,

and 98.1%/0.992 for classifying grades III from IV, which were more promising than using histogram parameters or using the single sequence MRI. In conclusion texture features were more effective for noninvasively grading gliomas than histogram parameters. The combined application of multiparametric MRI provided a higher grading efficiency. Also found that the T1+C were the best single sequence for glioma grading in MR texture analysis.

Ditmer et al in 2018 there studied the diagnostic accuracy of MRI texture analysis for grading gliomas, there Results reveals that of a total of 94 patients, 14 had low-grade gliomas and 80 had high-grade gliomas. Mean, SD, MPP, entropy and kurtosis each showed significant differences between glioma grades for different spatial scaling filters. Low and high-grade gliomas were best-discriminated using mean of 2 mm fine texture scale, with a sensitivity and specificity of 93% and 86% (AUC of 0.90). also and found that using the statistical parameter standard deviation at fine texture scale is the best to discriminate the gliomas grads with high a sensitivity and specificity on T1+C images. In conclusions quantitative measurement of heterogeneity using TA can discriminate high versus low-grade gliomas. Radiomic data of texture features can provide complementary diagnostic information for gliomas.

Skogen et al in 2016 in there study about diagnostic performance of texture analysis on MRI in grading cerebral gliomas, there results shows that LGG and HGG was best discriminated using SD at fine texture scale, with a sensitivity and specificity of 93% and 81% (AUC 0.910, $p < 0.0001$). The diagnostic ability for MRTA to differentiate between the different sub-groups (grade II–IV) was slightly lower but still significant.

Xie et al in 2018 in their study regarding textural features of dynamic contrast-enhanced MRI derived model-free and model-based parameter maps in glioma grading, using Field Strength/Sequence: 3.0T, including conventional anatomic sequences and DCE-MRI sequences (variable flip angle T1-weighted imaging and three-dimensional gradient echo volumetric imaging). Their results reveal that both Entropy and IDM of Extended Tofts- and Patlak-based v_p showed highest area under curve in discriminating between grade III and IV gliomas. However, intraclass correlation coefficient of these features revealed relatively lower inter-observer agreement. No significant correlation was found between microvascular density and textural features, compared with a moderate correlation found between cellular proliferation index and those features.

Chapter Three

Materials and Methods

3.1 Materials:

3.1.1 Study design:

This is analytical study of a case control type where normal T1, T2 and FLAIR MR images of the brain taken as a reference.

3.1.2 Study area and duration:

This study was achieved in Antalya medical center and it was conducted from October 2018 to March 2021.

3.1.3 Study population:

The population of this study includes MR images for patients having: SVD (ischemic), MS (demyelinating diseases) and Gliomas (tumors) .

3.1.4 Sample size and type:

The sample of this study consists of 1646 brain MR images selected conveniently from patients with Glioma (295), MS (497), SVD (542), (312) normal MR images.

3.1.4.1 Inclusion criteria:

Glioma, MS and SVD patients, age >18 years.

3.1.4.2 Exclusion criteria:

Patients having two types of lesions at the same time.

3.1.5 Equipment and software programs used in the study:

The machine that used was MRI device: 1.5 Tesla, closed system (General Electric), head coil.

RadiAnt . DICOM viewer 32-Bit Version.

Interactive Data language (IDL Version 6.1 win 32 (x86)) for Windows Integrated Development Environment (Classification features Clicks, Classification features).

IBM SPSS Statistics, 32-Bit 20.0 Windows Multilingual.

3.2 Method of data collection and analysis:

After that MR image was stored in computer disk they was viewed by the Radiant, DICOM viewer in computer, to select the section of image that have the lesion on it and then this images uploaded it into the computer based software Interactive Data language (IDL) where the DICOM image converted to TIFF format and the user then clicks on areas represents the grey matter, white matter, glioma, MS plaque and the SVD . In these areas a window of 3×3 pixel was set and the first and higher order statistics were extracted. Including the first order statistics (intensity-histogram-based features): Mean, variance, kurtosis, skewness, energy and entropy. And higher-order statistics texture features (Short Run Emphasis (SRE), Long Run Emphasis (LRE), Gray-Level Nonuniformity (GLN), Run-Length Nonuniformity (RLN), Run Percentage (RP), Low Gray-Level Run Emphasis (LGRE), High Gray-Level Run Emphasis (HGRE), Short Run Low Gray-Level Emphasis (SRLGE), Short Run High Gray-Level Emphasis (SRHGE), Long Run Low Gray-Level Emphasis (LRLGE), Long Run High Gray-Level Emphasis (LRHGE)). These features are then assigned as classification center used to classify the whole image into different classes using the Euclidean distance. The algorithm scans the whole image using a window of 3×3 pixel and a window of 6×6 pixel for computing the first and higher order statistics respectively, and computes the distance (the Euclidean distance) between the calculated features and the class's centers and assigns the window to the class with the lowest distance. Then the window interlaced one pixel and the same process stated over till the entire image were classified the data concerning grey matter, white matter, glioma, MS plaque and the SVD; to form the classification map. Also these features was entered into SPSS with its classes to generate a classification score using stepwise linear discriminate

analysis; to select the most discriminate feature that can be used in the classification of white matter pathologies. then scatter plot using discriminate function was generated as well as classification accuracy and linear discriminate function equation to differentiate between white matter pathologies for unseen images.

3.3 Ethical considerations:

Ethical approval from Sudan university of science and technology. Khartoum state ministry of health research department and from hospitals where no patient identification data or individual patient detail is published.

Research purpose and objectives was explained to participant in clear simple words.

Participant has right to voluntary informed consent.

Participant has the right to withdraw at any time without any deprivation.

Participant has the right to no harm (privacy and confidentiality by using coded questionnaire).

Participant has the right to benefit from the researcher knowledge and skills.

The data was collected from the PACS and radiology department in their rest time without any interruption to their work.

Chapter Four The Results

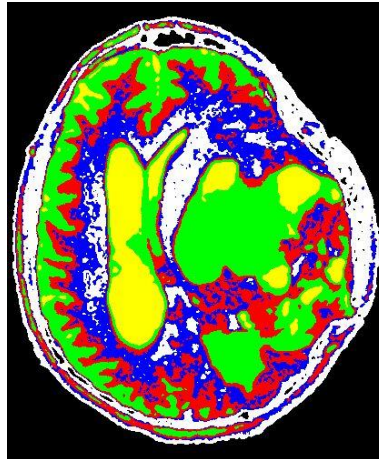


Fig (4-1): shows color map in T2 image for Glioma patient

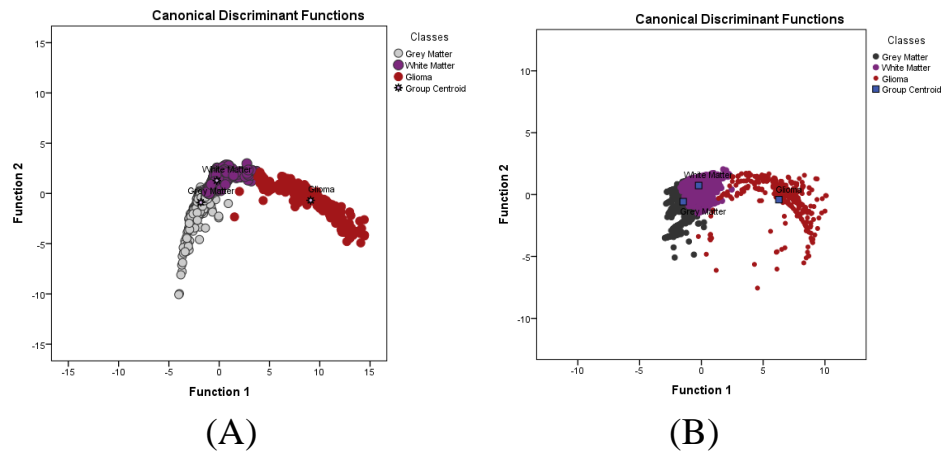


Fig (4-2): Scatter plot demonstrate the classification of brain tissues using linear discriminate analysis on T1 images for Glioma patients. First order features (A) and higher order features (B)

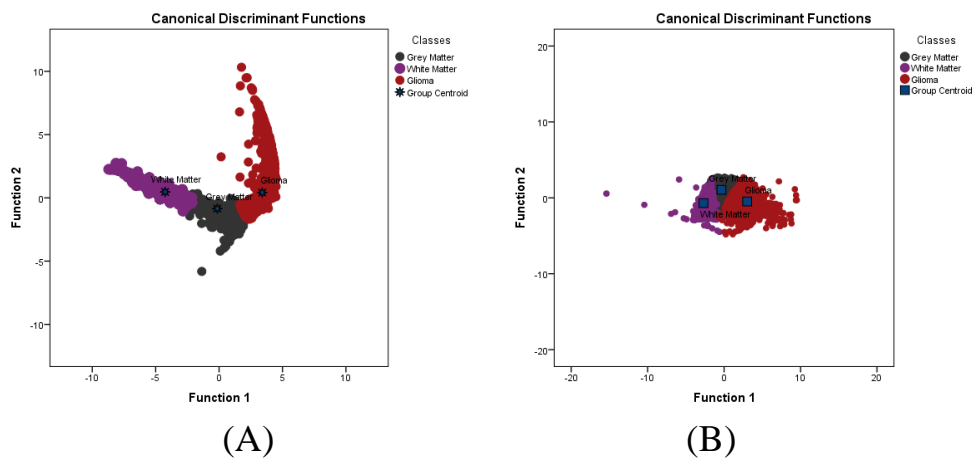


Fig (4-3): Scatter plot demonstrate the classification of brain tissues using linear discriminate analysis on T2 images for Glioma patients. First order features (A) and higher order features (B)

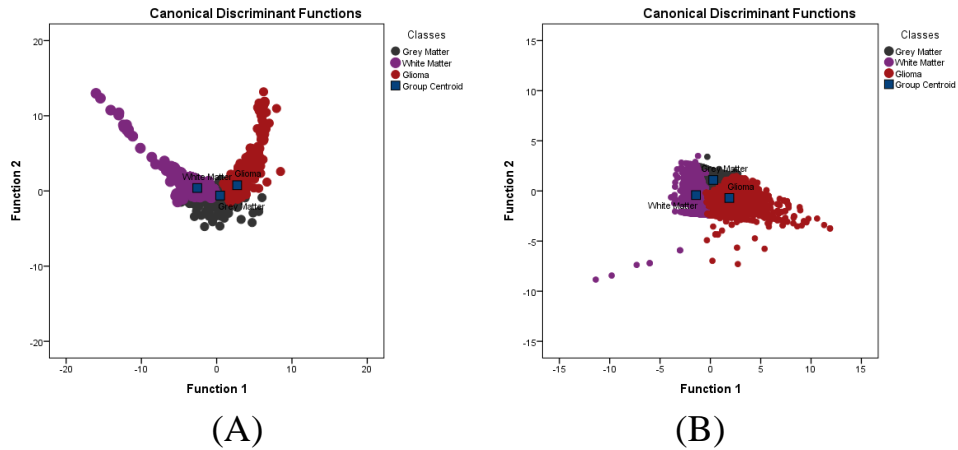


Fig (4-4): Scatter plot demonstrate the classification of brain tissues using linear discriminate analysis on FLAIR images for Glioma patients. First order features (A) and higher order features (B)

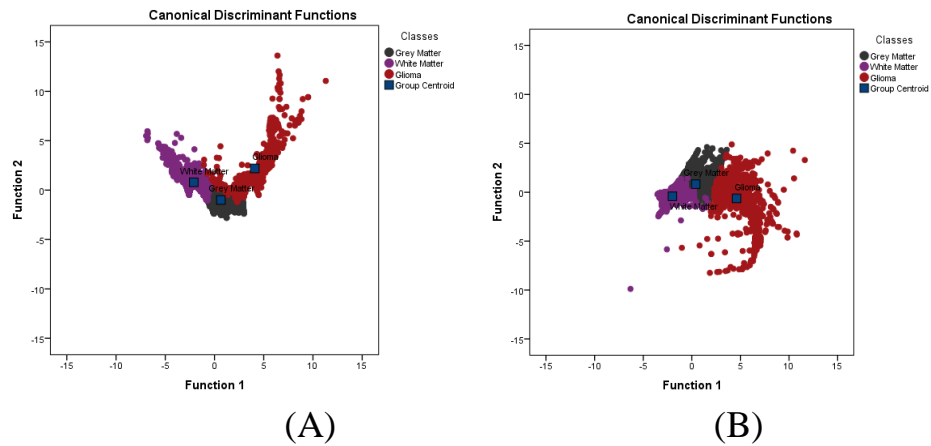


Fig (4-5): Scatter plot demonstrate the classification of brain tissues using linear discriminate analysis on T1+ C images for Glioma patients. First order features (A) and higher order features (B)

Table 4-1: Cross-tabulation shows the classification results of first order features from the classes using linear discriminate analysis on T1 images for Glioma patients.

		Classes	Predicted Group Membership			Total
			Grey Matter	White Matter	Glioma	
Original	Count	Grey Matter	1229	2	0	1231
		White Matter	65	940	0	1005
		Glioma	1	11	262	274
Original	%	Grey Matter	99.8	.2	.0	100.0
		White Matter	6.5	93.5	.0	100.0
		Glioma	.4	4.0	95.6	100.0
a. 96.9% of original grouped cases correctly classified.						

Table 4-2: Cross-tabulation shows the classification results of first order features from the classes using linear discriminate analysis on T2 images for Glioma patients.

		Classes	Predicted Group Membership			Total
			Grey Matter	White Matter	Glioma	
Original	Count	Grey Matter	3291	13	0	3304
		White Matter	24	2723	0	2747
		Glioma	63	0	3515	3578
	%	Grey Matter	99.6	.4	.0	100.0
		White Matter	.9	99.1	.0	100.0
		Glioma	1.8	.0	98.2	100.0
a. 99.0% of original grouped cases correctly classified.						

Table 4-3: Cross-tabulation shows the classification results of first order features from the classes using linear discriminate analysis on FLAIR images for Glioma patients.

		Classes	Predicted Group Membership			Total
			Grey Matter	White Matter	Glioma	
Original	Count	Grey Matter	5359	44	21	5424
		White Matter	412	3156	0	3568
		Glioma	419	0	2054	2473
	%	Grey Matter	98.8	.8	.4	100.0
		White Matter	11.5	88.5	.0	100.0
		Glioma	16.9	.0	83.1	100.0
a. 92.2% of original grouped cases correctly classified.						

Table 4-4: Cross-tabulation shows the classification results of first order features from the classes using linear discriminate analysis on T1+C images for Glioma patients.

		Classes	Predicted Group Membership			Total
			Grey Matter	White Matter	Glioma	
Original	Count	Grey Matter	4580	59	0	4639
		White Matter	249	2998	0	3247
		Glioma	138	14	786	938
	%	Grey Matter	98.7	1.3	.0	100.0
		White Matter	7.7	92.3	.0	100.0
		Glioma	14.7	1.5	83.8	100.0
a. 94.8% of original grouped cases correctly classified.						

Table 4-5: Cross-tabulation shows the classification results of higher order features from the classes using linear discriminate analysis on T1 images for Glioma patients.

		Classes	Predicted Group Membership			Total
			Grey Matter	White Matter	Glioma	
Original	Count	Grey Matter	967	187	0	1154
		White Matter	124	951	0	1075
		Glioma	9	27	273	309
	%	Grey Matter	83.8	16.2	.0	100.0
		White Matter	11.5	88.5	.0	100.0
		Glioma	2.9	8.7	88.3	100.0
a. 86.3% of original grouped cases correctly classified.						

Table 4-6: Cross-tabulation shows the classification results of higher order features from the classes using linear discriminate analysis on T2 images for Glioma patients.

		Classes	Predicted Group Membership			Total
			Grey Matter	White Matter	Glioma	
Original	Count	Grey Matter	3247	219	0	3466
		White Matter	227	2878	0	3105
		Glioma	249	27	2887	3163
	%	Grey Matter	93.7	6.3	.0	100.0
		White Matter	7.3	92.7	.0	100.0
		Glioma	7.9	.9	91.3	100.0
a. 92.6% of original grouped cases correctly classified.						

Table 4-7: Cross-tabulation shows the classification results of higher order features from the classes using linear discriminate analysis on FLAIR images for Glioma patients.

		Classes	Predicted Group Membership			Total
			Grey Matter	White Matter	Glioma	
Original	Count	Grey Matter	3700	190	58	3948
		White Matter	446	4571	4	5021
		Glioma	252	342	2606	3200
	%	Grey Matter	93.7	4.8	1.5	100.0
		White Matter	8.9	91.0	.1	100.0
		Glioma	7.9	10.7	81.4	100.0
a. 89.4% of original grouped cases correctly classified.						

Table 4-8: Cross-tabulation shows the classification results of higher order features from the classes using linear discriminate analysis on T1+C images for Glioma patients.

		Classes	Predicted Group Membership			Total
			Grey Matter	White Matter	Glioma	
Original	Count	Grey Matter	3055	251	0	3306
		White Matter	237	4026	0	4263
		Glioma	97	2	1457	1556
	%	Grey Matter	92.4	7.6	.0	100.0
		White Matter	5.6	94.4	.0	100.0
		Glioma	6.2	.1	93.6	100.0

a. 93.6% of original grouped cases correctly classified.

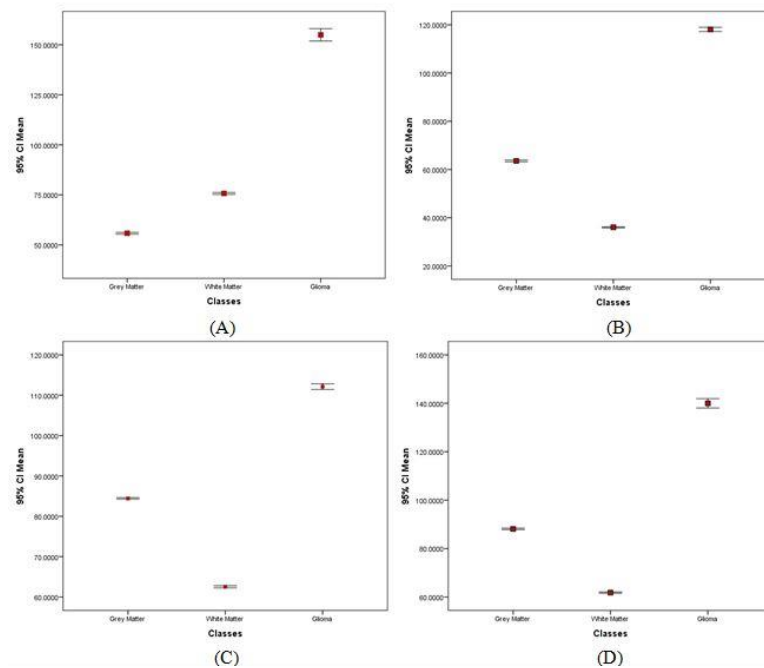


Fig (4-6): Error bar plot show the discriminate power of the Mean textural feature distribution for the selected classes on T1(A), T2(B), FLAIR(C) and T1+C(D) images for Glioma patients

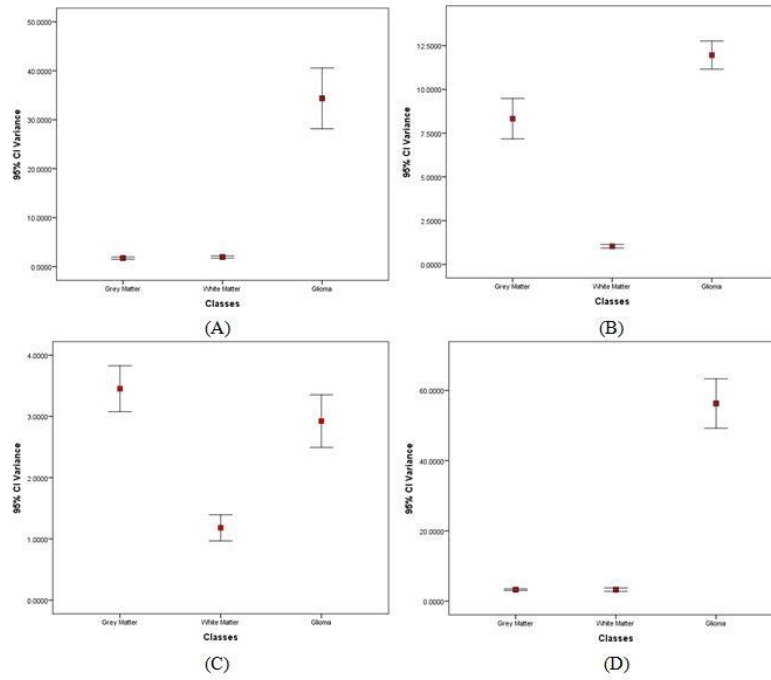


Fig (4-7): Error bar plot show the discriminate power of the Variance textural feature distribution for the selected classes on T1(A), T2(B), FLAIR(C) and T1+C(D) images for Glioma patients

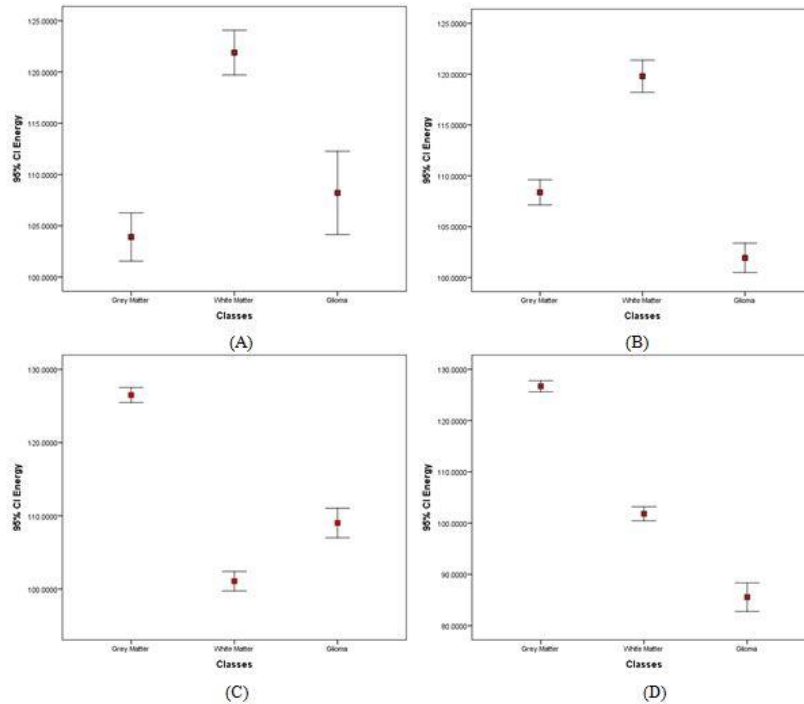


Fig (4-8): Error bar plot show the discriminate power of the Energy textural feature distribution for the selected classes on T1 (A), T2(B), FLAIR(C) and T1+C(D) images for Glioma patients

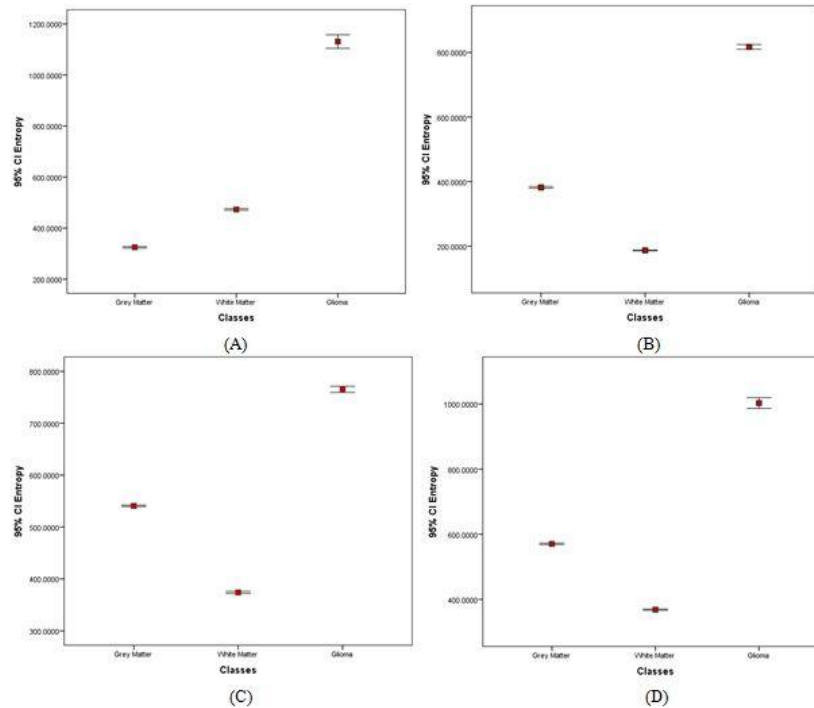


Fig (4-9): Error bar plot show the discriminate power of the Entropy textural feature distribution for the selected classes on T1(A), T2(B), FLAIR(C) and T1+C(D) images for Glioma patients

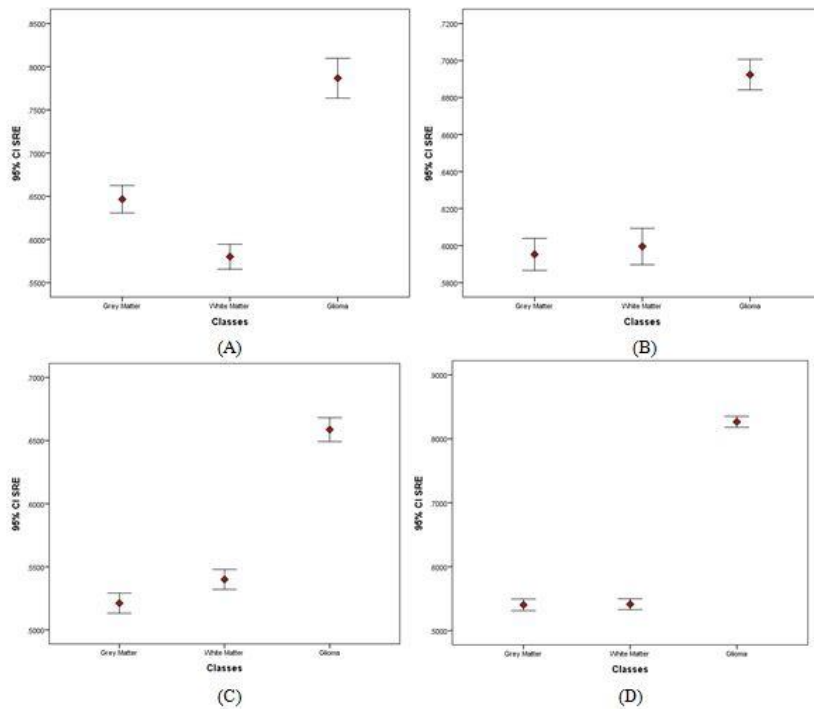


Fig (4-10): Error bar plot show the discriminate power of the SRE textural feature distribution for the selected classes on T1(A), T2(B), FLAIR(C) and T1+C(D) images for Glioma patients

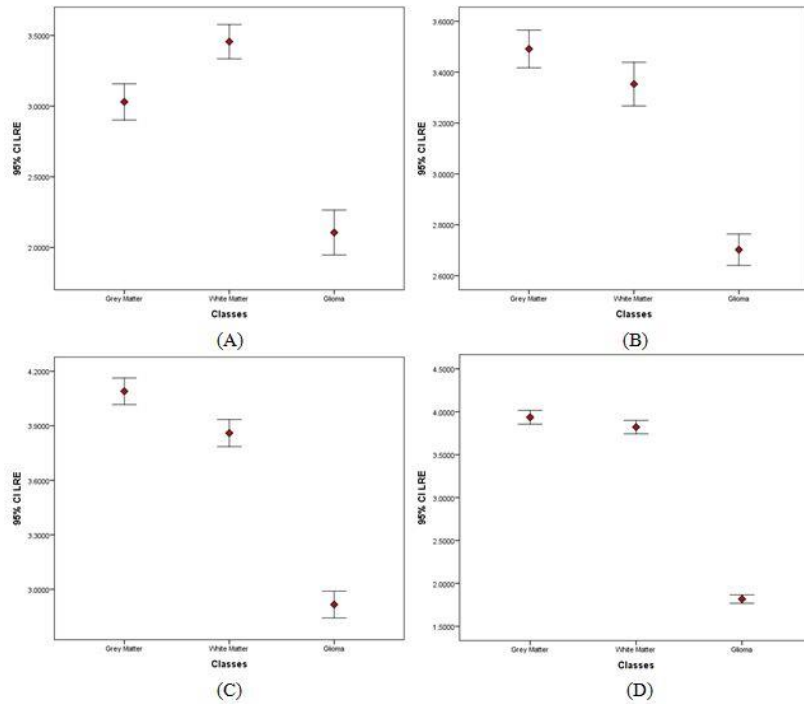


Fig (4-11): Error bar plot show the discriminate power of the LRE textural feature distribution for the selected classes on T1(A), T2(B), FLAIR(C) and T1+C(D) images for Glioma patients

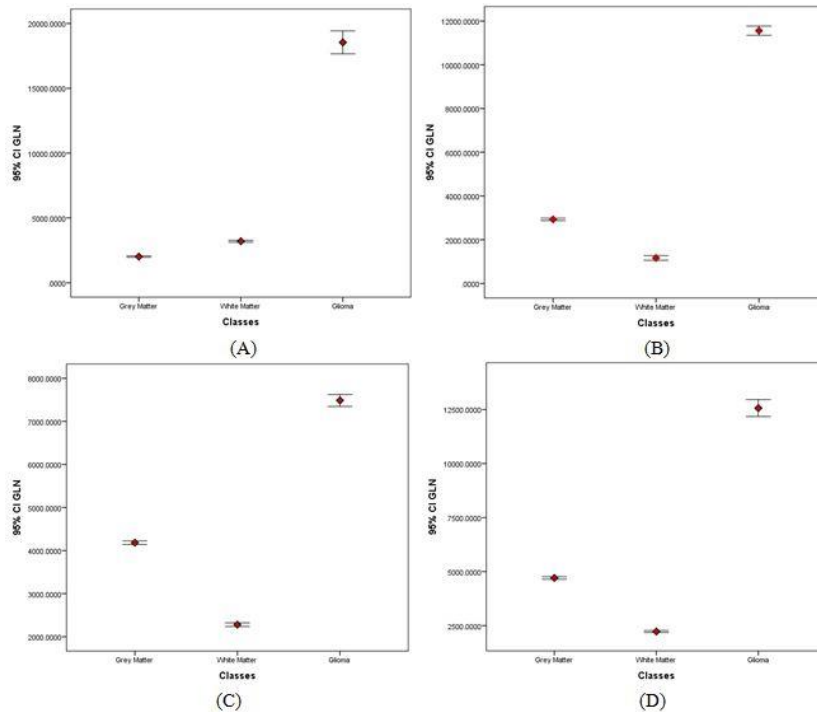


Fig (4-12): Error bar plot show the discriminate power of the GLN textural feature distribution for the selected classes on T1(A), T2(B), FLAIR(C) and T1+C(D) images for Glioma patients

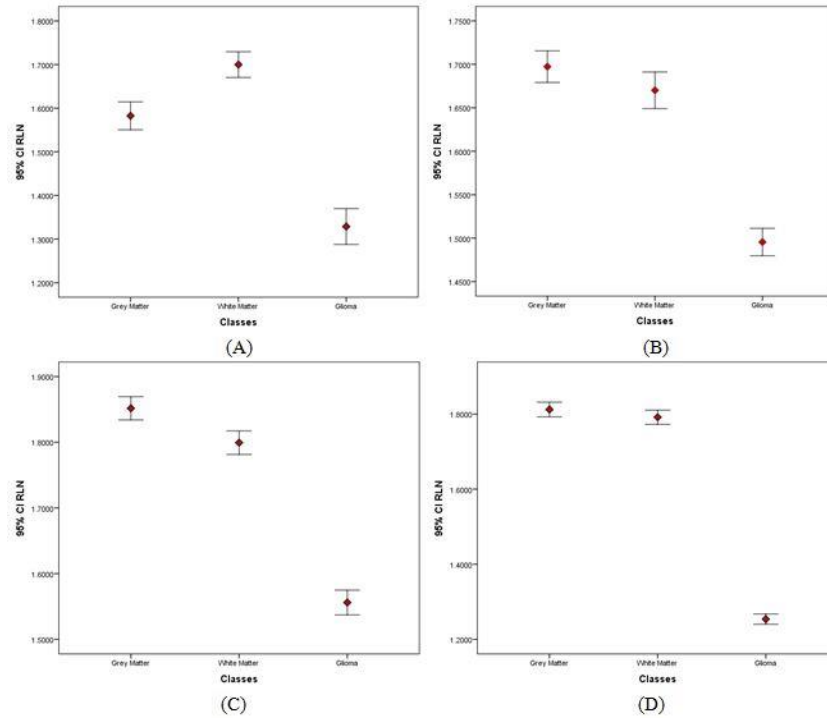


Fig (4-13): Error bar plot show the discriminate power of the RLN textural feature distribution for the selected classes on T1(A), T2(B), FLAIR(C) and T1+C(D) images for Glioma patients

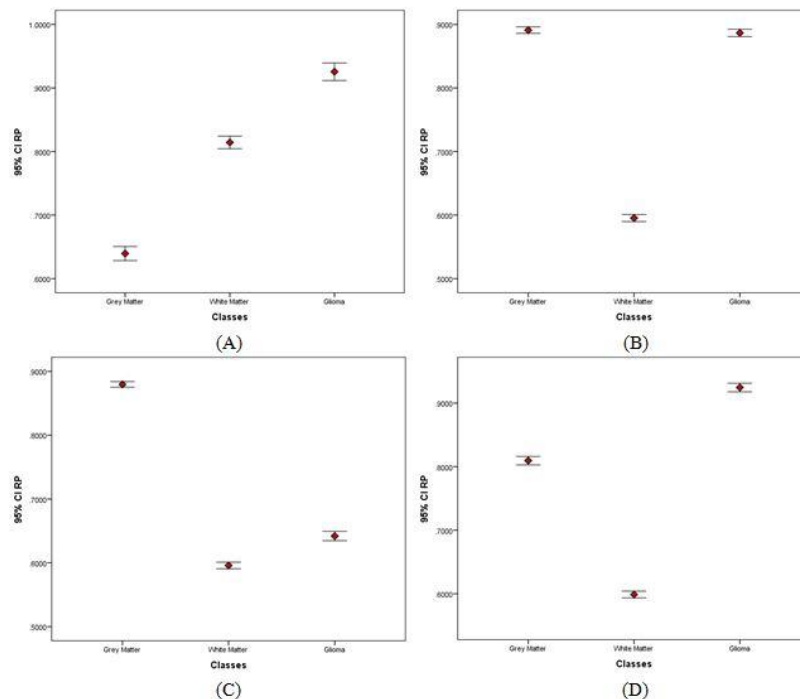


Fig (4-14): Error bar plot show the discriminate power of the RP textural feature distribution for the selected classes on T1(A), T2(B), FLAIR(C) and T1+C(D) images for Glioma patients

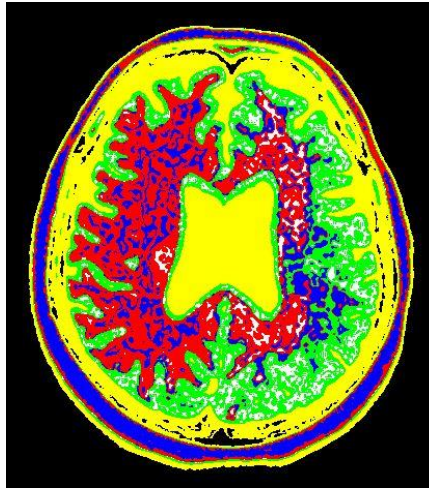


Fig (4-15): shows classification map in T1 image for MS patient

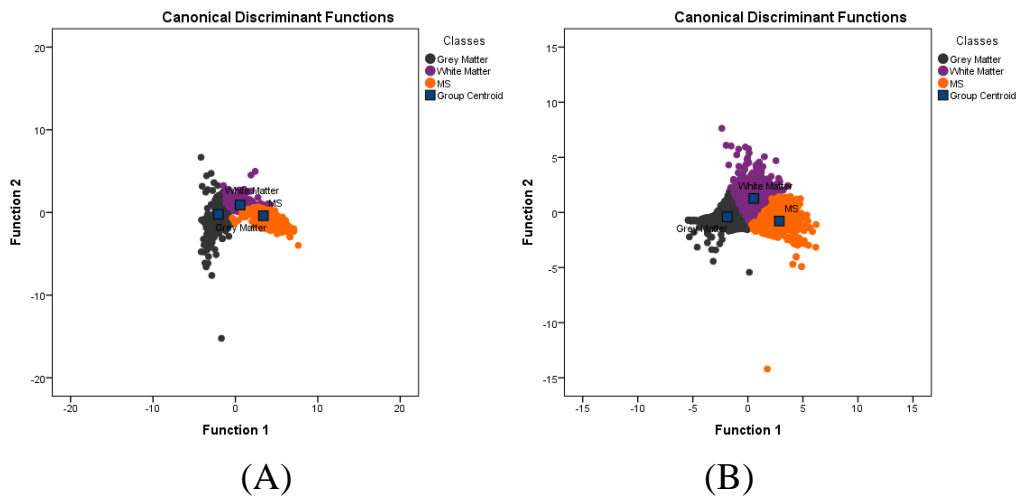


Fig (4-16): Scatter plot demonstrate the classification of brain tissues using linear discriminate analysis on T1 images for MS patients. First order features (A) and higher order features (B)

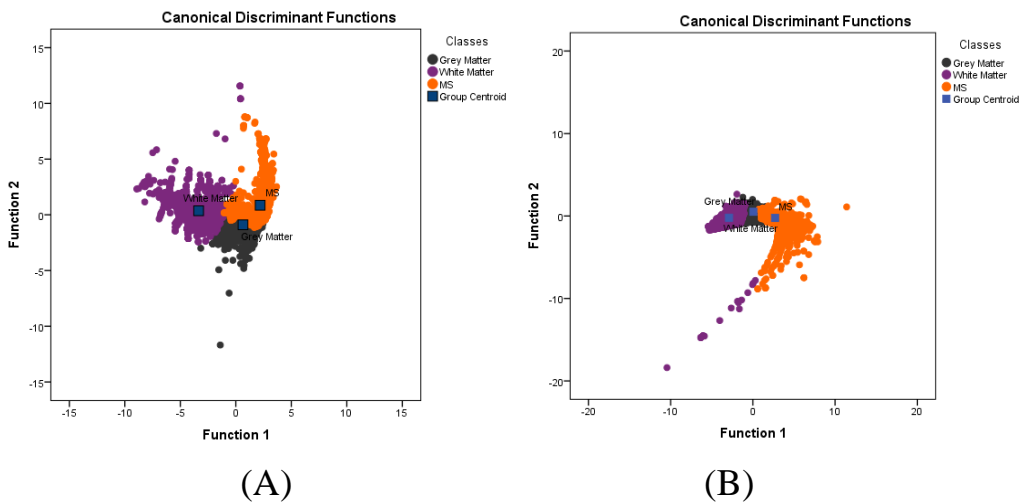


Fig (4-17): Scatter plot demonstrate the classification of brain tissues using linear discriminate analysis on T2 images for MS patients. First order features (A) and higher order features (B)

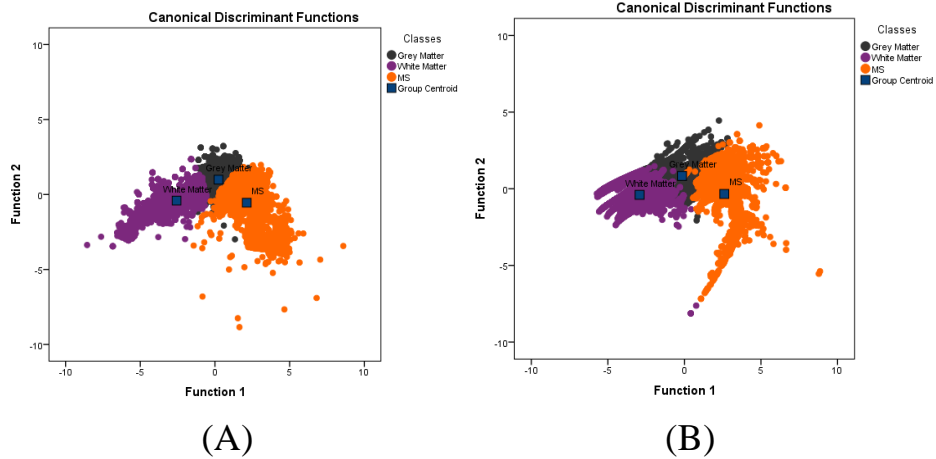


Fig (4-18): Scatter plot demonstrate the classification of brain tissues using linear discriminate analysis on FLAIR images for MS patients. First order features (A) and higher order features (B)

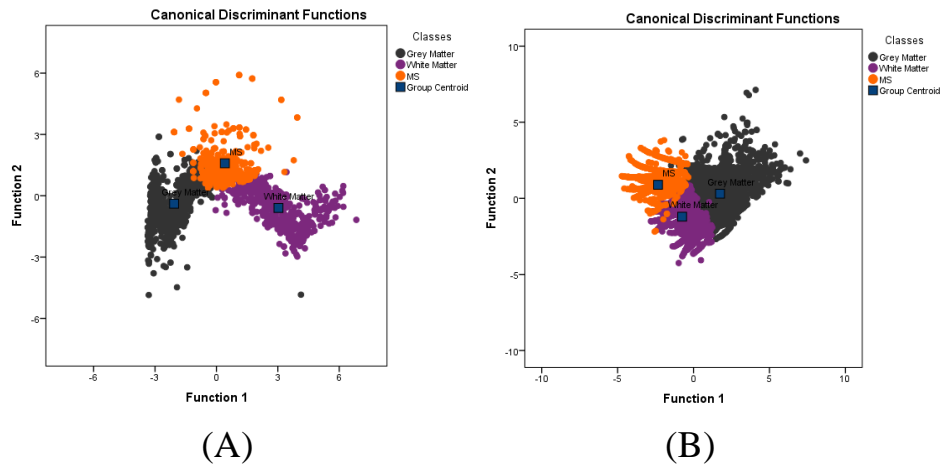


Fig (4-19): Scatter plot demonstrate the classification of brain tissues using linear discriminate analysis on T1+C images for MS patients. First order features (A) and higher order features (B)

Table 4-9: Cross-tabulation shows the classification results of the tissues using linear discriminate analysis for first order features on T1 images for MS patients.

Classes			Predicted Group Membership			Total
			Grey Matter	White Matter	MS	
Original	Count	Grey Matter	1115	34	0	1149
		White Matter	4	515	25	544
		MS	3	90	511	604
	%	Grey Matter	97.0	3.0	.0	100.0
		White Matter	.7	94.7	4.6	100.0
		MS	.5	14.9	84.6	100.0
a. 93.2% of original grouped cases correctly classified.						

Table 4-10: Cross-tabulation shows the classification results the tissues using linear discriminate analysis for first order features on T2 images for MS patients.

Classes			Predicted Group Membership			Total
			Grey Matter	White Matter	MS	
Original	Count	Grey Matter	4223	19	201	4443
		White Matter	37	2980	13	3030
		MS	508	0	2814	3322
	%	Grey Matter	95.0	.4	4.5	100.0
		White Matter	1.2	98.3	.4	100.0
		MS	15.3	.0	84.7	100.0
a. 92.8% of original grouped cases correctly classified.						

Table 4-11: Cross-tabulation shows the classification results of first order features from the classes using linear discriminate analysis for first order features on FLAIR images for MS patients.

Classes			Predicted Group Membership			Total
			Grey Matter	White Matter	MS	
Original	Count	Grey Matter	4325	1	36	4362
		White Matter	733	3554	0	4287
		MS	876	10	3809	4695
	%	Grey Matter	99.2	.0	.8	100.0
		White Matter	17.1	82.9	.0	100.0
		MS	18.7	.2	81.1	100.0
a. 87.6% of original grouped cases correctly classified.						

Table 4-12: Cross-tabulation shows the classification results of the tissues using linear discriminate analysis for first order features on T1+C images for MS patients.

Classes			Predicted Group Membership			Total
			Grey Matter	White Matter	MS	
Original	Count	Grey Matter	775	1	81	857
		White Matter	1	472	57	530
		MS	1	2	406	409
	%	Grey Matter	90.4	.1	9.5	100.0
		White Matter	.2	89.1	10.8	100.0
		MS	.2	.5	99.3	100.0
a. 92.0% of original grouped cases correctly classified.						

Table 4-13: Cross-tabulation shows the classification results of the tissues using linear discriminate analysis for higher order features on T1 images for MS patients.

Classes			Predicted Group Membership			Total
			Grey Matter	White Matter	MS	
Original	Count	Grey Matter	1114	25	1	1140
		White Matter	10	697	22	729
		MS	4	10	596	610
	%	Grey Matter	97.7	2.2	.1	100.0
		White Matter	1.4	95.6	3.0	100.0
		MS	.7	1.6	97.7	100.0
a. 97.1% of original grouped cases correctly classified.						

Table 4-14: Cross-tabulation shows the classification results of the tissues using linear discriminate analysis for higher order features on T2 images for MS patients.

Classes			Predicted Group Membership			Total
			Grey Matter	White Matter	MS	
Original	Count	Grey Matter	3278	23	39	3340
		White Matter	379	3348	3	3730
		MS	514	0	3427	3941
	%	Grey Matter	98.1	.7	1.2	100.0
		White Matter	10.2	89.8	.1	100.0
		MS	13.0	.0	87.0	100.0
a. 91.3% of original grouped cases correctly classified.						

Table 4-15: Cross-tabulation shows the classification results of the tissues using linear discriminate analysis for higher order features on FLAIR images for MS patients.

Classes			Predicted Group Membership			Total
			Grey Matter	White Matter	MS	
Original	Count	Grey Matter	3921	204	26	4151
		White Matter	401	3949	4	4354
		MS	446	0	4691	5137
	%	Grey Matter	94.5	4.9	.6	100.0
		White Matter	9.2	90.7	.1	100.0
		MS	8.7	.0	91.3	100.0
a. 92.1% of original grouped cases correctly classified.						

Table 4-16: Cross-tabulation shows the classification results of the tissues using linear discriminate analysis for higher order features on T1+C images for MS patients.

Classes			Predicted Group Membership			Total
			Grey Matter	White Matter	MS	
Original	Count	Grey Matter	3107	252	93	3452
		White Matter	5	2110	127	2242
		MS	0	13	1845	1858
	%	Grey Matter	90.0	7.3	2.7	100.0
		White Matter	.2	94.1	5.7	100.0
		MS	.0	.7	99.3	100.0

a. 93.5% of original grouped cases correctly classified.

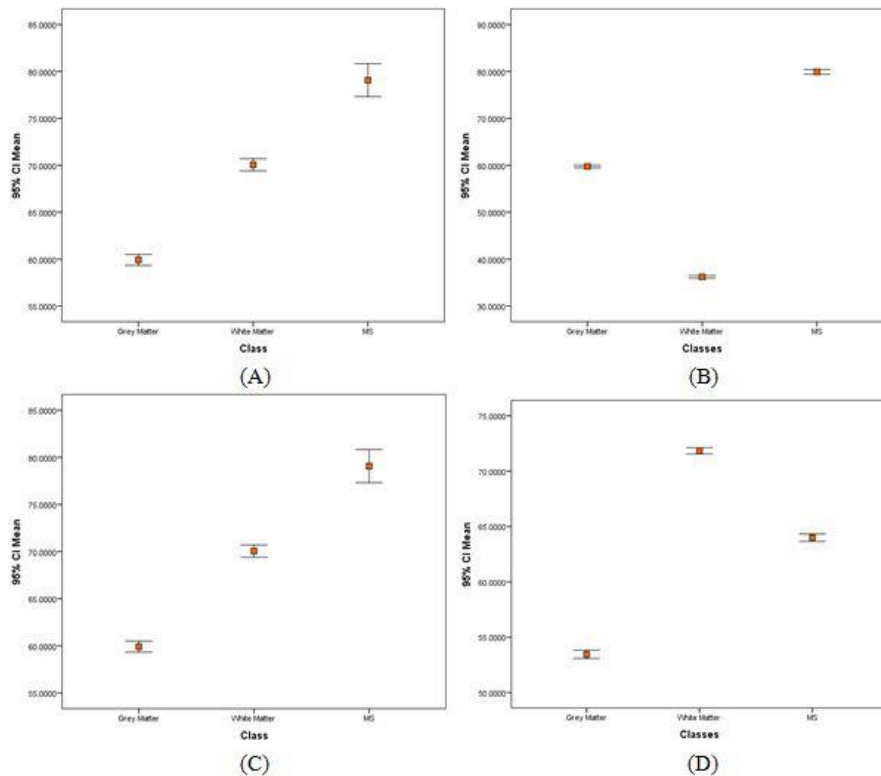


Fig (4-20): Error bar plot show the discriminate power of the Mean textural feature distribution for the selected classes on T1(A), T2(B), FLAIR(C) and T1+C(D) images for MS patients

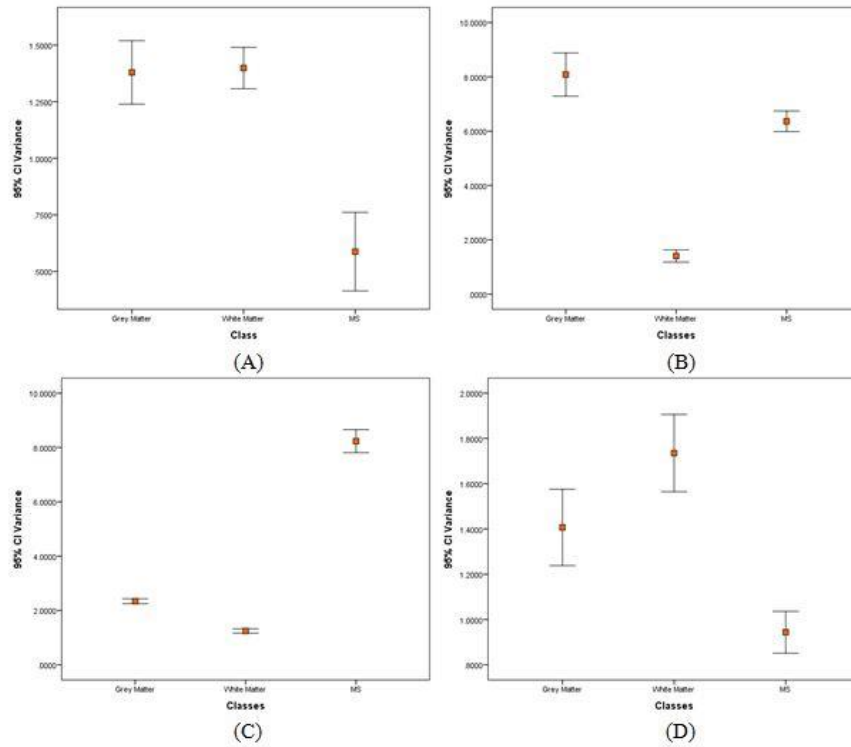


Fig (4-21): Error bar plot show the discriminate power of the Variance textural feature distribution for the selected classes on T1(A), T2(B), FLAIR(C) and T1+C(D) images for MS patients

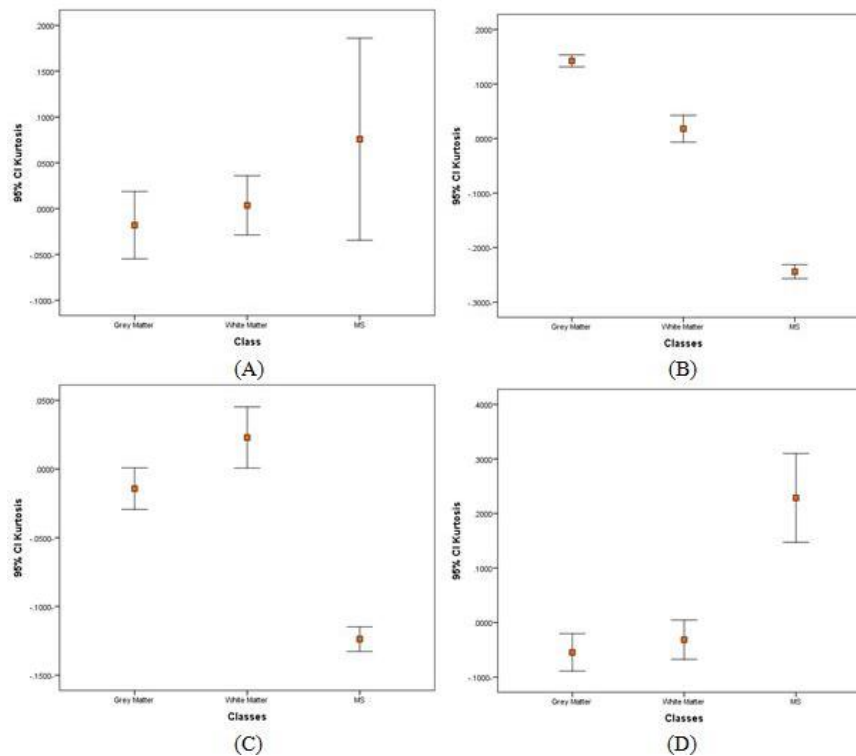


Fig (4-22): Error bar plot show the discriminate power of the Kurtosis textural feature distribution for the selected classes on T1(A), T2(B), FLAIR(C) and T1+C(D) images for MS patients

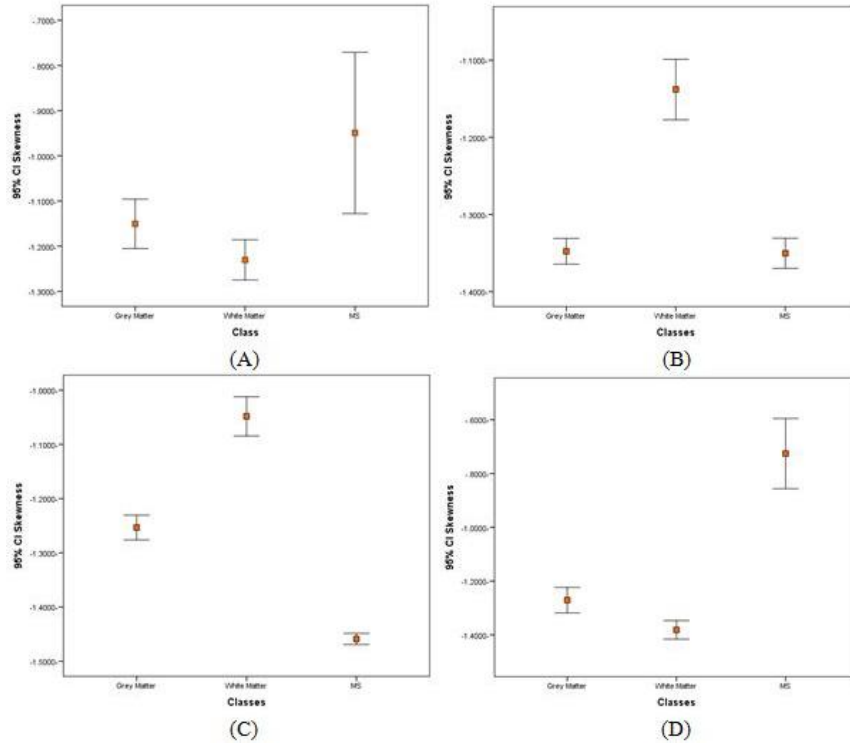


Fig (4-23): Error bar plot show the discriminate power of the Skewness textural feature distribution for the selected classes on T1(A), T2(B), FLAIR(C) and T1+C(D) images for MS patients

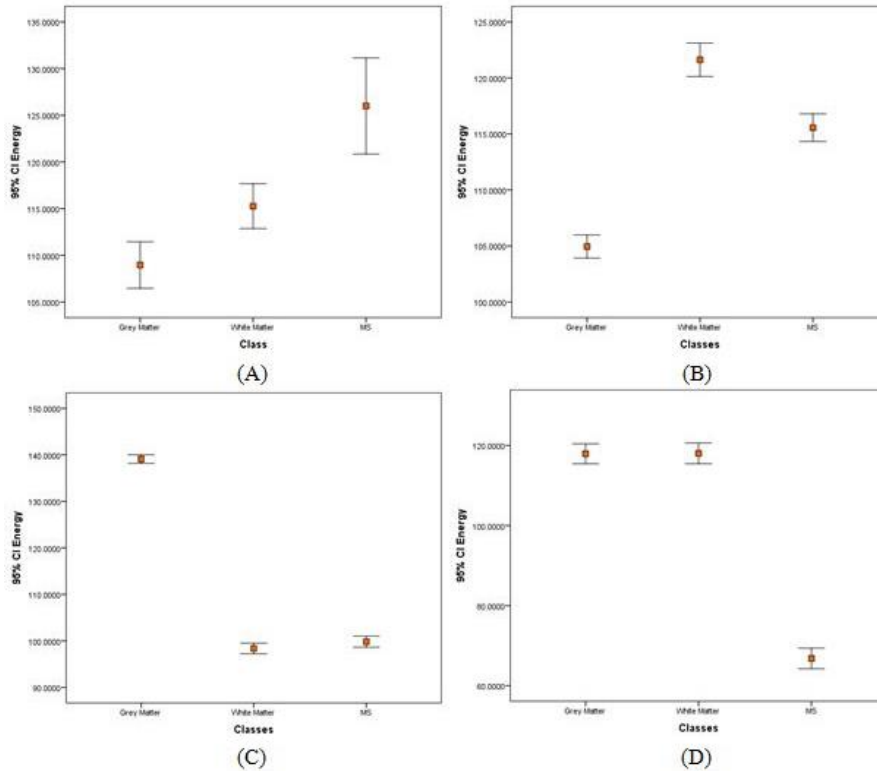


Fig (4-24): Error bar plot show the discriminate power of the Energy textural feature distribution for the selected classes on T1(A), T2(B), FLAIR(C) and T1+C(D) images for MS patients

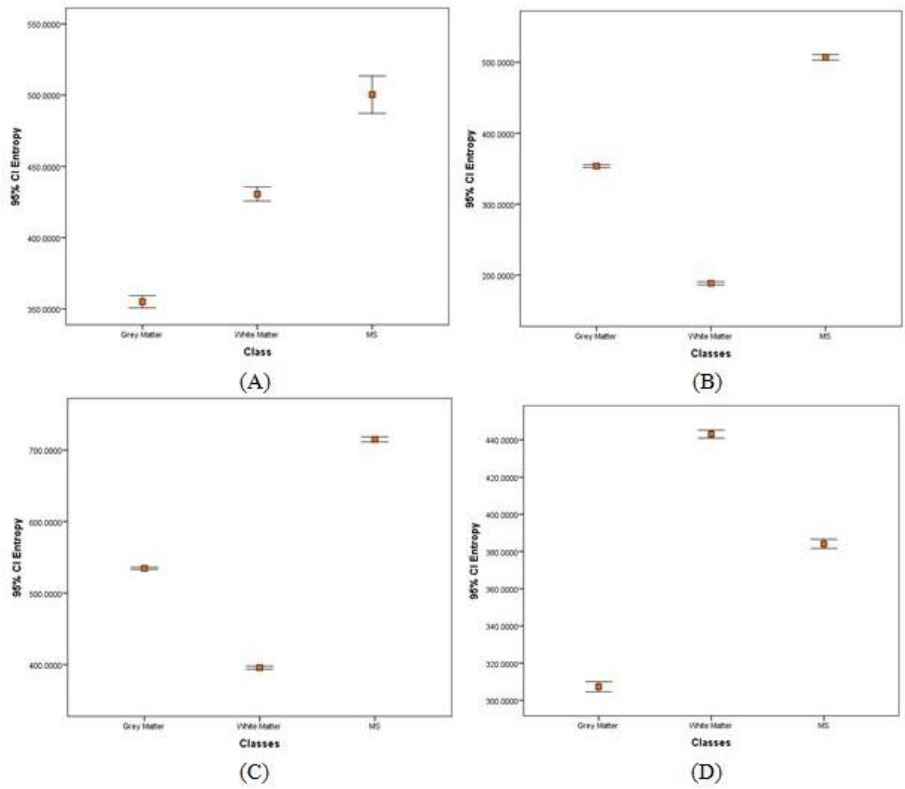


Fig (4-25): Error bar plot show the discriminate power of the Entropy textural feature distribution for the selected classes on T1(A), T2(B), FLAIR(C) and T1+C(D) images for MS patients

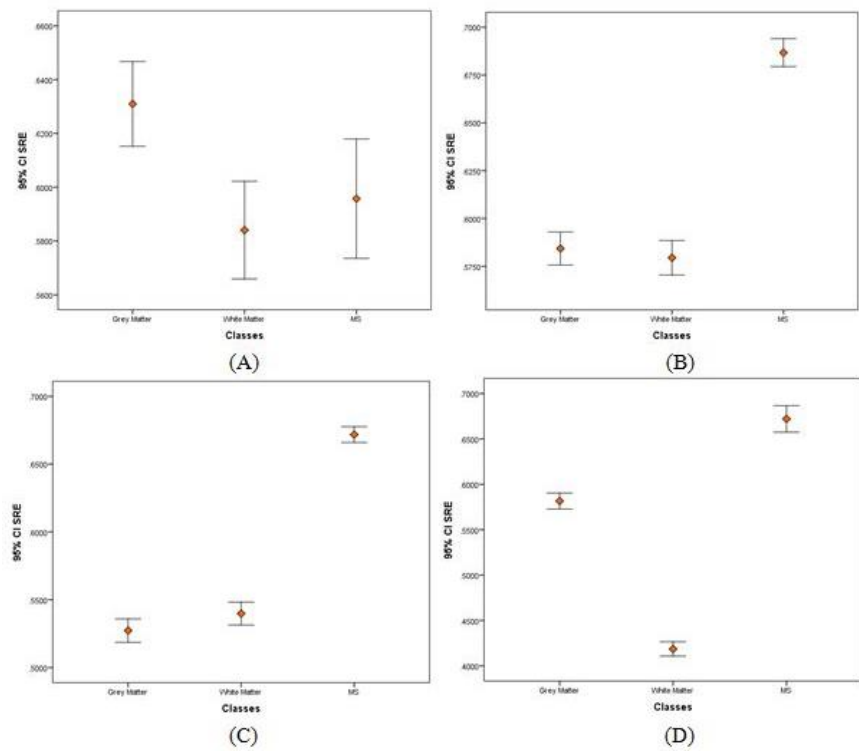


Fig (4-26): Error bar plot show the discriminate power of the SRE textural feature distribution for the selected classes on T1(A), T2(B), FLAIR(C) and T1+C(D) images for MS patients

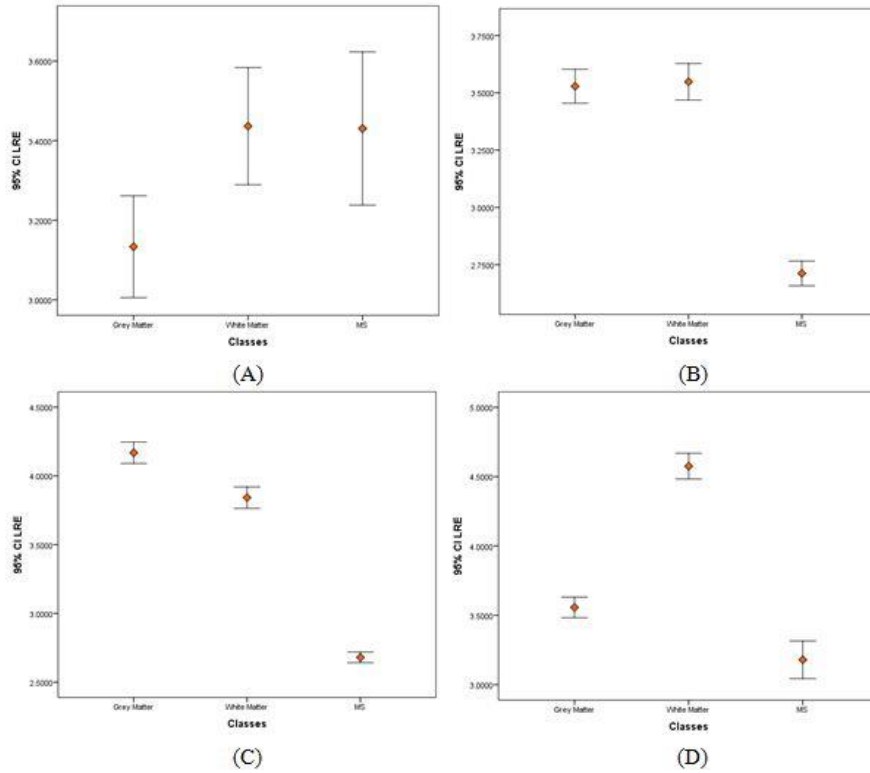


Fig (4-27): Error bar plot show the discriminate power of the LRE textural feature distribution for the selected classes on T1(A), T2(B), FLAIR(C) and T1+C(D) images for MS patients

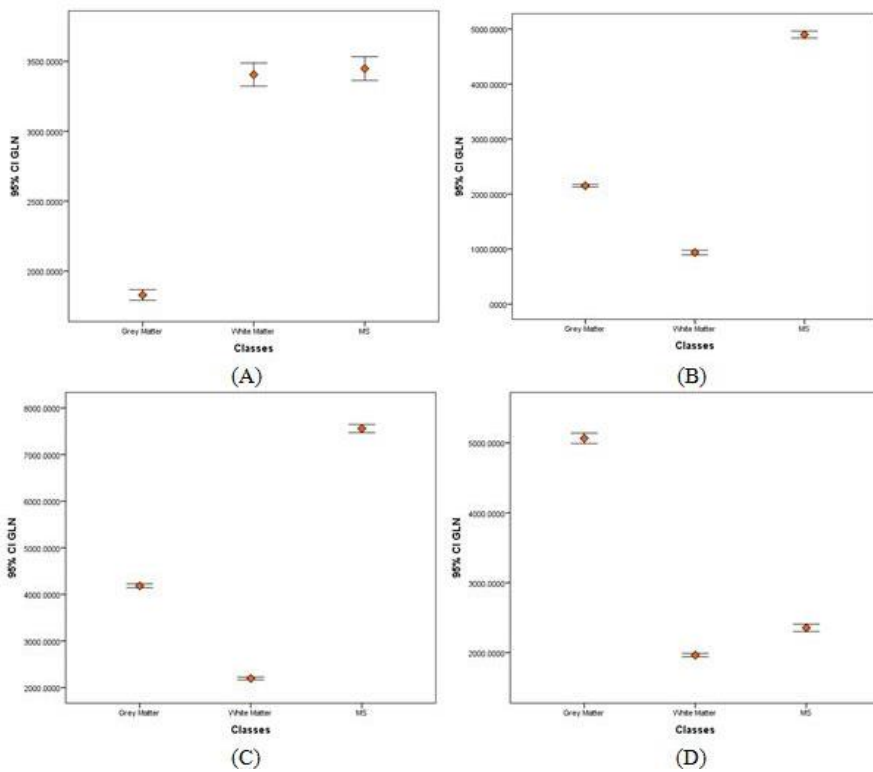


Fig (4-28): Error bar plot show the discriminate power of the GLN textural feature distribution for the selected classes on T1(A), T2(B), FLAIR(C) and T1+C(D) images for MS patients

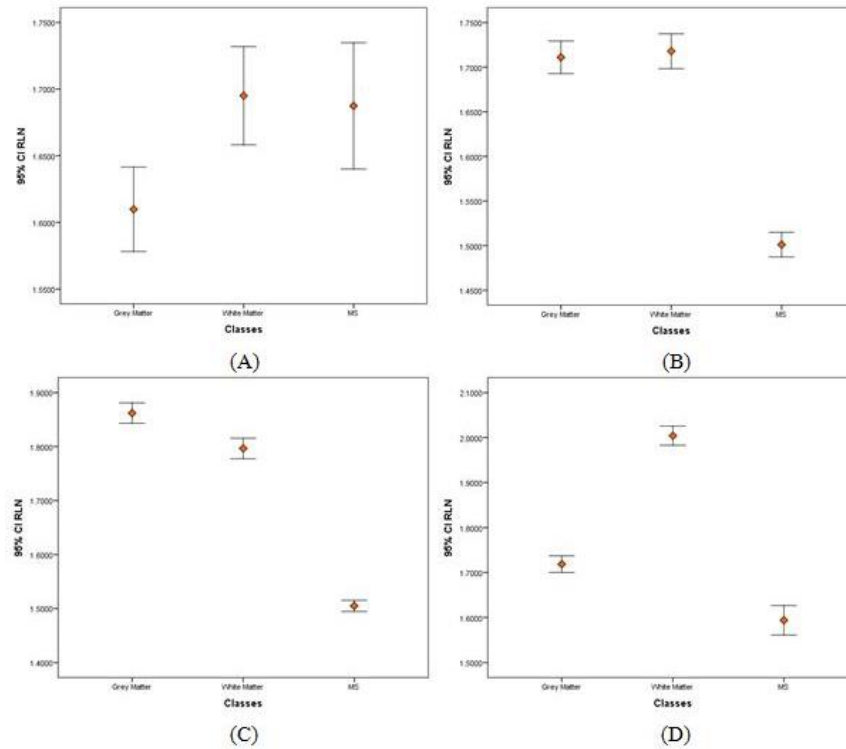


Fig (4-29): Error bar plot show the discriminate power of the RLN textural feature distribution for the selected classes on T1(A), T2(B), FLAIR(C) and T1+C(D) images for MS patients

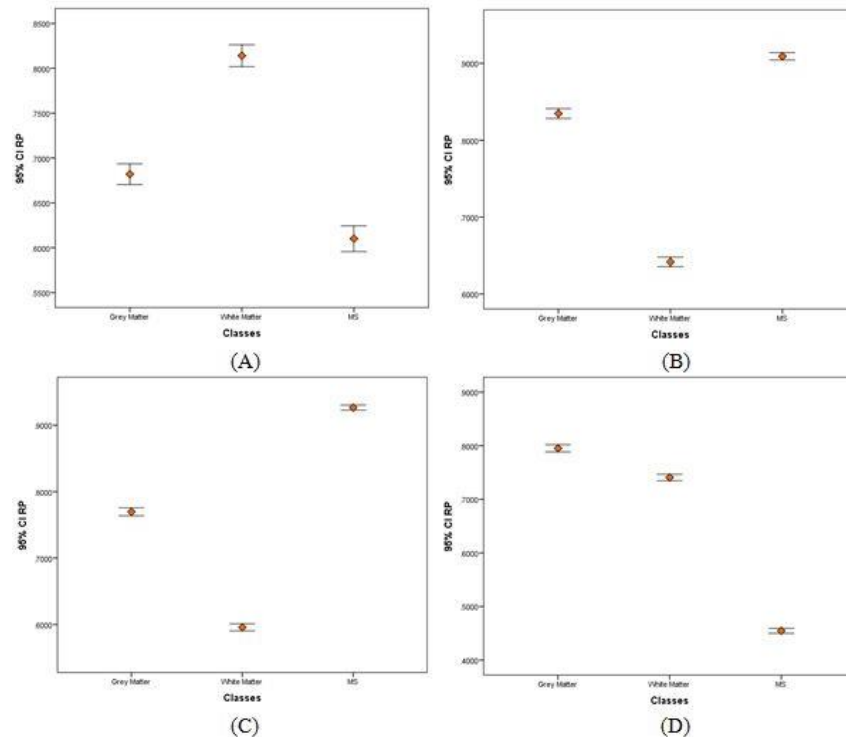


Fig (4-30): Error bar plot show the discriminate power of the RP textural feature distribution for the selected classes on T1(A), T2(B), FLAIR(C) and T1+C(D) images for MS patients

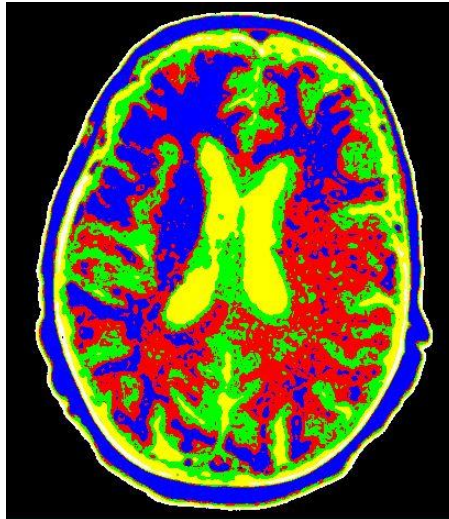


Fig (4-31): shows classification map in T1 image for SVD patient

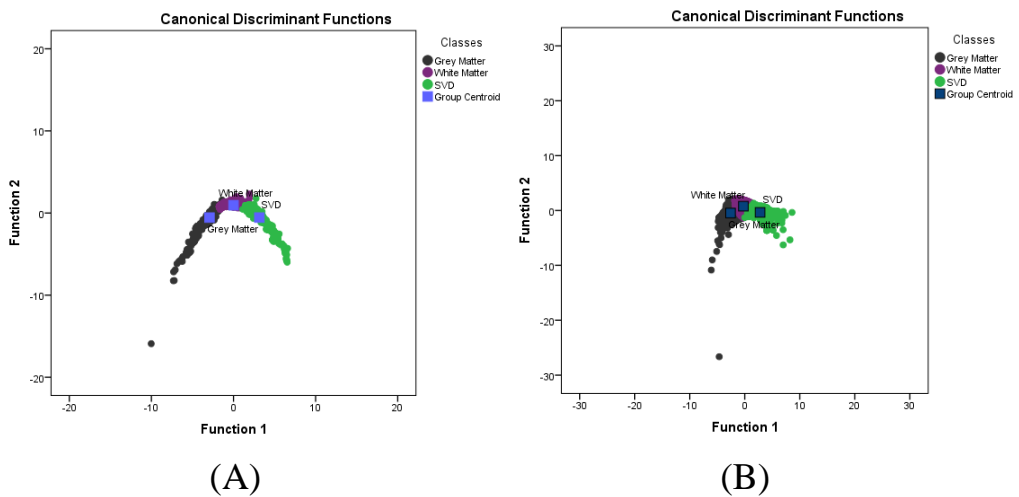


Fig (4-32): Scatter plot demonstrate the classification of brain tissues using linear discriminate analysis on T1 images for SVD patients. First order features (A) and higher order features (B)

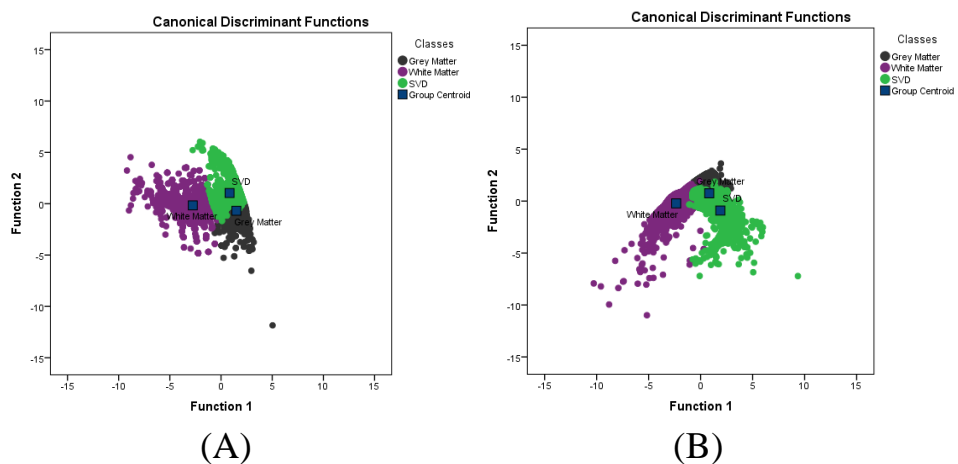


Fig (4-33): Scatter plot demonstrate the classification of brain tissues using linear discriminate analysis on T2 images for SVD patients. First order features (A) and higher order features (B)

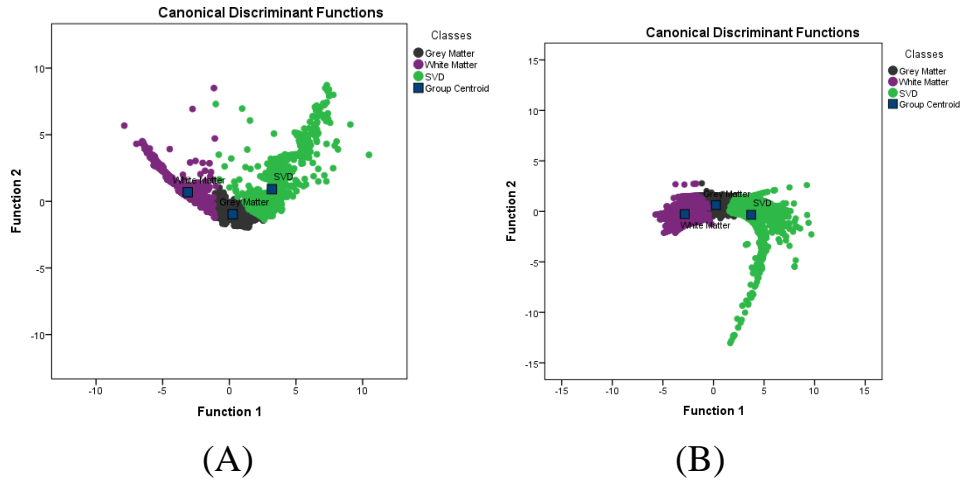


Fig (4-34): Scatter plot demonstrate the classification of brain tissues using linear discriminate analysis on FLAIR images for SVD patients. First order features (A) and higher order features (B)

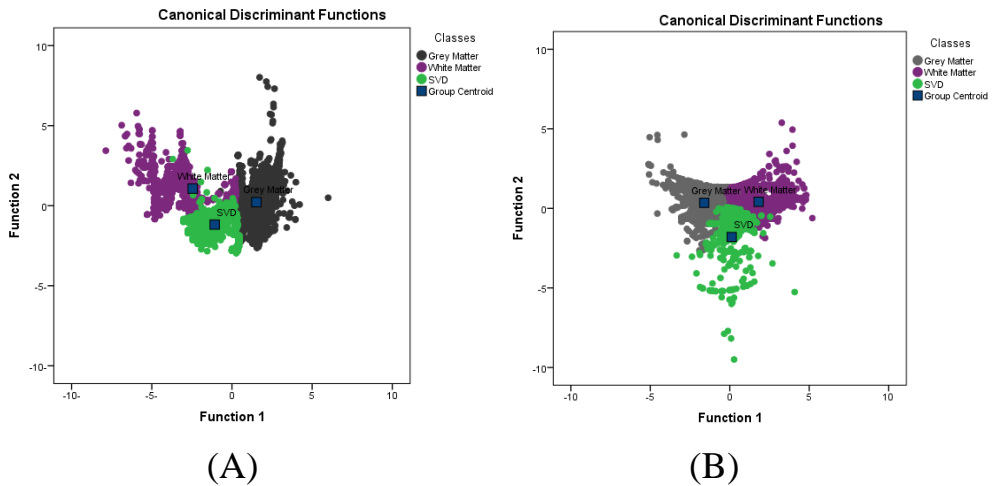


Fig (4-35): Scatter plot demonstrate the classification of brain tissues using linear discriminate analysis on T1+C images for SVD patients. First order features (A) and higher order features (B)

Table 4-17: Cross-tabulation shows the classification results tissues using linear discriminate analysis for first order features on T1 images for SVD patients.

Classes			Predicted Group Membership			Total
			Grey Matter	White Matter	SVD	
Original	Count	Grey Matter	993	38	0	1031
		White Matter	9	1152	0	1161
		SVD	0	41	917	958
	%	Grey Matter	96.3	3.7	.0	100.0
		White Matter	.8	99.2	.0	100.0
		SVD	.0	4.3	95.7	100.0
a. 97.2% of original grouped cases correctly classified.						

Table 4-18: Cross-tabulation shows the classification results tissues using linear discriminate analysis for first order features on T2 images for SVD patients.

Classes			Predicted Group Membership			Total
			Grey Matter	White Matter	SVD	
Original	Count	Grey Matter	3393	0	389	3782
		White Matter	35	2886	25	2946
		SVD	428	1	2519	2948
	%	Grey Matter	89.7	.0	10.3	100.0
		White Matter	1.2	98.0	.8	100.0
		SVD	14.5	.0	85.4	100.0
a. 90.9% of original grouped cases correctly classified.						

Table 4-19: Cross-tabulation shows the classification results tissues using linear discriminate analysis for first order features on FLAIR images for SVD patients.

Classes			Predicted Group Membership			Total
			Grey Matter	White Matter	SVD	
Original	Count	Grey Matter	4575	20	2	4597
		White Matter	280	2780	0	3060
		SVD	227	5	2388	2620
	%	Grey Matter	99.5	.4	.0	100.0
		White Matter	9.2	90.8	.0	100.0
		SVD	8.7	.2	91.1	100.0
a. 94.8% of original grouped cases correctly classified.						

Table 4-20: Cross-tabulation shows the classification results tissues using linear discriminate analysis for first order features on T1+C images for SVD patients.

Classes			Predicted Group Membership			Total
			Grey Matter	White Matter	SVD	
Original	Count	Grey Matter	3632	1	165	3798
		White Matter	273	1097	103	1473
		SVD	39	12	1982	2033
	%	Grey Matter	95.6	.0	4.3	100.0
		White Matter	18.5	74.5	7.0	100.0
		SVD	1.9	.6	97.5	100.0
a. 91.9% of original grouped cases correctly classified.						

Table 4-21: Cross-tabulation shows the classification results tissues using linear discriminate analysis for higher order features on T1 images for SVD patients.

Classes			Predicted Group Membership			Total
			Grey Matter	White Matter	SVD	
Original	Count	Grey Matter	993	56	0	1049
		White Matter	14	1074	6	1094
		SVD	0	94	977	1071
	%	Grey Matter	94.7	5.3	.0	100.0
		White Matter	1.3	98.2	.5	100.0
		SVD	.0	8.8	91.2	100.0
a. 94.7% of original grouped cases correctly classified.						

Table 4-22: Cross-tabulation shows the classification results tissues using linear discriminate analysis for higher order features on T2 images for SVD patients.

Classes			Predicted Group Membership			Total
			Grey Matter	White Matter	SVD	
Original	Count	Grey Matter	3301	149	557	4007
		White Matter	118	3281	7	3406
		SVD	632	4	1845	2481
	%	Grey Matter	82.4	3.7	13.9	100.0
		White Matter	3.5	96.3	.2	100.0
		SVD	25.5	.2	74.4	100.0
a. 85.2% of original grouped cases correctly classified.						

Table 4-23: Cross-tabulation shows the classification results tissues using linear discriminate analysis for higher order features on FLAIR images for SVD patients.

Classes			Predicted Group Membership			Total
			Grey Matter	White Matter	SVD	
Original	Count	Grey Matter	3336	62	17	3415
		White Matter	151	4022	0	4173
		SVD	159	0	2790	2949
	%	Grey Matter	97.7	1.8	.5	100.0
		White Matter	3.6	96.4	.0	100.0
		SVD	5.4	.0	94.6	100.0
a. 96.3% of original grouped cases correctly classified.						

Table 4-24: Cross-tabulation shows the classification results tissues using linear discriminate analysis for higher order features on T1+C images for SVD patients.

Classes			Predicted Group Membership			Total
			Grey Matter	White Matter	SVD	
Original	Count	Grey Matter	930	9	37	976
		White Matter	19	817	5	841
		SVD	28	44	309	381
	%	Grey Matter	95.3	.9	3.8	100.0
		White Matter	2.3	97.1	.6	100.0
		SVD	7.3	11.5	81.1	100.0

a. 93.5% of original grouped cases correctly classified.

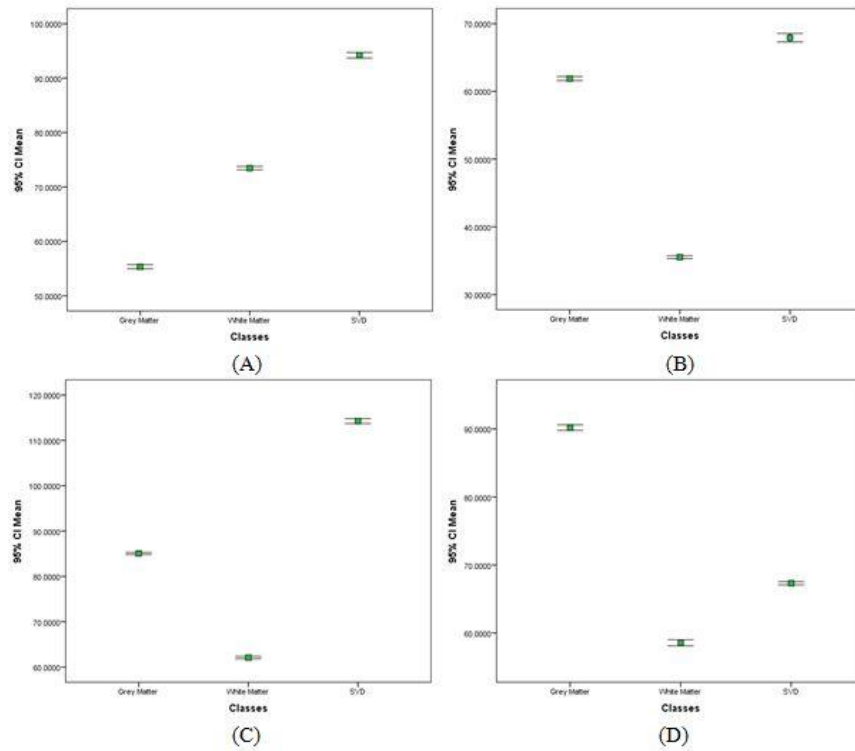


Fig (4-36): Error bar plot show the discriminate power of the Mean textural feature distribution for the selected classes on T1(A), T2(B), FLAIR(C) and T1+C(D) images for SVD patients

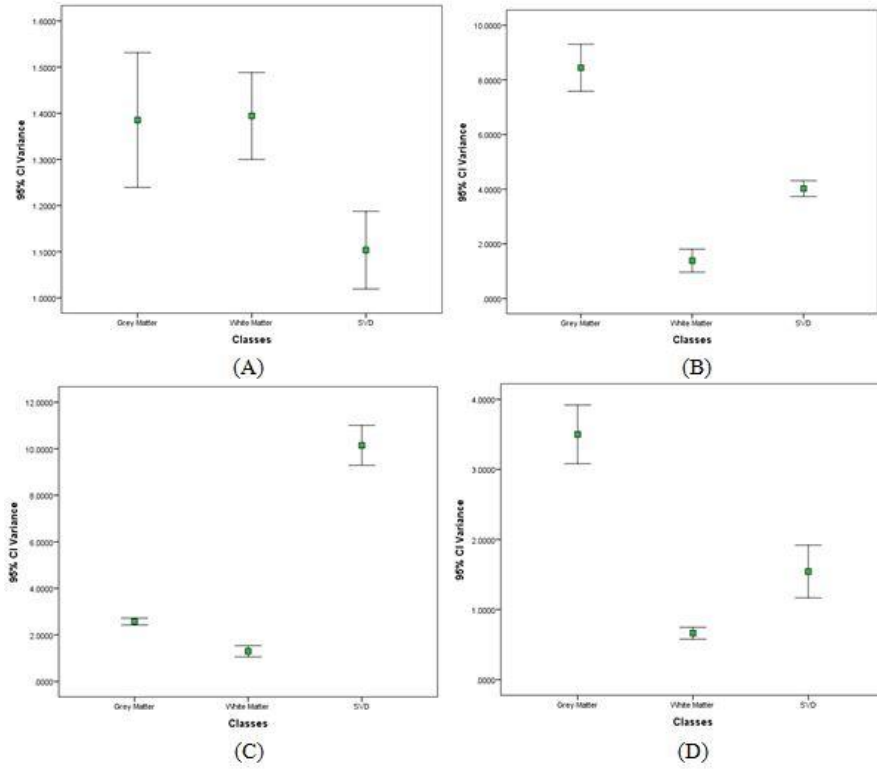


Fig (4-37): Error bar plot show the discriminate power of the Variance textural feature distribution for the selected classes on T1(A), T2(B), FLAIR(C) and T1+C(D) images for SVD patients

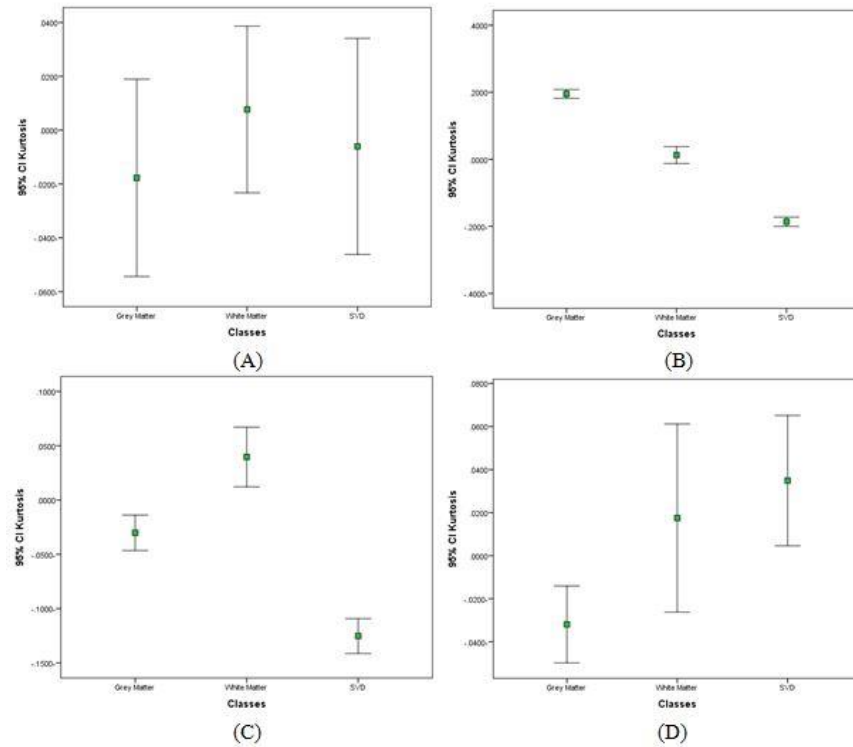


Fig (4-38): Error bar plot show the discriminate power of the Kurtosis textural feature distribution for the selected classes on T1(A), T2(B), FLAIR(C) and T1+C(D) images for SVD patients

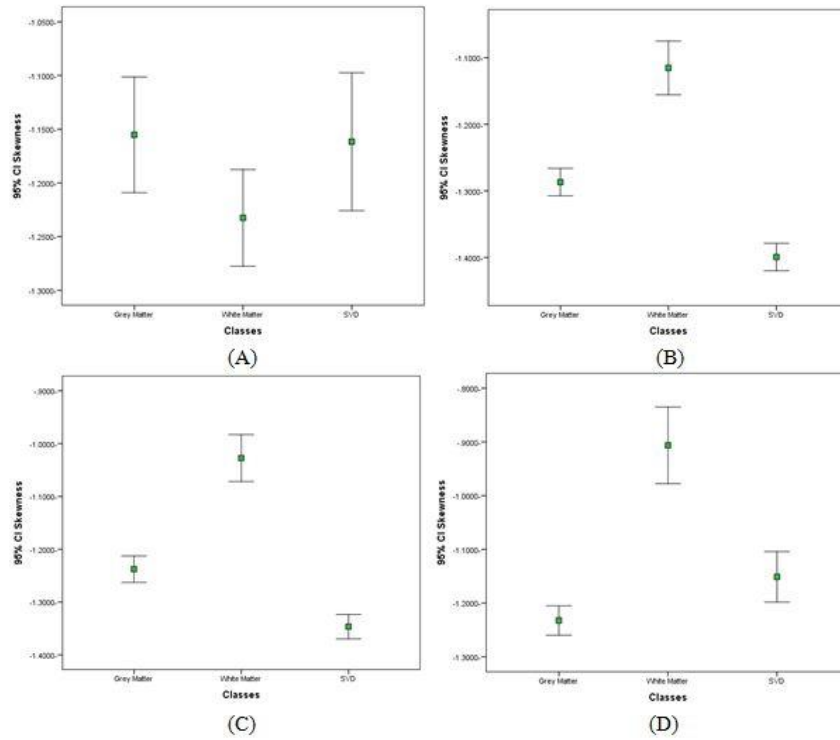


Fig (4-39): Error bar plot show the discriminate power of the Skewness textural feature distribution for the selected classes on T1(A), T2(B), FLAIR(C) and T1+C(D) images for SVD patients

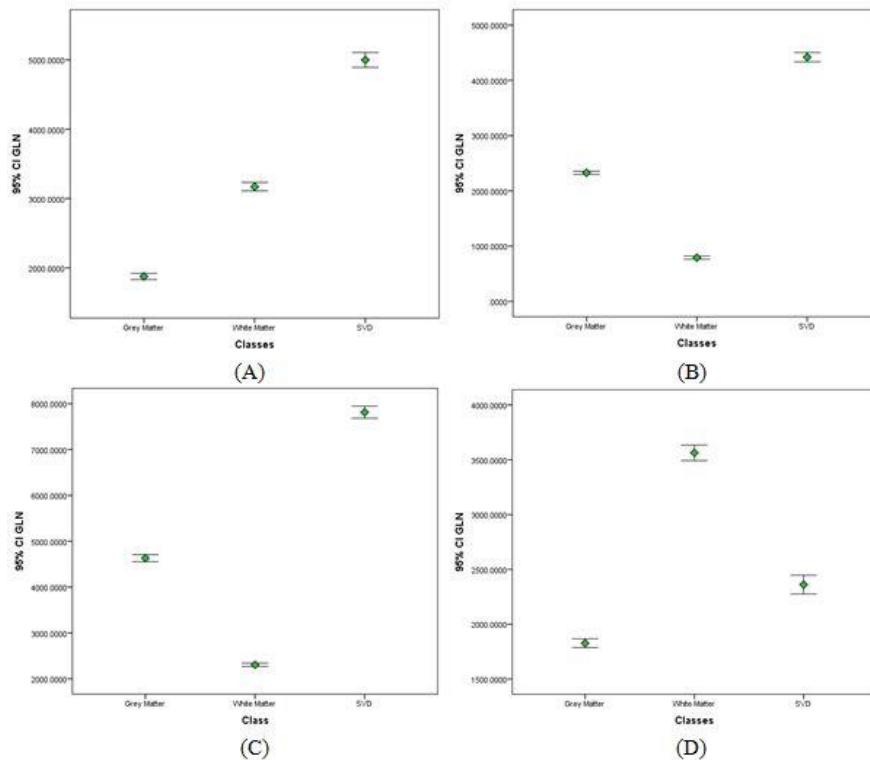


Fig (4-40): Error bar plot show the discriminate power of the Energy textural feature distribution for the selected classes on T1(A), T2(B), FLAIR(C) and T1+C(D) images for SVD patients

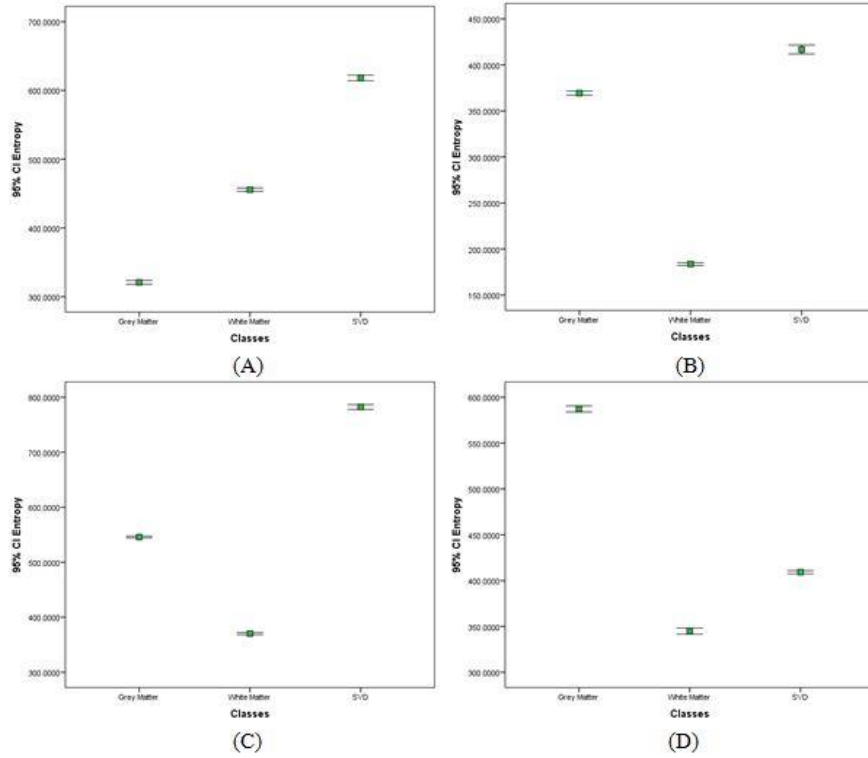


Fig (4-41): Error bar plot show the discriminate power of the Entropy textural feature distribution for the selected classes on T1(A), T2(B), FLAIR(C) and T1+C(D) images for SVD patients

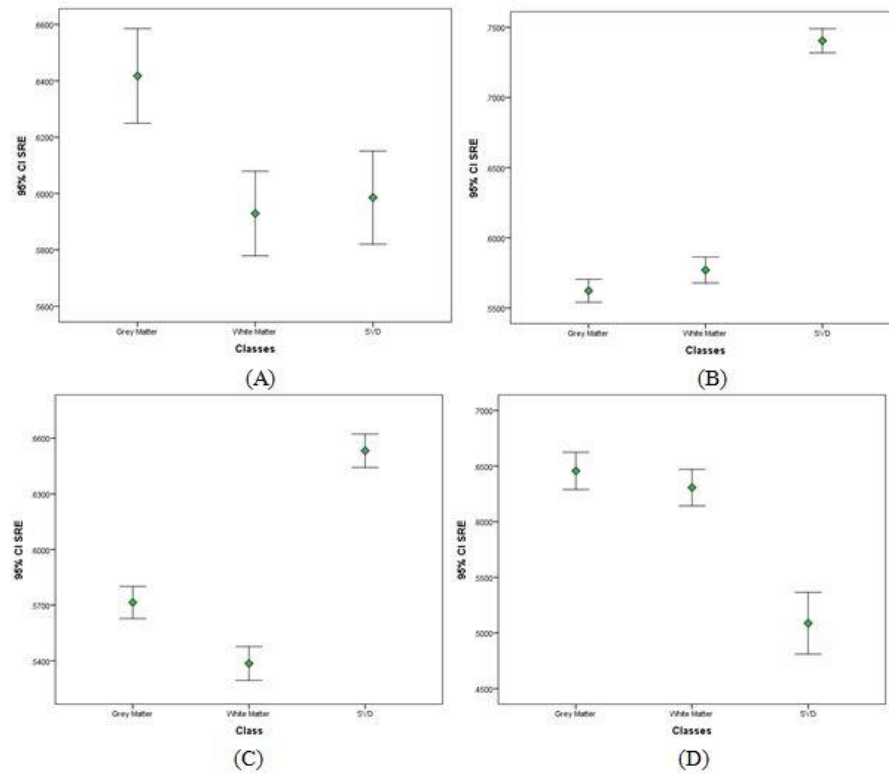


Fig (4-42): Error bar plot show the discriminate power of the SRE textural feature distribution for the selected classes on T1(A), T2(B), FLAIR(C) and T1+C(D) images for SVD patients

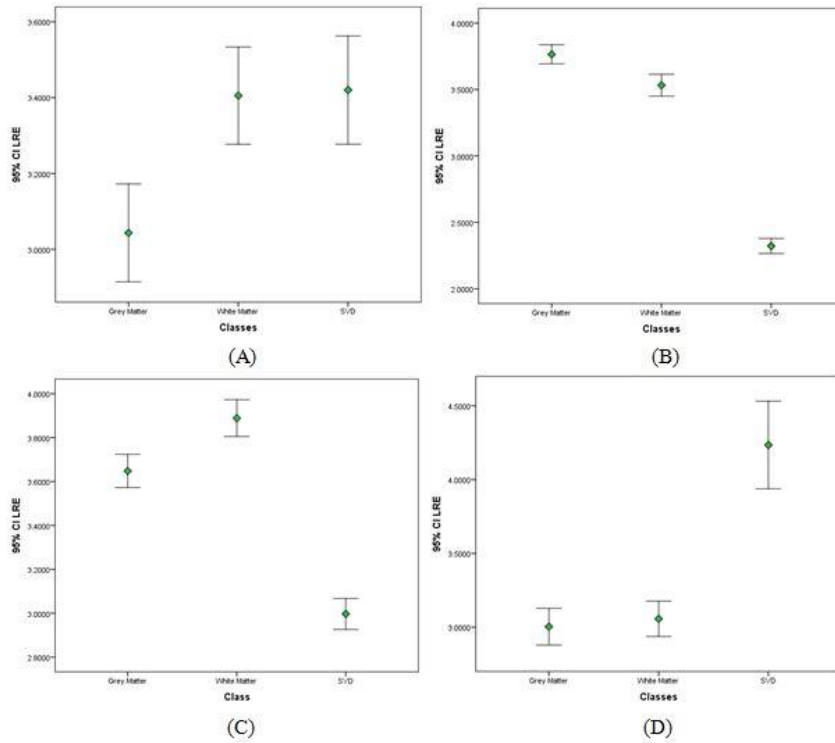


Fig (4-43): Error bar plot show the discriminate power of the LRE textural feature distribution for the selected classes on T1(A), T2(B), FLAIR(C) and T1+C(D) images for SVD patients

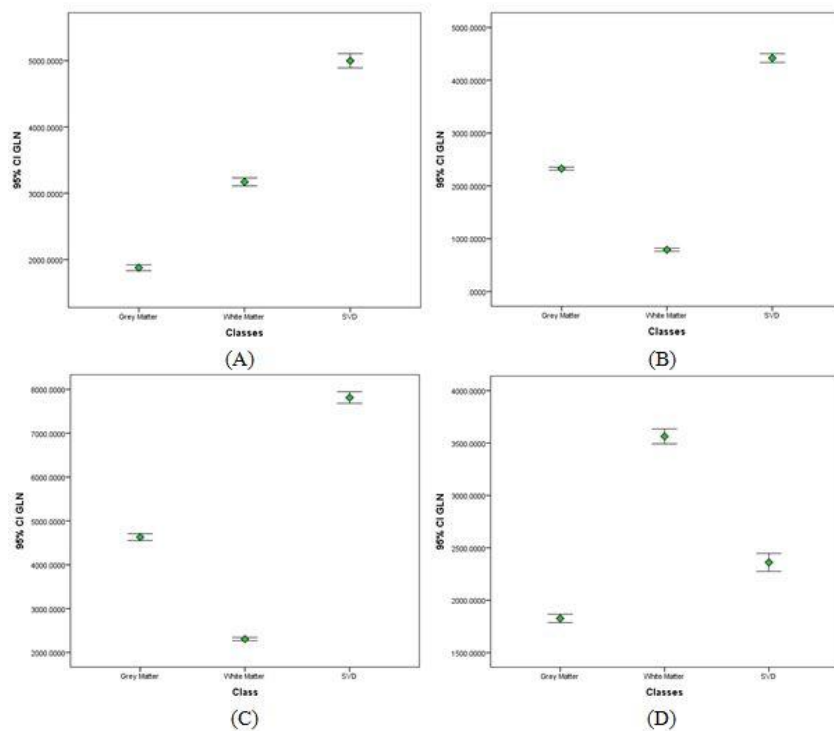


Fig (4-44): Error bar plot show the discriminate power of the GLN textural feature distribution for the selected classes on T1(A), T2(B), FLAIR(C) and T1+C(D) images for SVD patients

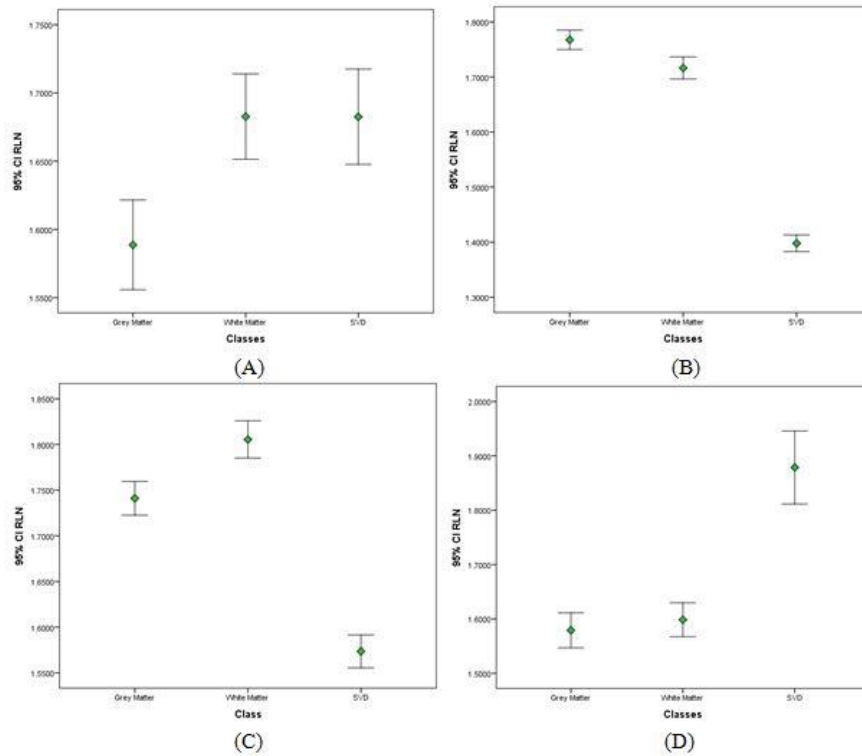


Fig (4-45): Error bar plot show the discriminate power of the RLN textural feature distribution for the selected classes on T1(A), T2(B), FLAIR(C) and T1+C(D) images for SVD patients

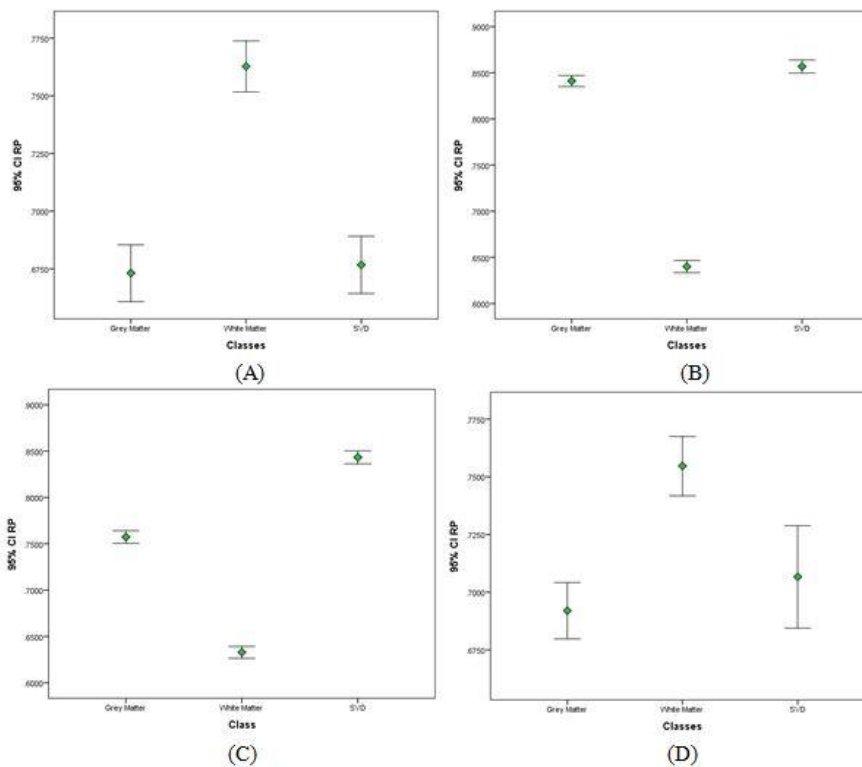


Fig (4-46): Error bar plot show the discriminate power of the RP textural feature distribution for the selected classes on T1(A), T2(B), FLAIR(C) and T1+C(D) images for SVD patients

All lesions

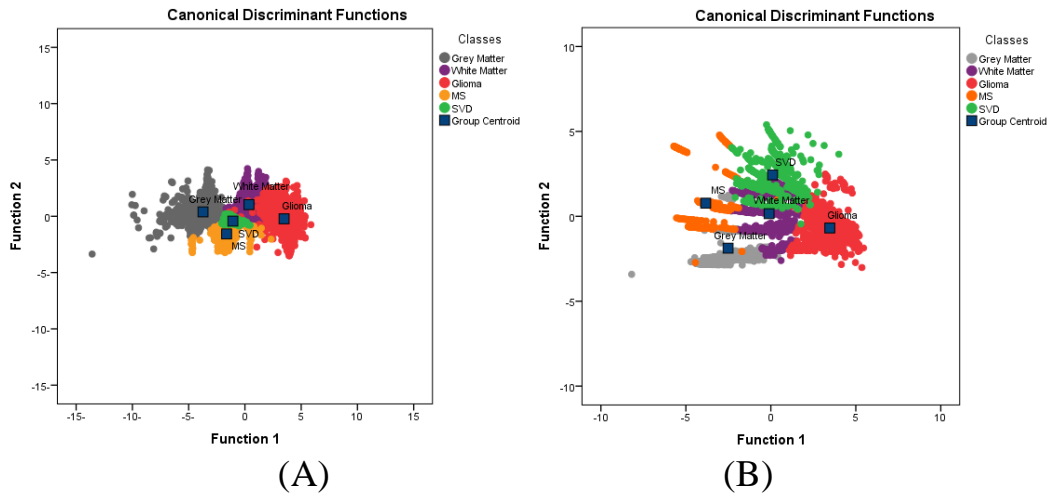


Fig (4-47): Scatter plots demonstrate the classification of white matter lesions using linear discriminate analysis on T1+C MR images for patients with Glioma, MS and SVD. First order features (A) and higher order features (B)

Table 4-25: Cross-tabulation shows the classification results of first order statistics using linear discriminate analysis on T1+C MR Images for patients with Glioma, MS and SVD.

Classes		Predicted Group Membership					Total
		Grey Matter	White Matter	Glioma	MS	SVD	
Original	Grey Matter	89.7	.0	.0	5.4	4.9	100.0
	White Matter	.0	87.3	.0	.0	12.7	100.0
	Glioma	.0	12.2	87.3	.0	.5	100.0
	MS	2.0	.3	.2	80.3	17.3	100.0
	SVD	.0	.0	.0	.0	100.0	100.0
a. 87.2% of original grouped cases correctly classified.							

Table 4-26: Cross-tabulation shows the classification results of Higher order statistics using linear discriminate analysis on T1+C MR Images for patients with Glioma, MS and SVD.

Classes		Predicted Group Membership					Total
		Grey Matter	White Matter	Glioma	MS	SVD	
Original	Grey Matter	97.5	.0	.1	1.4	1.0	100.0
	White Matter	4.6	93.1	.0	2.3	.0	100.0
	Glioma	.0	3.0	96.3	.0	.6	100.0
	MS	.7	.0	.0	93.0	6.3	100.0
	SVD	.0	.0	.0	.0	100.0	100.0
a. 96.2% of original grouped cases correctly classified.							

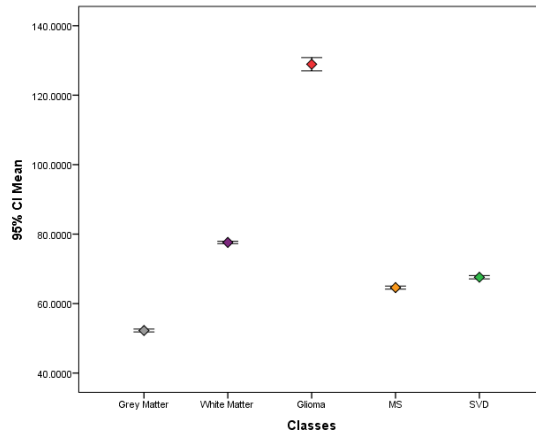


Fig (4-48): Error bar plot show the discriminate power of the Mean textural feature distribution for the selected classes on T1+C MR Images for patients with Glioma, MS and SVD.

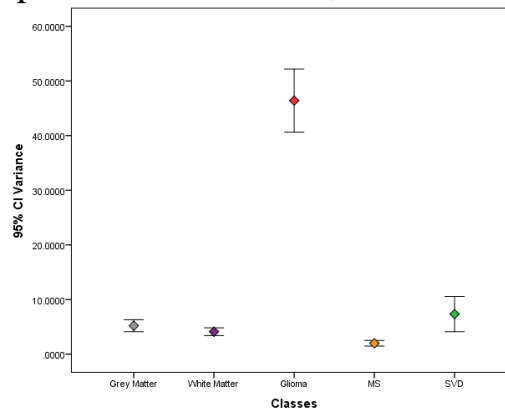


Fig (4-49): Error bar plot show the discriminate power of the Variance textural feature distribution for the selected classes on T1+C MR Images for patients with Glioma, MS and SVD.

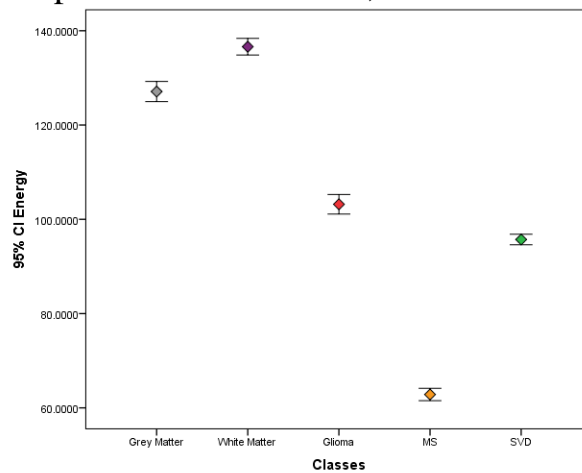


Fig (4-50): Error bar plot show the discriminate power of the Energy textural feature distribution for the selected classes on T1+C MR Images for patients with Glioma, MS and SVD.

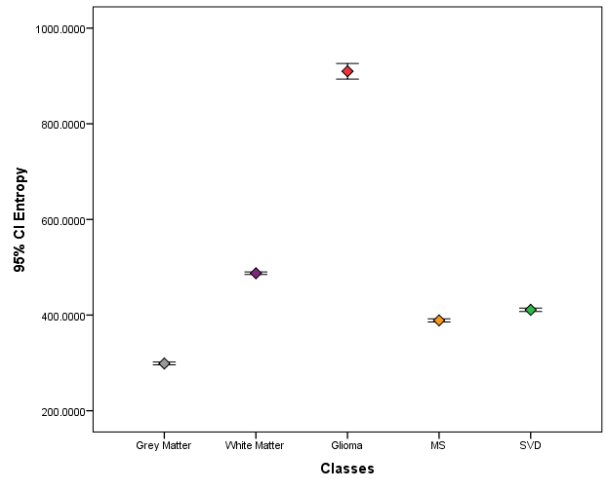


Fig (4-51): Error bar plot show the discriminate power of the Entropy textural feature distribution for the selected classes on T1+C MR Images for patients with Glioma, MS and SVD.

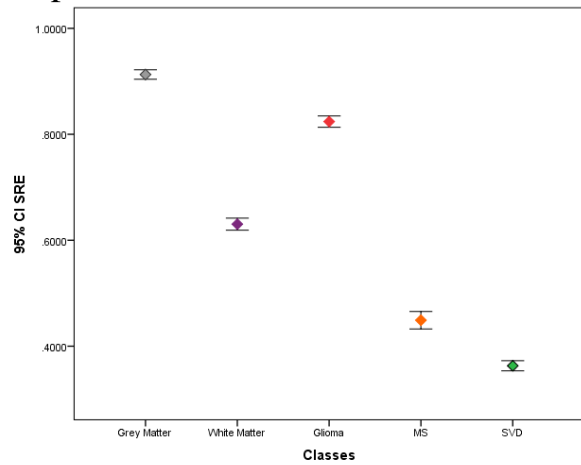


Fig (4-52): Error bar plot show the discriminate power of the SRE textural feature distribution for the selected classes on T1+C MR Images for patients with Glioma, MS and SVD.

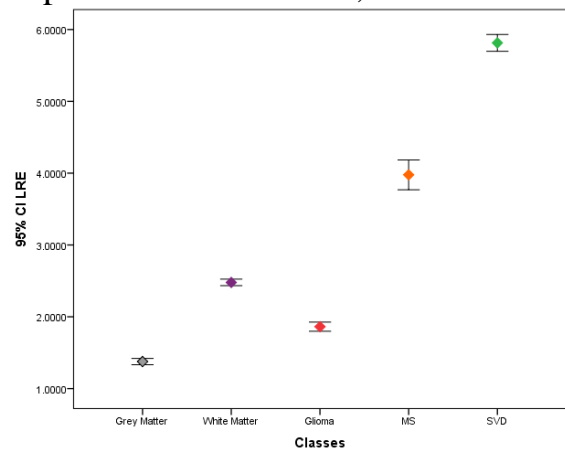


Fig (4-53): Error bar plot show the discriminate power of the LRE textural feature distribution for the selected classes on T1+C MR Images for patients with Glioma, MS and SVD.

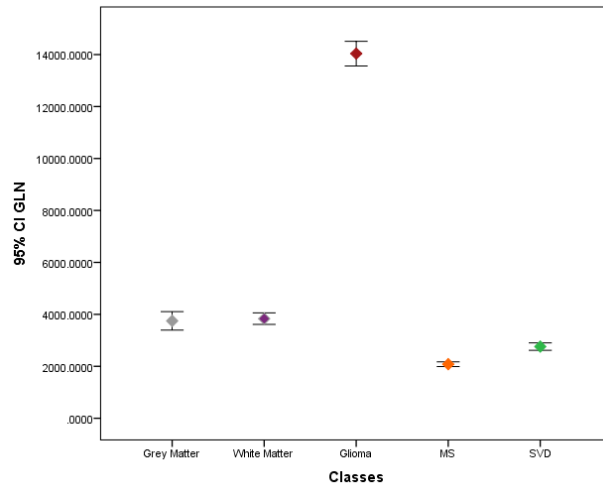


Fig (4-54): Error bar plot show the discriminate power of the GLN textural feature distribution for the selected classes on T1+C MR Images for patients with Glioma, MS and SVD.

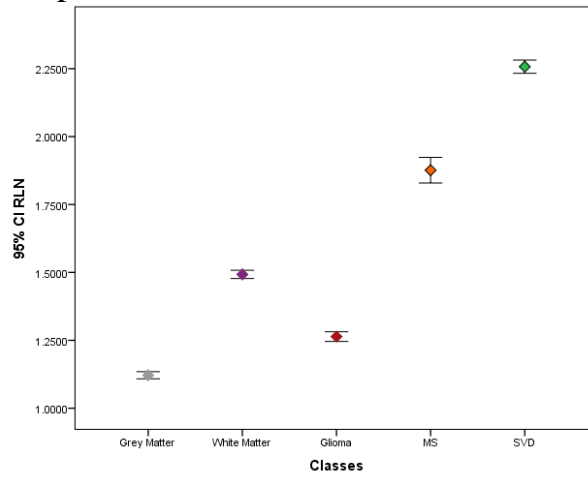


Fig (4-55): Error bar plot show the discriminate power of the RLN textural feature distribution for the selected classes on T1+C MR Images for patients with Glioma, MS and SVD.

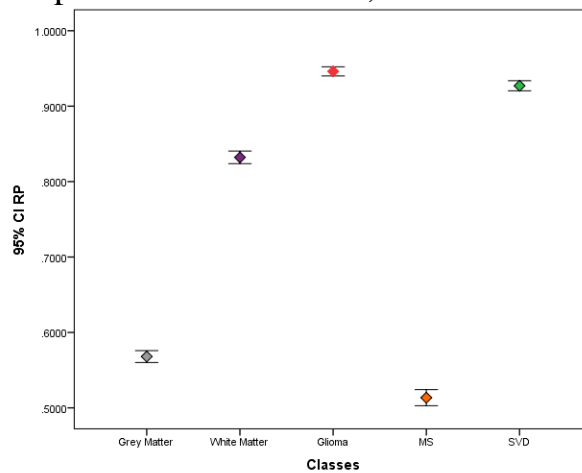


Fig (4-56): Error bar plot show the discriminate power of the RP textural feature distribution for the selected classes on T1+C MR Images for patients with Glioma, MS and SVD.

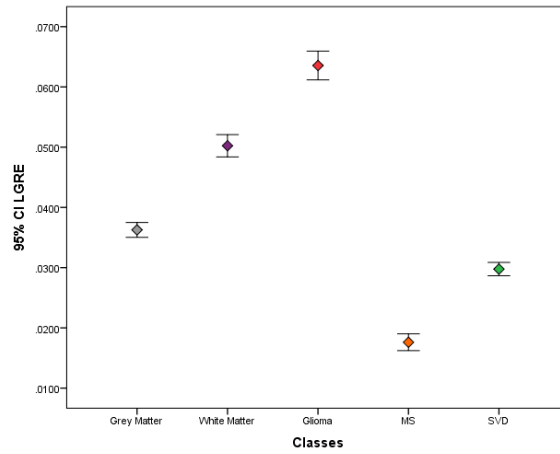


Fig (4-57): Error bar plot show the discriminate power of the LGRE textural feature distribution for the selected classes on T1+C MR Images for patients with Glioma, MS and SVD.

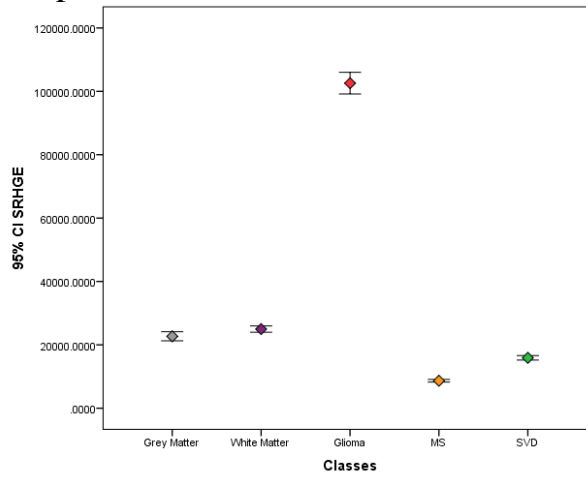


Fig (4-58): Error bar plot show the discriminate power of the SRHGE textural feature distribution for the selected classes on T1+C MR Images for patients with Glioma, MS and SVD.

Chapter five

Discussion, conclusion and recommendation

5.1. Discussion:

The main aim of this thesis is to characterize the white matter lesions (Glioma, Multiple Sclerosis [MS] and Small Vessels Disease [SVD]) on MR images (T1, T2, FLAIR and T1+C imaging sequences) using texture analysis (first order statistics and higher order statistics). In this study there is five classes; from each class a six first order statistical features (mean, variance, kurtosis, skewness, energy and entropy) and eleven higher order statistical features (SRE, LRE, GLN, RLN, RP, LGRE, HGRE, SRLGE, SRHGE, LRLGE and LRHGE) were extracted to classify the white matter lesions from normal tissues and from each other, using linear discriminate analysis. the result of classification indicated that using the first order and the higher order statistical features are : firstly for the Glioma it successfully differentiate it from the grey matter and white matter of the brain on T1, T2, T1+C and FLAIR images, similar to Qurat 2010, as there is no interference between the classes centers (blue squares), presented in Fig (4-2) to Fig (4-5); with classification accuracy using the first order textural features equal 99.0%, 96.9%, 94.8% and 92.2% on T2, T1(agreeing to Doaa, 2003),T1+C and FLAIR images respectively; and the sensitivity of detecting the Glioma in that order equal 98.2%, 95.6%, 83.8% and 83.1%. While when using the higher order statistical features the highest accuracy was on T1+C (corresponding to Tian et al 2018) then T2, FLAIR and lastly T1 images (=93.6%, 92.6%, 89.4% and 86.4% respectively); and sensitivity = 93.6%, 91.3%, 81.4% and 88.3% correspondingly; shown in table (4-1) to table (4-8).

Secondly in the MS patient images also effectively distinguish between the lesion plaques and the normal tissue in all imaging sequences as there is no interference between the classes centers (blue squares), presented in Fig (4-16) to Fig (4-19). with classification accuracy when using the first order textural features equal 93.2%, 92.8%, 92.0% and 87.6% on T1,T2,T1+C and FLAIR images respectively; and the sensitivity of detecting the MS plaques in that order equal 84.6%, 84.7%, 99.3% and 81.1%. While when using the higher order statistical features the highest accuracy was on T1, T1+C, FLAIR and lastly T2 images equal to 97.1%, 93.5%, 92.1% and 91.3% respectively; and sensitivity equal to 97.7%, 99.3%, 91.3% and 87.0% respectively; (agreeing to Jing 2008 and Loizou in 2014) ; presented in table(4-9) to table (4-16).

Also when using linear discriminate analysis in the classification of the features that extracted from the SVD patients images; it successfully differentiate the lesion from the normal brain tissues in all MR imaging sequences; as there is no interference between the classes centers (blue squares), presented on fig (4-32) to Fig (4-35). With accuracy equal to 97.2%, 94.8%, 91,9 % and 90.9% on T1, FLAIR, T1+C and T2 images respectively; and the sensitivity of detecting the SVD in that order equal 95.7%, 91.1%, 97.5% and 85.4% ; when using the first order features. While when using the higher order features the highest accuracy was on FLAIR, T1, T1+C and then T2 images equal to 96.3%, 94.7%, 93.5% and 85.2% respectively; and sensitivity equal to 94.6%, 91.2%, 81.1% and 74.4% respectively; presented in table (4-17) to table (4-24).

Moreover, a classification map was generate from the classified features for all lesions in all MR imaging sequences, shown in the appendices (appendix (A-1) to (A-12)). Also presented on fig (4-1), fig (4-15) and fig (4-31) for the imaging sequence that had the highest accuracy in each lesion.

From what listed above the result of discrimination of lesions in the T1+C imaging sequence has the highest sensitivity for detecting the lesions than the others imaging sequences (appears 4 times); so on this study it has been chosen to classify the lesions from each other and the result of classification using the first order and the higher order statistical features showed that all classes are very different from each other as the center of each class (blue square) is away from the other on T1+C images, presented on Fig (4-47); with classification accuracy using the first order textural features equal 87.2%; and the sensitivity of detecting the Glioma, MS and SVD equal 87.3%, 80.3%, 100% respectively, shown from table(4-25). While when using the higher order statistical features the accuracy was on T1+C equal 96.2%; and sensitivity equal 96.3%, 93.0% and 100% for the Glioma, MS and SVD correspondingly (agreeing to Theocharakis 2009 and Sarah 2017 but on FLAIR imaging sequence), as presented in table (4-25).

Regarding the T1 imaging sequence, for Glioma patients in part (A) from fig (4-6) to fig (4-14); the first order statistical features; the mean and the entropy (same as declared by Soni et al 2019), Textural features have successfully distinguished between the Glioma and the normal tissue; with the Glioma have the highest value and the grey matter having the lowest value. Also the skewness differentiates between the Glioma and the normal tissue, with the Glioma have the lowest value. Although the variance textural feature differentiates between the Glioma and the normal tissue, but there is interference between the grey matter and the white matter. However energy textural feature shows interference between the Glioma and the grey matter. While on the higher order statistics the features that successfully discriminate between the Glioma and the normal tissue were the SRE, LRE, GLN, RLN and RP textural features, with the Glioma having the highest SRE and GLN

values, and lowest LRE and RLN values from the normal tissues. While LGRE textural features also differentiate between the Glioma and the grey matter and the white matter, but the the Glioma shows a wide ranging.

Moreover concerning the T2 imaging sequence for Glioma patients in part (B) from fig (4-6) to fig (4-14); the first order statistical features; the mean, the variance and the entropy (same as declared by Soni et al 2019) textural features have successfully distinguish between the Glioma and the normal tissue specially the white matter (the Glioma have the highest value while the white matter have the lowest value); also the energy feature differentiates between the alioma and the normal tissue, with the Glioma having the lowest value than the normal tissues, while the kurtosis textural features shows interference between the Glioma and the white matter. Additionally on the higher order statistical features the SRE, LRE, GLN and RLN textural features successfully differentiate the Glioma from the normal tissues; with the Glioma having the highest value on SRE and GLN textural features and lowest LRE and RLN values; nevertheless there is interference between the grey matter and white matter values on SRE, LRE and RLN. However the RP textural feature shows interference between the grey matter and the Glioma.

On FLAIR imaging sequence for the Glioma patients, the first order statistical features; mean, variance, skewness, energy and the entropy (same as declared by Soni et al 2019), have been successfully differentiate between the Glioma and the white matter, with the Glioma have the highest mean value and entropy value, but there is interference between the Glioma and grey matter in the variance textural feature values. While for the higher order statistical features the SRE, GLN, HGRE and SRHGE highly discriminate the Glioma from the normal tissue, with the Glioma have the highest value in all of them; in addition

the LRE and RLN also differentiate the Glioma well, but it have the lowest value on them both. Presented on part (C) from fig (4-6) to fig (4-14). Furthermore on T1+C imaging sequence the first order statistical features; the mean and the entropy (same as declared by Soni et al 2019 and Xie et al 2018) textural features have successfully distinguish between the Glioma and the normal tissue; specially the white matter (the Glioma have the highest value while the white matter have the lowest value); also the energy textural feature differentiate between the Glioma and normal tissue, with it having the lowest value; while the variance textural feature, it differentiate the Glioma from the normal tissue, corresponding to Ditmer et al, 2018 and Skagon et al, 2016 ; but there is interference between the grey matter and the white matter. Furthermore concerning the higher order statistical features, the SRE, LRE, GLN, RLN, RP and LGRE successfully differentiate the Glioma from the normal tissue, with the Glioma having the highest value on SRE, GLN, RP and LGRE. But on the LRE, and RLN textural features having the lowest values than the normal tissues also there is interference between the white matter and the grey matter on SRE, LRE, and RLN textural features. Presented on part (D) from fig (4-6) to fig (4-14).

While regarding the T1 imaging sequence in MS patients, concerning the first order statistics; the mean, the variance, the energy and the entropy successfully differentiate the MS plaques from the normal tissue, with the MS plaques having the highest mean, energy and entropy values than the normal tissues, but having the lowest variance textural feature value with a wide range and also on this feature there is interference between the grey matter and the white matter. Moreover on the higher order statistics the; RP, LGRE, HGRE and LRLGE textural features effectively differentiate the MS plaques from the normal tissue, the RP shows the best discrimination with the MS having the lowest value and

the white matter having the highest RP value. While on the SRE, LRE, GLN and RLN textural features there is interference between the MS plaques and the white matter. Presented on part (A) from fig (4-20) to fig (4-30).

Furthermore on the T2 imaging sequence in MS patients; the first order statistics; mean, variance, kurtosis, energy and entropy textural features successfully differentiate the MS plaques from the normal tissue, with the MS having the highest mean and entropy values and the white matter having the lowest values (agreeing with Sarah 2016 in what concerning the mean and the entropy but regarding the energy feature energy there was interference between the MS and white matter ; the discrimination results on the this thesis have different sample size and different classes (on this thesis the classes are the lesion (MS), normal white matter and normal grey matter; while on Sarah 2017 the classes were the lesion (MS), normal appearance white matter, normal appearance grey matter and CSF)). Additionally on the higher order statistics the; SRE, LRE, GLN, RLN, RP, HGRE, SRHGE and LRHGE textural features successfully differentiate the MS plaques from the normal tissue, with the MS having the highest SRE, GLN, RP, HGRE, SRHGE and LRHGE values than the normal tissues, with the white matter having the lowest GLN, RP, HGRE, SRHGE and LRHGE values; however on the SRE, LRE and RLN textural features there is interference between the white matter and the grey matter. Presented on part (B) from fig (4-20) to fig (4-30).

While on FLAIR imaging sequence for the MS patients, the first order statistical features; mean, variance, kurtosis, skewness and entropy textural features have been successfully differentiate between the MS plaques and the white matter, with MS having the highest mean, variance and entropy values and the white matter having the lowest values

(agreeing with Sarah 2017), but in the kurtosis and the skewness; the MS have the lowest value and the white matter have the highest value. On the other hand the energy textural feature shows good differentiation for the grey matter, with it having the highest value, but there is interference between the white matter and the MS plaques. While regarding the higher order statistical features: the SRE, LRE, GLN, RLN, RP, LRGE, HGRE and SRHGE textural features successfully differentiate the MS plaques from the normal tissue, with the MS having the highest GLN, RP, LRGE, HGRE and SRHGE values and the white matter having the lowest values, while on the SRE textural feature there interference the grey matter and the white matter. Presented on part (C) from fig (4-20) to fig (4-30).

On T1+C imaging sequence for the MS patients, the first order statistical features; mean, variance, kurtosis, skewness, energy and the entropy have been successfully differentiate between the MS plaques and the normal tissues, with interference between the grey matter and the white matter values on kurtosis and energy textural features. Moreover regarding the higher order statistical features; the SRE, LRE, GLN, RLN, RP, SRLGE and LRHGE textural features effectively differentiate the MS plaques from the normal tissue; with the SRE, LRE, RLN and RP shows the best differentiation between the MS plaques and the white matter. Presented on part (D) from fig (4-20) to fig (4-30).

In addition on T1 imaging sequence in SVD patients; the first order statistical features; mean, variance, energy and the entropy successfully differentiate between the SVD and the normal tissues, but there interference between the grey matter and the white matter in variance and energy features values. However regarding the higher order statistics; GLN, RP, LGRE, HGRE, SRLGE, SRHGE, LRLGE and LRHGE textural features successfully differentiate the SVD from the

normal tissue; and best feature for the differentiation between the SVD and the white matter is RP feature, with the SVD having the lowest value and the white matter having the highest value. Presented on part (A) from fig (4-36) to fig (4-46). Furthermore on T2 imaging sequence in SVD patients; all the first order statistical features; mean, variance, kurtosis, skewness, energy and the entropy have successfully differentiate between the SVD and the normal tissues, also there is no interference between the three classes in all features; and the best features that differentiate between the SVD and the white matter are; mean, skewness and the entropy, with the SVD having the highest value and the white matter have the lowest value of mean and the entropy while their skewness values are opposite to that. Moreover regarding the higher order statistical features; the SRE, LRE, GLN, RLN, RP, HGRE, SRLGE, SRHGE and LRLGE textural features successfully differentiate the SVD from the normal tissue; and best features to differentiate the SVD from the white matter is GLN and the RP features, with the SVD having the highest value and the white matter have the lowest value. Presented on part (B) from fig (4-36) to fig (4-46).

Additionally on FLAIR imaging sequence in SVD patients; about the first order statistics; mean, variance, kurtosis, skewness, energy and the entropy have successfully discriminate the SVD from the normal tissue; with no interference between all classes in all features, and the best features that differentiate between the SVD and the white matter are; mean, variance, kurtosis, skewness and the entropy textural features. Furthermore regarding the higher order statistics; the SRE, LRE, GLN, RLN, RP, LRGE, HGRE, SRHGE and LRHGE textural features successfully differentiate between the three classes in general; and the SVD from the white matter in specific. Presented on part (C) from fig (4-36) to fig (4-46).

Furthermore on T1+C imaging sequence the first order statistical features; the mean, variance, skewness, energy and entropy textural features have successfully distinguish between the SVD and the normal tissue, with the energy feature the best discrimination result between the SVD and the white matter (the SVD have the lowest value while the white matter have the highest value); also here is no interference between the three classes in the previously listed features. In addition concerning the higher order statistical features, the SRE, LRE, GLN, RLN, RP, LGRE, HGRE, SRHGE, and LRLGE textural features successfully differentiate the SVD from the normal tissue, but there is interference between the grey matter and the white matter values in SRE, LRE, RLN, RP and LGRE textural features. Presented on part (D) from fig (4-36) to fig (4-46).

Finally concerning the discrimination results for all lesions in T1+C imaging sequence; the first order statistical features (mean, variance, energy and entropy) shows effective differentiation – no interference between all classes (Glioma, MS, SVD, grey matter and white matter), (corresponding to Sarah 2017 regarding the MS and the SVD in FLAIR images); with the Glioma having the highest values in all previously listed features and the MS plaques have the lowest value regarding the lesions. In addition for the higher order statistical features, the SRE, LRE, RLN, RP, LGRE and SRHGE features successfully discriminate between the five classes, while the GLN feature shows good differentiation between the three lesions, but there is interference between the grey matter and the white matter. In case of Glioma the GLN, LGRE and SRHGE features are the best for differentiate between it and the other lesions; while for the MS the best is the RP feature, and for the SVD the best features for distinguish it, are LRE and RLN. Presented from fig (4-48) to fig (4-58).

5.2. Conclusion:

In conclusion the white matter lesions can be diagnosed quantitatively from the normal tissues on MR images:

Firstly the Glioma:

When using the first order statistics by a*:

*sensitivity equal to **95.6%** on **T1** images using the following equations:

$$\text{Glioma} = (20.230 \times \text{mean}) + (.277 \times \text{variance}) + (-5.500 \times \text{skewness}) + (.206 \times \text{energy}) + (-2.321 \times \text{entropy}) - 275.570$$

$$\text{White matter} = (23.640 \times \text{mean}) + (-.103 \times \text{variance}) + (-5.337 \times \text{skewness}) + (.219 \times \text{energy}) + (-2.851 \times \text{entropy}) - 238.220$$

$$\text{Grey matter} = (21.471 \times \text{mean}) + (-.129 \times \text{variance}) + (-4.689 \times \text{skewness}) + (.192 \times \text{energy}) + (-2.605 \times \text{entropy}) - 189.823$$

*sensitivity equal to **98.2%** on **T2** images using the following equations:

$$\text{Glioma} = (19.977 \times \text{mean}) + (-.100 \times \text{variance}) + (1.830 \times \text{Kurtosis}) + (.053 \times \text{energy}) + (-2.363 \times \text{entropy}) - 217.467$$

$$\text{White matter} = (13.668 \times \text{mean}) + (-.053 \times \text{variance}) + (1.059 \times \text{Kurtosis}) + (.061 \times \text{energy}) + (-1.635 \times \text{entropy}) - 98.053$$

$$\text{Grey matter} = (17.800 \times \text{mean}) + (-.067 \times \text{variance}) + (1.781 \times \text{Kurtosis}) + (.053 \times \text{energy}) + (-2.123 \times \text{entropy}) - 163.923$$

*sensitivity equal to **83.1%** on **FLAIR** images using the following equations:

$$\text{Glioma} = (43.313 \times \text{mean}) + (.456 \times \text{variance}) + (-1.354 \times \text{skewness}) + (.209 \times \text{energy}) + (-5.206 \times \text{entropy}) - 449.781$$

$$\text{White matter} = (39.778 \times \text{mean}) + (.426 \times \text{variance}) + (-1.425 \times \text{skewness}) + (.165 \times \text{energy}) + (-4.830 \times \text{entropy}) - 351.069$$

$$\text{Grey matter} = (43.227 \times \text{mean}) + (.471 \times \text{variance}) + (-1.642 \times \text{skewness}) + (.201 \times \text{energy}) + (-5.227 \times \text{entropy}) - 427.022$$

*sensitivity equal to **83.8%** on **T1+C** images using the following equations:

$$\text{Glioma} = (33.284 \times \text{mean}) + (.047 \times \text{variance}) + (.265 \times \text{energy}) + (-3.955 \times \text{entropy}) - 360.222$$

$$\text{White matter} = (31.523 \times \text{mean}) + (-.013 \times \text{variance}) + (.259 \times \text{energy}) + (-3.796 \times \text{entropy}) - 288.834$$

$$\text{Grey matter} = (35.007 \times \text{mean}) + (-.010 \times \text{variance}) + (.298 \times \text{energy}) + (-4.202 \times \text{entropy}) - 364.053$$

When using the higher order statistics by a*:

*sensitivity equal to **88.3%** on **T1** images using the following equations:

$$\text{Glioma} = (91.169 \times \text{SRE}) + (8.573 \times \text{LRE}) + (.007 \times \text{GLN}) + (83.018 \times \text{RP}) + (-151.252 \times \text{LGRE}) - 108.927$$

$$\text{White matter} = (102.659 \times \text{SRE}) + (9.108 \times \text{LRE}) + (.004 \times \text{GLN}) + (85.814 \times \text{RP}) + (-273.059 \times \text{LGRE}) - 76.855$$

$$\text{Grey matter} = (102.199 \times SRE) + (9.358 \times LRE) + (.003 \times GLN) + (74.818 \times RP) + (-246.055 \times LGRE) - 67.418$$

*sensitivity equal to **91.3%** on **T2** images using the following equations:

$$\text{Glioma} = (3018.801 \times SRE) + (-735.729 \times LRE) + (.010 \times GLN) + (4323.954 \times RLN) + (125.574 \times RP) - 3355.977$$

$$\text{White matter} = (3010.589 \times SRE) + (-734.551 \times LRE) + (.006 \times GLN) + (4315.083 \times RLN) + (105.704 \times RP) - 3307.723$$

$$\text{Grey matter} = (3024.061 \times SRE) + (-735.840 \times LRE) + (.008 \times GLN) + (4325.909 \times RLN) + (126.052 \times RP) - 3347.503$$

*sensitivity equal to **81.4%** on **FLAIR** images using the following equations:

$$\text{Glioma} = (204.564 \times SRE) + (.008 \times GLN) + (102.857 \times RLN) + (71.911 \times RP) - 181.097$$

$$\text{White matter} = (208.547 \times SRE) + (.005 \times GLN) + (103.777 \times RLN) + (73.037 \times RP) - 172.733$$

$$\text{Grey matter} = (210.897 \times SRE) + (.007 \times GLN) + (104.680 \times RLN) + (83.014 \times RP) - 187.687$$

*sensitivity equal to **93.6%** on **T1+C** images using the following equations:

$$\text{Glioma} = (94.305 \times SRE) + (11.117 \times LRE) + (.009 \times GLN) + (79.843 \times RP) + (157.989 \times LGRE) + (-77.437 \times SRLGE) - 112.462$$

$$\text{White matter} = (98.729 \times SRE) + (10.535 \times LRE) + (.005 \times GLN) + (71.341 \times RP) + (-183.077 \times LGRE) + (-104.702 \times SRLGE) - 68.796$$

$$\text{Grey matter} = (99.810 \times SRE) + (10.712 \times LRE) + (.007 \times GLN) + (79.136 \times RP) + (-87.865 \times LGRE) + (-143.967 \times SRLGE) - 84.798$$

Secondly the MS:

When using the first order statistics by a*:

*sensitivity equal to **84.6%** on **T1** images using the following equations:

$$\text{MS} = (216.462 \times \text{mean}) + (5.340 \times \text{variance}) + (1.242 \times \text{Kurtosis}) + (-3.900 \times \text{skewness}) + (.318 \times \text{energy}) + (-29.012 \times \text{entropy}) - 1339.589$$

$$\text{White matter} = (225.128 \times \text{mean}) + (5.762 \times \text{variance}) + (1.681 \times \text{Kurtosis}) + (-4.625 \times \text{skewness}) + (.287 \times \text{energy}) + (-30.239 \times \text{entropy}) - 1412.320$$

$$\text{Grey matter} = (225.803 \times \text{mean}) + (5.541 \times \text{variance}) + (1.768 \times \text{Kurtosis}) + (-4.482 \times \text{skewness}) + (.267 \times \text{energy}) + (-30.401 \times \text{entropy}) - 1390.958$$

*sensitivity equal to **84.7%** on **T2** images using the following equations:

$$\text{MS} = (44.349 \times \text{mean}) + (.064 \times \text{variance}) + (-1.935 \times \text{Kurtosis}) + (-1.103 \times \text{skewness}) + (-.022 \times \text{energy}) + (-5.729 \times \text{entropy}) - 320.691$$

$$\text{White matter} = (37.698 \times \text{mean}) + (.109 \times \text{variance}) + (.233 \times \text{Kurtosis}) + (-1.113 \times \text{skewness}) + (-.001 \times \text{energy}) + (-4.912 \times \text{entropy}) - 221.127$$

$$\text{Grey matter} = (44.334 \times \text{mean}) + (.113 \times \text{variance}) + (.413 \times \text{Kurtosis}) + (-1.267 \times \text{skewness}) + (-.030 \times \text{energy}) + (-5.756 \times \text{entropy}) - 307.783$$

*sensitivity equal to **81.1%** on **FLAIR** images using the following equations:

$$MS = (77.591 \times \text{mean}) + (.777 \times \text{variance}) + (-.062 \times \text{Kurtosis}) + (-3.790 \times \text{skewness}) + (.196 \times \text{energy}) + (-9.544 \times \text{entropy}) - 718.437$$

$$\text{White matter} = (73.887 \times \text{mean}) + (.561 \times \text{variance}) + (.358 \times \text{Kurtosis}) + (-2.671 \times \text{skewness}) + (.153 \times \text{energy}) + (-9.136 \times \text{entropy}) - 620.747$$

$$\text{Grey matter} = (78.003 \times \text{mean}) + (.649 \times \text{variance}) + (.287 \times \text{Kurtosis}) + (-3.256 \times \text{skewness}) + (.204 \times \text{energy}) + (-9.621 \times \text{entropy}) - 708.782$$

*sensitivity equal to **99.3%** on **T1+C** images using the following equations:

$$MS = (411.974 \times \text{mean}) + (2.785 \times \text{Kurtosis}) + (-4.786 \times \text{skewness}) + (.123 \times \text{energy}) + (-56.858 \times \text{entropy}) - 2269.702$$

$$\text{White matter} = (398.743 \times \text{mean}) + (1.857 \times \text{Kurtosis}) + (-5.591 \times \text{skewness}) + (.180 \times \text{energy}) + (-54.966 \times \text{entropy}) - 2159.827$$

$$\text{Grey matter} = (417.190 \times \text{mean}) + (1.298 \times \text{Kurtosis}) + (-6.235 \times \text{skewness}) + (.174 \times \text{energy}) + (-57.655 \times \text{entropy}) - 2306.445$$

When using the higher order statistics by a*:

*sensitivity equal to **97.7%** on **T1** images using the following equations:

$$MS = (2870.460 \times \text{SRE}) + (-749.270 \times \text{LRE}) + (.028 \times \text{GLN}) + (4310.889 \times \text{RLN}) + (-11.688 \times \text{RP}) + (587.433 \times \text{LGRE}) + (-15639.512 \times \text{SRLGE}) + (.003 \times \text{SRHGE}) + (-145.420 \times \text{LRLGE}) - 3275.347$$

$$\text{White matter} = (2886.286 \times \text{SRE}) + (-744.483 \times \text{LRE}) + (.023 \times \text{GLN}) + (4291.633 \times \text{RLN}) + (16.113 \times \text{RP}) + (511.892 \times \text{LGRE}) + (-17429.484 \times \text{SRLGE}) + (.002 \times \text{SRHGE}) + (-492.588 \times \text{LRLGE}) - 3257.169$$

$$\text{Grey matter} = (2885.392 \times \text{SRE}) + (-739.134 \times \text{LRE}) + (.019 \times \text{GLN}) + (4264.104 \times \text{RLN}) + (22.229 \times \text{RP}) + (455.895 \times \text{LGRE}) + (-16915.883 \times \text{SRLGE}) + (.002 \times \text{SRHGE}) + (-367.678 \times \text{LRLGE}) - 3216.130$$

*sensitivity equal to **87.0%** on **T2** images using the following equations:

$$MS = (102.304 \times \text{SRE}) + (11.084 \times \text{LRE}) + (.024 \times \text{GLN}) + (91.493 \times \text{RP}) + (-.001 \times \text{SRHGE}) - 116.777$$

$$\text{White matter} = (100.290 \times \text{SRE}) + (10.729 \times \text{LRE}) + (.014 \times \text{GLN}) + (66.201 \times \text{RP}) + (-.001 \times \text{SRHGE}) - 73.049$$

$$\text{Grey matter} = (102.700 \times \text{SRE}) + (11.070 \times \text{LRE}) + (.019 \times \text{GLN}) + (82.918 \times \text{RP}) + (-.001 \times \text{SRHGE}) - 95.977$$

*sensitivity equal to **91.3%** on **FLAIR** images using the following equations:

$$MS = (2649.221 \times \text{SRE}) + (-647.170 \times \text{LRE}) + (.016 \times \text{GLN}) + (3787.139 \times \text{RLN}) + (191.383 \times \text{RP}) + (-735.568 \times \text{LGRE}) + (.000 \times \text{SRHGE}) - 2949.645$$

$$\text{White matter} = (2673.342 \times \text{SRE}) + (-648.698 \times \text{LRE}) + (.010 \times \text{GLN}) + (3798.084 \times \text{RLN}) + (169.960 \times \text{RP}) + (-992.612 \times \text{LGRE}) + (-.001 \times \text{SRHGE}) - 2928.918$$

$$\text{Grey matter} = (2668.861 \times \text{SRE}) + (-648.500 \times \text{LRE}) + (.014 \times \text{GLN}) + (3797.842 \times \text{RLN}) + (183.531 \times \text{RP}) + (-893.456 \times \text{LGRE}) + (-.001 \times \text{SRHGE}) - 2950.125$$

*sensitivity equal to **99.3%** on **T1+C** images using the following equations:

$$MS = (103.588 \times SRE) + (10.786 \times LRE) + (.010 \times GLN) + (98.778 \times RP) + (-448.397 \times LGRE) + (-292.812 \times SRLGE) - 73.765$$

$$White\ matter = (92.237 \times SRE) + (10.594 \times LRE) + (.012 \times GLN) + (123.059 \times RP) + (-493.553 \times LGRE) + (-397.402 \times SRLGE) - 83.017$$

$$Grey\ matter = (83.550 \times SRE) + (10.286 \times LRE) + (.015 \times GLN) + (118.782 \times RP) + (-390.567 \times LGRE) + (253.881 \times SRLGE) - 91.288$$

Finally the SVD:

When using the higher order statistics by a*:

*sensitivity equal to **95.7%** on **T1** images using the following equations:

$$SVD = (120.438 \times mean) + (3.317 \times variance) + (3.974 \times Kurtosis) + (.158 \times energy) + (-15.384 \times entropy) - 930.150$$

$$White\ matter = (123.661 \times mean) + (3.297 \times variance) + (3.611 \times Kurtosis) + (.139 \times energy) + (-15.868 \times entropy) - 937.862$$

Grey matter =

$$(118.223 \times mean) + (3.048 \times variance) + (3.054 \times Kurtosis) + (.126 \times energy) + (-15.217 \times entropy) - 838.951$$

*sensitivity equal to **85.4%** on **T2** images using the following equations:

$$SVD = (62.645 \times mean) + (.376 \times variance) + (7.156 \times Kurtosis) + (-.970 \times skewness) + (-.049 \times energy) + (-8.343 \times entropy) - 387.797$$

$$White\ matter = (56.779 \times mean) + (.376 \times variance) + (7.181 \times Kurtosis) + (-.675 \times skewness) + (-.048 \times energy) + (-7.589 \times entropy) - 310.561$$

$$Grey\ matter = (65.258 \times mean) + (.422 \times variance) + (9.233 \times Kurtosis) + (-.779 \times skewness) + (-.086 \times energy) + (-8.702 \times entropy) - 412.208$$

*sensitivity equal to **91.1%** on **FLAIR** images using the following equations:

$$SVD = (81.718 \times mean) + (.546 \times variance) + (-1.323 \times Kurtosis) + (-1.530 \times skewness) + (.207 \times energy) + (-10.027 \times entropy) - 760.743$$

$$White\ matter = (77.951 \times mean) + (.347 \times variance) + (-.805 \times Kurtosis) + (-1.155 \times skewness) + (.155 \times energy) + (-9.642 \times entropy) - 643.448$$

$$Grey\ matter = (83.355 \times mean) + (.427 \times variance) + (-1.081 \times Kurtosis) + (-1.414 \times skewness) + (.198 \times energy) + (-10.277 \times entropy) - 755.374$$

*sensitivity equal to **97.5%** on **T1+C** images using the following equations:

$$SVD = (110.315 \times mean) + (.724 \times variance) + (.384 \times Kurtosis) + (-3.272 \times skewness) + (-.200 \times energy) + (-13.895 \times entropy) - 866.256$$

$$White\ matter = (104.717 \times mean) + (.679 \times variance) + (.346 \times Kurtosis) + (-2.901 \times skewness) + (-.146 \times energy) + (-13.192 \times entropy) - 784.611$$

$$Grey\ matter = (111.955 \times mean) + (.783 \times variance) + (.334 \times Kurtosis) + (-3.292 \times skewness) + (-.152 \times energy) + (-14.070 \times entropy) - 913.428$$

When using the higher order statistics by a*:

*sensitivity equal to **91.2%** on **T1** images using the following equations:

$$SVD = (89.227 \times SRE) + (19.454 \times LRE) + (.025 \times GLN) + (155.459 \times RP) + (-887.325 \times SRLGE) + (.000 \times SRHGE) + (-3605.454 \times LRLGE) - 121.426$$

$$White\ matter = (111.127 \times SRE) + (20.854 \times LRE) + (.021 \times GLN) + (173.747 \times RP) + (-2900.165 \times SRLGE) + (-.001 \times SRHGE) + (-3818.665 \times LRLGE) - 124.415$$

$$Grey\ matter = (119.578 \times SRE) + (19.624 \times LRE) + (.017 \times GLN) + (162.475 \times RP) + (-3142.358 \times SRLGE) + (-.001 \times SRHGE) + (-3250.814 \times LRLGE) - 110.234$$

*sensitivity equal to **74.4%** on **T2** images using the following equations:

$$SVD = (111.437 \times SRE) + (16.370 \times LRE) + (.018 \times GLN) + (98.282 \times RP) + (-1081.461 \times SRLGE) + (-.001 \times SRHGE) + (-978.342 \times LRLGE) - 105.154$$

$$White\ matter = (106.403 \times SRE) + (14.791 \times LRE) + (.011 \times GLN) + (79.436 \times RP) + (-586.871 \times SRLGE) + (-.001 \times SRHGE) + (-769.059 \times LRLGE) - 75.779$$

$$Grey\ matter = (117.861 \times SRE) + (16.393 \times LRE) + (.015 \times GLN) + (101.124 \times RP) + (-2188.334 \times SRLGE) + (-.001 \times SRHGE) + (-994.345 \times LRLGE) - 101.296$$

*sensitivity equal to **94.6%** on **FLAIR** images using the following equations:

$$SVD = (246.153 \times SRE) + (.015 \times GLN) + (119.320 \times RLN) + (128.474 \times RP) + (-377.513 \times LGRE) + (.000 \times SRHGE) - 241.388$$

$$White\ matter = (271.839 \times SRE) + (.009 \times GLN) + (123.676 \times RLN) + (133.602 \times RP) + (-717.558 \times LGRE) + (-.001 \times SRHGE) - 216.688$$

$$Grey\ matter = (261.982 \times SRE) + (.012 \times GLN) + (122.237 \times RLN) + (136.503 \times RP) + (-571.058 \times LGRE) + (-.001 \times SRHGE) - 228.981$$

*sensitivity equal to **81.1%** on **T1+C** images using the following equations:

$$SVD = (2732.658 \times SRE) + (-681.046 \times LRE) + (.018 \times GLN) + (3954.977 \times RLN) + (60.110 \times RP) + (68.620 \times LGRE) + (-6899.477 \times SRLGE) + (-1105.283 \times LRLGE) - 3007.824$$

$$White\ matter = (2742.335 \times SRE) + (-685.688 \times LRE) + (.023 \times GLN) + (3973.990 \times RLN) + (72.061 \times RP) + (-74.975 \times LGRE) + (-4923.496 \times SRLGE) + (-851.074 \times LRLGE) - 3049.070$$

$$Grey\ matter = (2756.913 \times SRE) + (-681.830 \times LRE) + (.017 \times GLN) + (3956.939 \times RLN) + (83.682 \times RP) + (-168.006 \times LGRE) + (-4957.869 \times SRLGE) + (-766.020 \times LRLGE) - 3025.414$$

5.3. Recommendation:

After conduction of this thesis the researcher recommended that:

- Large sample can be used to have better overall accuracy using representative data set.
- More specialized researches should be done e.g: In case of glioma the classes can be the differentiation between its grades or the parts of the tumor itself and the surrounding white matter. While on multiple sclerosis the differentiation could be between the lesion plaques and the normal appearance white matter.
- Other type of diseases and feature can use or comparison between diseases have the same radiographic appearance.
- IDL program should be adopted by the radiology department to deal with the challenging cases and to have an objective second opinion.
- This study consider as starting point for continues researches in this subject are highly recommended.

References:

- Andreas Adam, Adrian K. Dixon, Jonathan H. Gillard, Cornelia M. 2015. Schaefer Prokop, Grainger & Allison's Diagnostic Radiology. 6th Edition, New York Oxford, Churchill Livingstone Elsevier.
- Bontrager .Kenneth L, Lampignano.John P. 2014.Textbook Of Radiographic Positioning and Related Anatomy. 8th Edition. China: Mosby Elsevier Inc .
- Catherine Westbrook. 2008. Handbook of MRI Technique. 3rd Edition. USA, Wiley-Blackwell, Sheridan Books, Inc.
- Catherine Westbrook. John Talbot, 2019. MRI in Practice, 5th Edition, Wiley Blackwell.
- Chapman .Stephen, Nakielny. Richard. 2003. Aids to Radiological Differential Diagnosis . Fourth Edition. London: British Library.
- Ditmer A, Zhang B, Shujaat T, Pavlina A, Luibrand N, Gaskill-Shipley M, Vagal A. 2018. Diagnostic accuracy of MRI texture analysis for grading gliomas. *Journal of Neuro-oncology*;140(3):583-9.
- ELHASSEN, Sarah Suliman Mohammed, et al. 2017. Characterization of Multiple Sclerosis on the Brain Magnetic Resonance Images Using Texture Analysis. Sudan University of Science and Technology.
- Evert J. Blink . MRI Physics. November, 2004:support@mri-physics.com
- Forbes K . 2017. MRI brain white matter change: spectrum of change – how can we grade., *J R Coll Physicians Edinb*; 47: 271–5
- Haralick, R. M. 1979. Statistical and structural approaches to texture. *Proceedings on the IEEE* (67) 5: 786-803.
- Johnston, B., Atkins, M. S., Mackiewich, B., & Anderson, M. 1996. Segmentation of multiple sclerosis lesions in intensity corrected multispectral MRI. *IEEE Transactions on Medical Imaging*, 15(2), 154-169.

- Kassner.A, Thornhill .R.E. 2010. Texture Analysis: A Review of Neurologic MR Imaging Applications. *AJNR Am J Neuroradiol*; 31:809–816
- Kelley L.L., Petersen C.M., 2007. *Sectional Anatomy for imaging professionals*, Second Edition, United States of America, Mosby-Elsevier Inc.
- Kornienko, Valery N.; Pronin, Igor Nicolaevich. 2008. *Diagnostic neuroradiology*. Springer Science & Business Media.
- Li Q, Yang Y, Reis C, Tao T, Li W, Li X, Zhang JH. 2018. Cerebral small vessel disease. *Cell transplantation* ;27(12):1711-22.
- Mahmoud-Ghoneim, Doaa., Toussaint, G., Constans, J. M., & Jacques, D. 2003. Three dimensional texture analysis in MRI: a preliminary evaluation in gliomas. *Magnetic resonance imaging*, 21(9), 983-987.
- Materka, M. Strzelecki, 1998. *Texture Analysis Methods – A Review*, Technical University of Lodz, Institute of Electronics, COST B11 report, Brussels Stefanowskiego; 18: 90-924
- Michoux .N, Guillet. A, Rommel. D,Mazzamuto. G, Sindic .C, Duprez. T . 2015. TextureAnalysis of T2-Weighted MR Images to Assess Acute Inflammation in Brain MS Lesions. *PLoS ONE* ;10: 1-13: e0145497. doi:10.1371/journal.pone.0145497
- Nicolae.S,Robert.Y,RobertV.Jones,IrenH.S,Laura.O, James G. S, 2016. White Matter Diseases with Radiologic-Pathologic Correlation, *RadioGraphics*; 36:1426–1447
- Qurat-Ul-Ain, G. L., Kazmi, S. B., Jaffar, M. A., & Mirza, A. M. 2010. Classification and segmentation of brain tumor using texture analysis. *Recent advances in artificial intelligence, knowledge engineering and data bases*, 147-155.
- Ronald L. Eisenberg, Nancy M. Johnson. 2016. *Comprehensive Radiographic pathology*. 6th edition. China. Mosby, Inc. page 287 - 333

Sarah Suliman Mohammed, et. al. 2021. "Characterization of Glioma on Brain Magnetic Resonance Images Using Texture Analysis." IOSR Journal of Dental and Medical Sciences (IOSR-JDMS), 20(03), pp. 30-41.

Sarah Suliman Mohammed, et. al. 2021. "Characterization of White Matter Lesions on Brain Magnetic Resonance Images Using Texture Analysis ." IOSR Journal of Dental and Medical Sciences (IOSR-JDMS), 20(03), pp. 57-64.

Skogen K, Schulz A, Dormagen JB, Ganeshan B, Helseth E, Server A. 2016. Diagnostic performance of texture analysis on MRI in grading cerebral gliomas. *European journal of radiology*. 1;85(4):824-9.

Soni N, Priya S, Bathla G. 2019. Texture analysis in cerebral gliomas: a review of the literature. *American Journal of Neuroradiology*; Jun 1;40(6).

Stephanie Ryan, Michelle McNicholas, Stephen Eustace. 2011. *Anatomy for Diagnostic Imaging*, 3rd edition , New York Oxford, Saunders Elsevier.

Theocharakis, P., Glotsos, D., Kalatzis, I., Kostopoulos, S., Georgiadis, P., Sifaki, K., ... & Nikiforidis, G. 2009. Pattern recognition system for the discrimination of multiple sclerosis from cerebral microangiopathy lesions based on texture analysis of magnetic resonance images. *Magnetic resonance imaging*, 27(3), 417-422.

Tian Q, Yan LF, Zhang X, Zhang X, Hu YC, Han Y, Liu ZC, Nan HY, Sun Q, Sun YZ, Yang Y. 2018. Radiomics strategy for glioma grading using texture features from multiparametric MRI. *Journal of Magnetic Resonance Imaging*; 48(6):1518-28.

Valdés Hernández, Maria. D. C., González-Castro, V., Chappell, F. M., Sakka, E., Makin, S., Armitage, P. A., & Wardlaw, J. M. 2017.

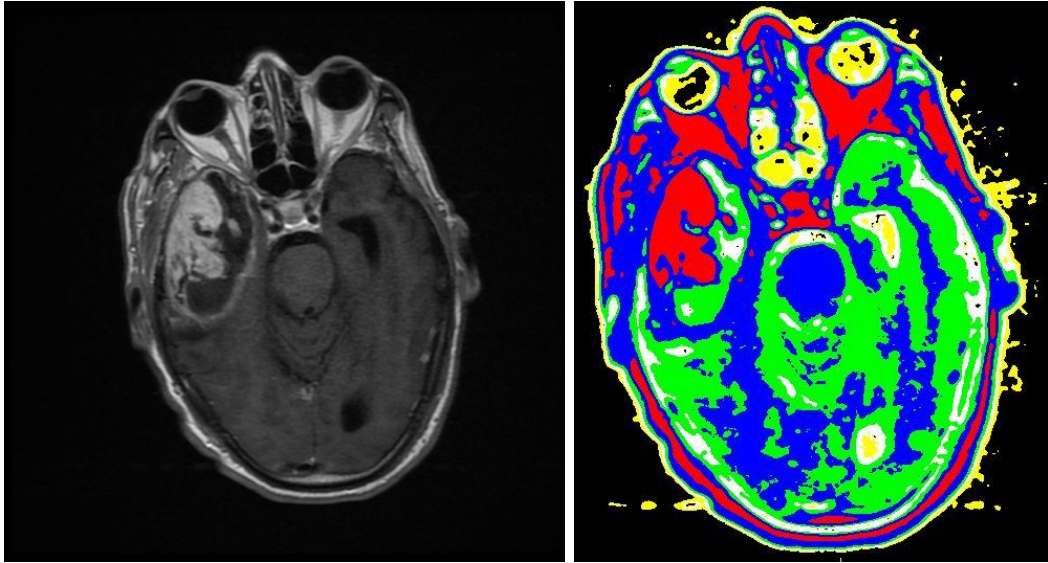
application of Texture analysis to study small Vessel Disease and Blood–Brain Barrier integrity. *Frontiers in neurology*, 8, 327.

Xie T, Chen X, Fang J, Kang H, Xue W, Tong H, Cao P, Wang S, Yang Y, Zhang W. 2018. Textural features of dynamic contrast-enhanced MRI derived model-free and model-based parameter maps in glioma grading. *Journal of Magnetic Resonance Imaging*;47(4):1099-1111.

Zhang, J., Tong, L., Wang, L., & Li, N. 2008. Texture analysis of multiple sclerosis: a comparative study. *Magnetic resonance imaging*, 26(8), 1160-1166.

Zhang, J., Tong, L., Wang, L., & Li, N. 2008. Texture analysis of multiple sclerosis: a comparative study. *Magnetic resonance imaging*, 26(8), 1160-1166.

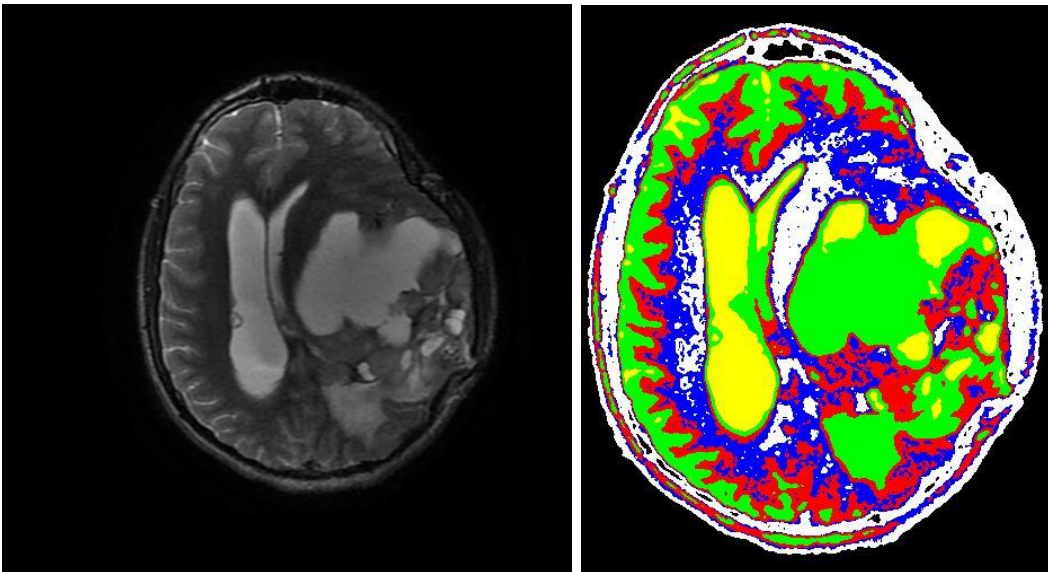
Appendices
Appendix (A); the color map



(a)

(b)

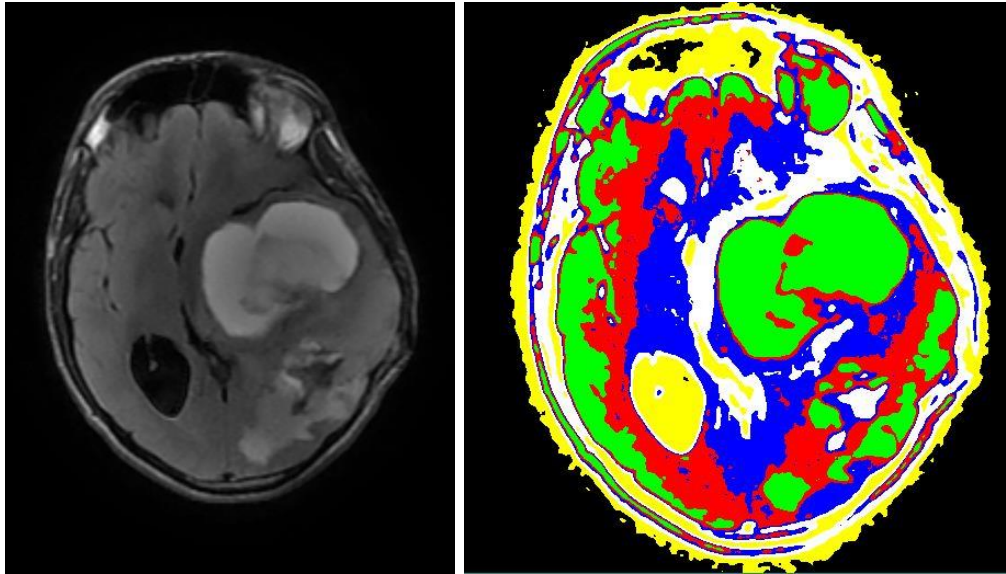
Appendix (A-1): (a) T1 images, (b) color map; for patient with Glioma



(a)

(b)

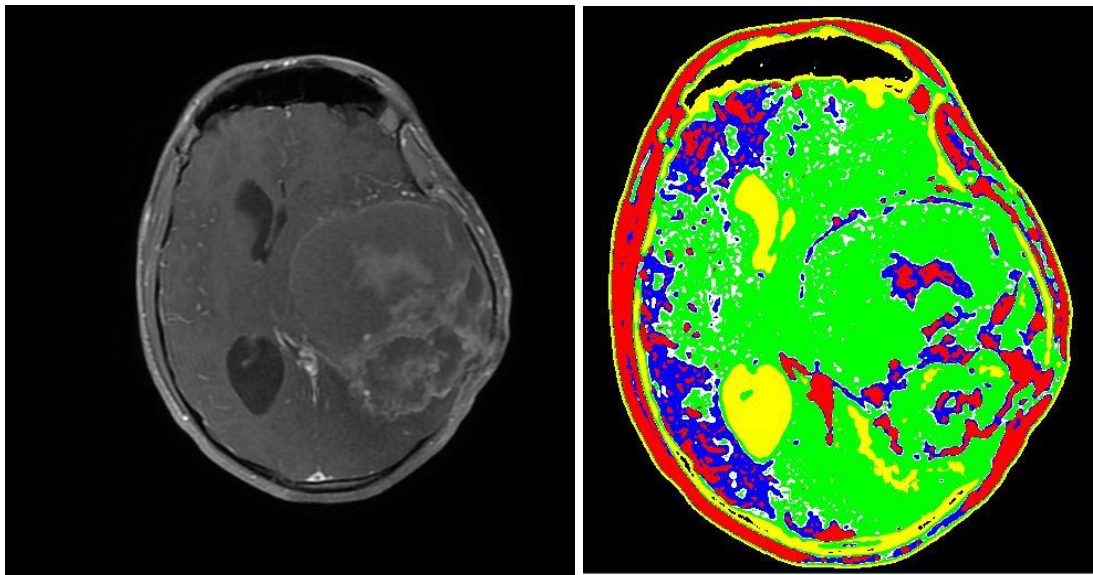
Appendix (A-2): (a) T2 images, (b) color map; for patient with Glioma



(a)

(b)

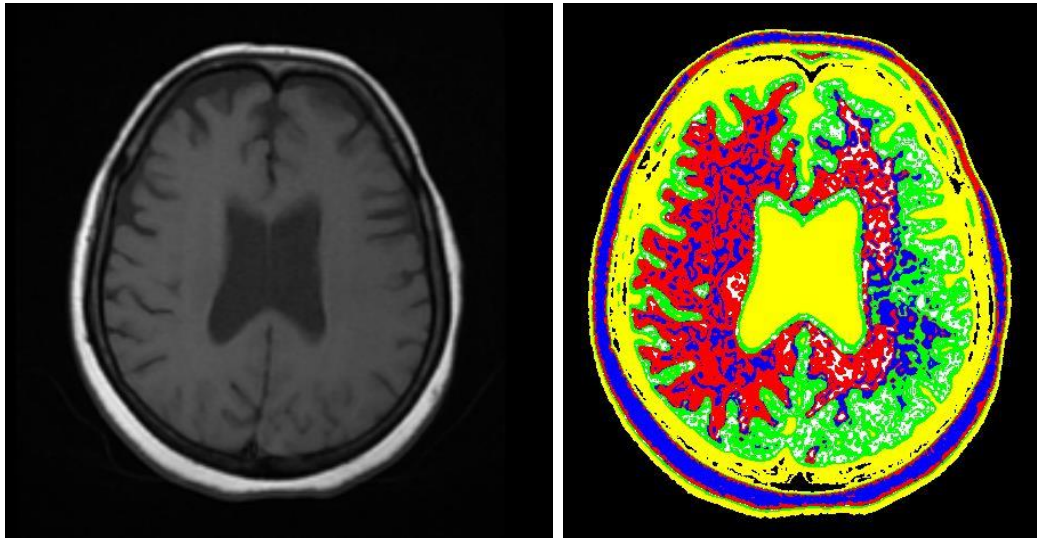
Appendix (A-3): (a) FLAIR images, (b) color map; for patient with Glioma



(a)

(b)

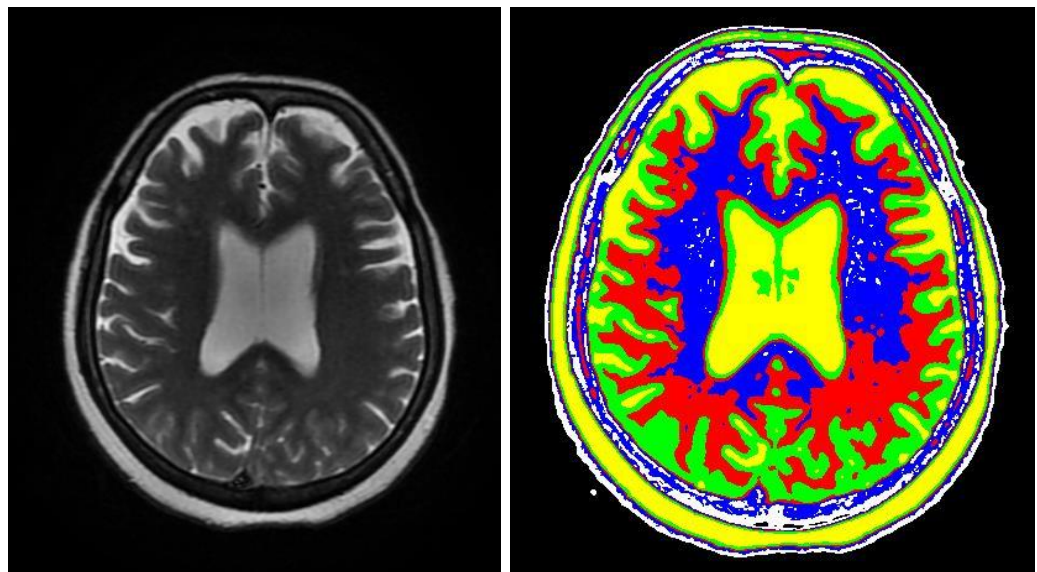
Appendix (A-4): (a) T1+C images, (b) color map; for patient with Glioma



(a)

(b)

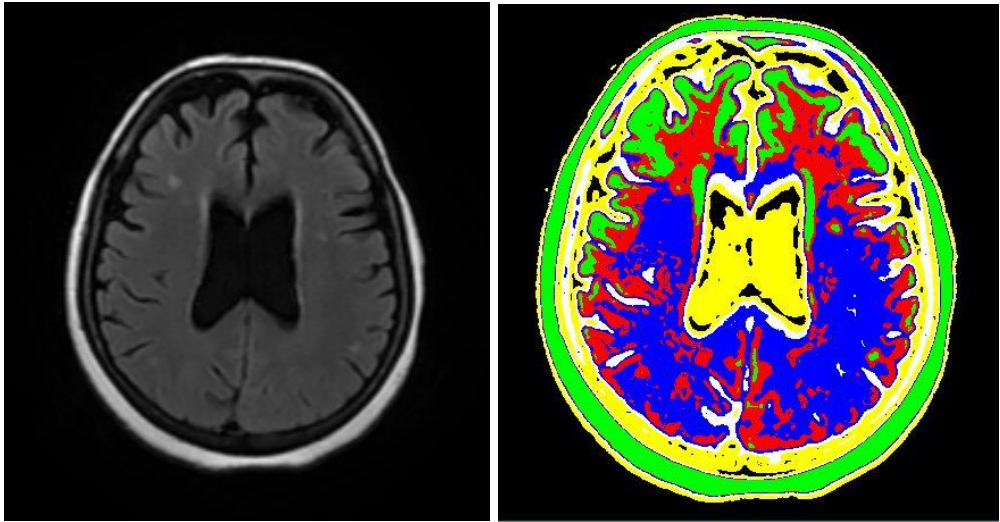
Appendix (A-5): (a) T1 images, (b) color map; for patient with MS



(a)

(b)

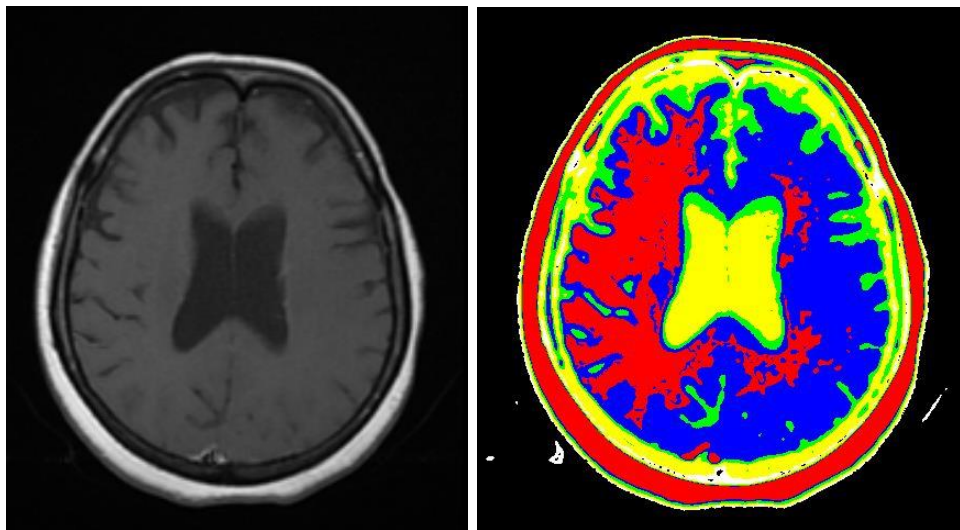
Appendix (A-6): (a) T2 images, (b) color map; for patient with MS



(a)

(b)

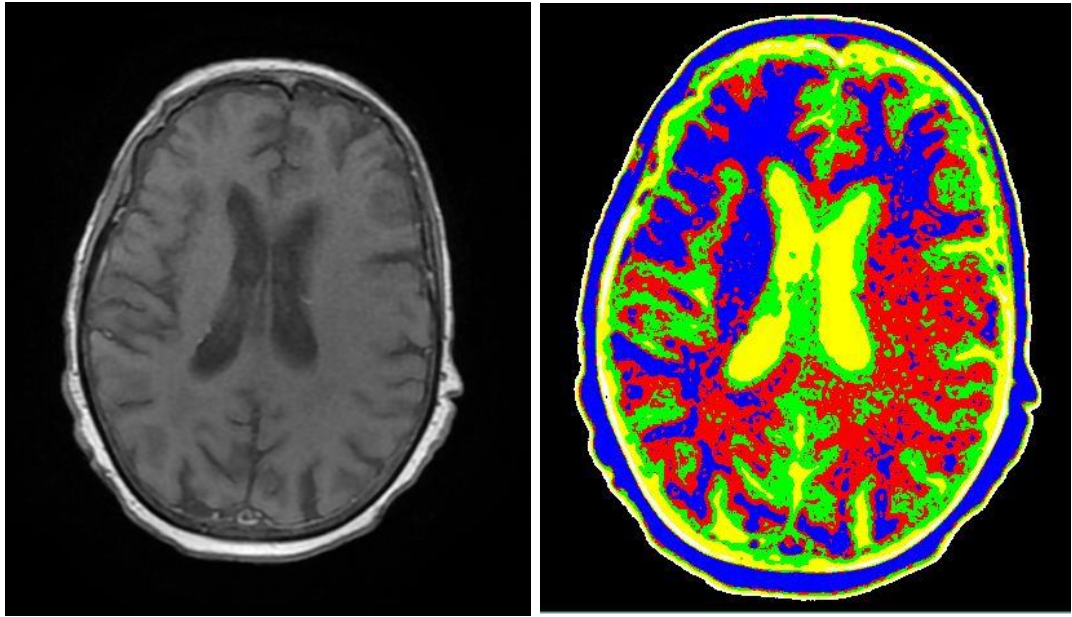
Appendix (A-7): (a) FLAIR images, (b) color map; for patient with MS



(a)

(b)

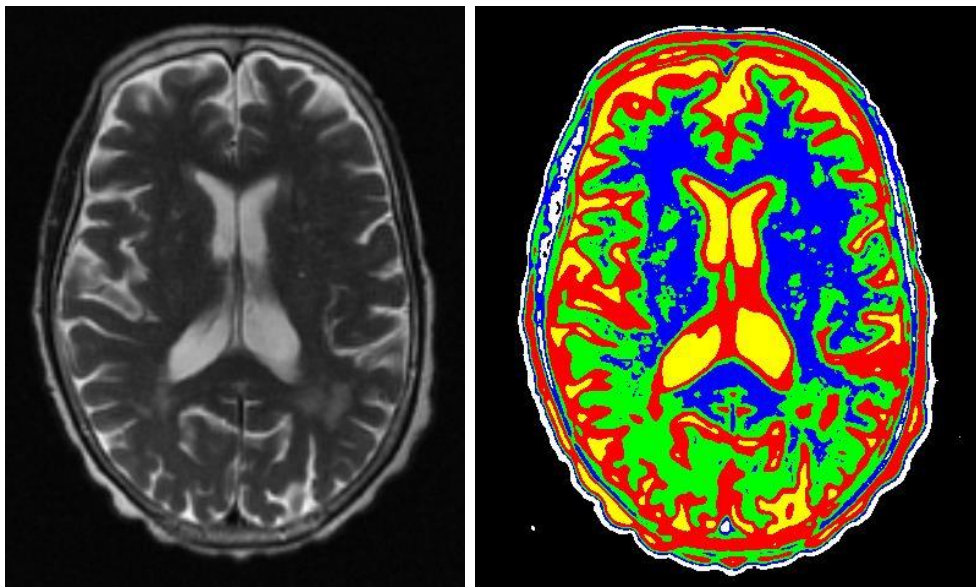
Appendix (A-8): (a) T1+C images, (b) color map; for patient with MS



(a)

(b)

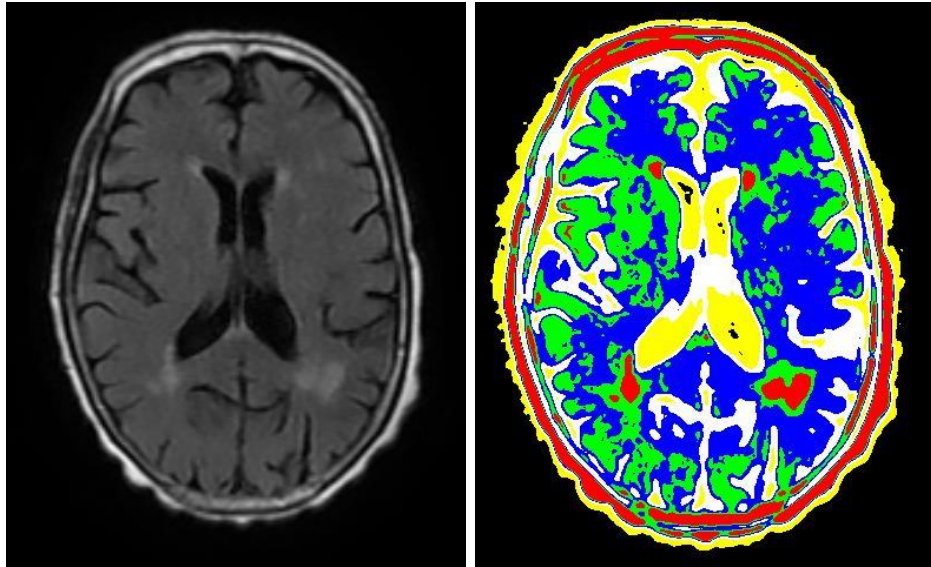
Appendix (A-9): (a) T1 images, (b) color map; for patient with SVD



(a)

(b)

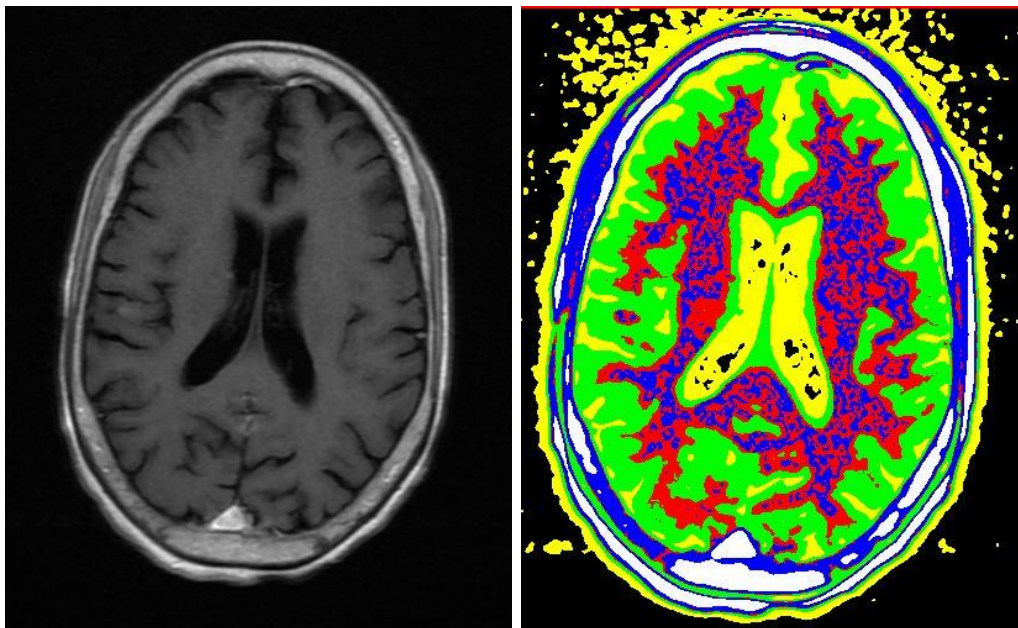
Appendix (A-10): (a) T2 images, (b) color map; for patient with SVD



(a)

(b)

Appendix (A-11): (a) FLAIR images, (b) color map; for patient with SVD



(a)

(b)

Appendix (A-12): (a) T1+C images for patient wit, (b) color map; for patient with SVD

Appendix (B) ethical approval process



وزارة الصحة - ولاية الخرطوم
الإدارة العامة للإستراتيجية والمعلومات
ادارة الابتكار والتطوير والبحث العلمي



التاريخ: 28/ 07/ 2019 م إقرار بالالتزام بتوجيهات لجنة البحوث الاخلاقية بوزارة الصحة ولاية الخرطوم

أقر انا الباحث ياسر محمد الحسن جامعة السودان للعلوم والتكنولوجيا - الخرطوم بالالتزام بتوصيات لجنة البحوث الاخلاقية بوزارة الصحة ولاية الخرطوم الآتية:-

- 1- عدم اجراء البحث مع الكوادر الصحية اثناء فترة العمل
- 2- مراعاة كافة حقوق المبحوثين المتفق عليها مع اللجنة
- 3- اخذ عينة من المبحوثين لغرض البحث
- 4- اخذ العينات الموجودة اصلا بالمعمل
- 5- ابلاغ المبحوثين بنتائج فحوصاتهم حالاً
- 6- سيتم جمع البيانات من الملفات
- 7- تسليم الوزارة نسخة من ملخص وتوصيات تقرير البحث عند الانتهاء منه
- 8- ارسال تقرير متابعة لجمع بيانات البحث كل اسبوعين للجنة عبر الايميل
- 9- الموافقة على تنفيذ البحث سارية حتى عام من تاريخه

* الفترة المتوقعة لتسليم التقرير للمؤسسة العلمية:- 20/10-2020

* الفترة المتوقعة لتسليم ملخص وتوصيات تقرير للوزارة:- 30/11-2020

* مدة جمع البيانات :- مستوفى

* مكان جمع البيانات :- مستوفى بالخرطوم

في حالة عدم التزام الباحث بما تم الاتفاق عليه يتم:-

- 1- مساهلة الباحث وفقاً لقانون البحوث الاتحادي
- 2- يحرم الباحث من حق اجراء بحث في المؤسسات التابعة للوزارة.
- 3- يحرم الباحث من اعطاء الموافقة العلمية والاخلاقية من ادارة البحوث بوزارة الصحة ولاية الخرطوم لنشر تقريره.

اسم المشرف :- د. روى محمد الفاضل جاراين

رقم هاتفه:- 0990080859

توقيع الباحث: ياسر محمد الحسن

رقم هاتفه:- 0919101599

ibtikar.Kmoh@gmial . com

توقيع السيد/ مدير ادارة الابتكار والتطوير والبحث العلمي
د. منى فتح الرحمن عمر

رويا ولاية: نحو عاصمة وطنية آمنة متحضرة

رويا ولاية: نحو عاصمة وطنية آمنة متحضرة

Appendix (B-1): the commitment that signed by the researcher



2.6. Ethical consideration:

Ethical approval from Sudan university of science and technology. Khartoum state ministry of health research department and from hospitals where no patient identification data or individual patient detail is published.

Research purpose and objectives will be explained to participant in clear simple words

Participant has right to voluntary informed consent

Participant has the right to withdraw at any time without any deprivation

Participant has the right to no harm(privacy and confidentiality by using coded questionnaire)

Participant has the right to benefit from the researcher knowledge and skills

The data will be collected from the PACS and radiology department in their rest time without any interruption to their work

Appendix (B-2) : Ethical consideration in English language

استمارة موافقة

انا الباحثة ساره سليمان محمد الحسن من جامعة السودان للعلوم والتكنولوجيا كلية الدراسات العليا. اقوم ببحث عن توصيف إصابات النسيج الأبيض في صور الرنين المغناطيسي للمخ باستخدام التحليل الملمسي قد تم اختياركم للمشاركة في هذا البحث ومعكم عدد اخر من المستشفيات. نتوقع مشاركتكم انتم و الآخرين لنحصل على نتائج تفيد الباحث و المجتمع. خلال هذه الدراسة سأقوم بأخذ صور لي أمراض معينة تم تحديدها في خطة البحث وإجراء تحليل باستخدام برنامج في الحاسوب عليها

الإجراء الذي اقوم به خالي من المخاطر على المشاركين

ونحن نأمل في مشاركتكم معنا في هذا البحث و نؤكد لك على سرية المعلومات الخاصة بكم . وأنه لن يطلع عليها إلا الباحث المعني ولجنة أخلاقيات البحوث .

كما نؤكد إمكانية الانسحاب من البحث في اي وقت نشاء ودون ابداء توضيح لأسباب الانسحاب و يتم ذلك بالتوقيع على طلب الانسحاب ولن يؤثر ذلك أيضا على حقك في الاستفادة من البحث .

اذا كان لديك اي سؤال او إستفسار يخص البحث او حقوقك كمشارك أثناء تنفيذ البحث يمكنك الاتصال علي

0919101599



Appendix (B-3) : Ethical consideration in Arabic language

وارز
No
17/28

وزارة الصحة ولاية الخرطوم
الادارة العامة للاستراتيجية والمعلومات
ادارة التطوير والابتكار والبحث العلمي

التاريخ 17/28 2019م

السيد/ المهندس الهادي الخامة

الموضوع : الموافقة على تنفيذ بحث

الرجاء السماح بتنفيذ بحث
Characterization of white matter
lesions on Brain Magnetic Resonance Images
using Texture Analysis

والذي يقوم به الباحث سليمان محمد العبد

ومنه بما يحتاج اليه من معلومات على ان يتم تنفيذ البحث حسب موجهات اللجنة الاخلاقية للبحوث.

بسم وجزاكم الله خير

د/منى فتح الرحمن عمر
مدير ادارة التطوير والابتكار والبحث العلمي

د/منى
17/28
الخامة

Appendix (B-4): the acceptance letter from the ministry of health



بِسْمِ اللَّهِ الرَّحْمَنِ الرَّحِيمِ
وزارة الصحة - ولاية الحارطوم
إدارة المؤسسات العلاجية الخاصة



التمرة: وص/وخ/م/ع/خ/١٤٤٤/٢

تاريخ: ١٩/ ذو الحجة / ١٤٤٠ هـ
الموافق: ٢٠/ أغسطس / ٢٠١٩ م

السيد / مدير طبي ...
مركزه الطبي

المحترم ...
السلام عليكم ورحمة الله وبركاته ...

الموضوع / الموافقة على تنفيذ بحث

إشارة للموضوع أعلاه، ننقل لكم موافقة الإدارة لتنفيذ بحث بعنوان :

Characterization Of White Matter Lesions On Brain Magnetic Resonance Images
Using Texure Analysis .

والذي ينفذه الباحث /سارة سليمان محمد الحسن ، الرجاء تسهيل مهمة
جمع البيانات للباحث ومدته بالمعلومات المساعدة .

.... والله ولي التوفيق


د. محمد عباس أحمد فوراوي
مدير إدارة المؤسسات العلاجية الخاصة

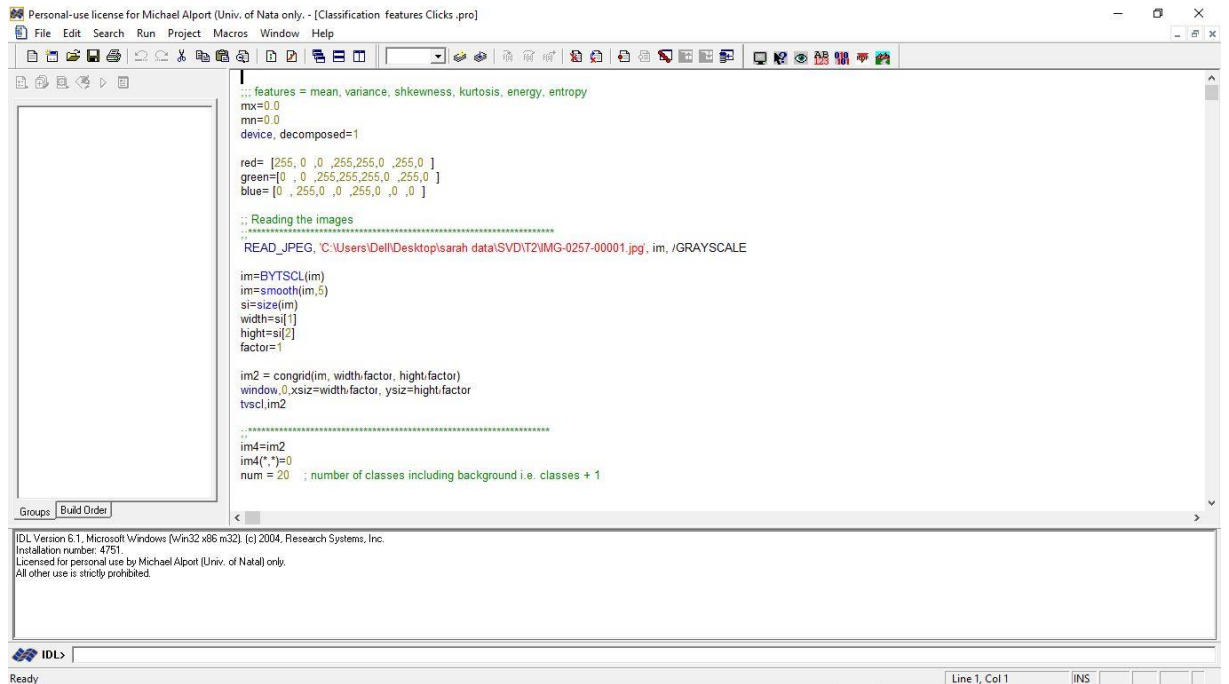


صورة إلى :
الملتف .

رؤية الوزارة : مجتمع بنعم بأفضل المستويات الصحية
رؤية الولاية : نحو عاصمة وطنية آمنة متحضرة
الحارطوم - حي الشاطئ - شمال أبراج الأمراء هاتف : ٠١٨٣٧٦١٢٩٢ Email: dpci.mohks@gmail.com

Appendix (B-5): the acceptance letter to Antaly medical center

Appendix (C)



```
Personal-use license for Michael Alport (Univ. of Natal only. - [Classification features Clicks .pro]
File Edit Search Run Project Macros Window Help
::: features = mean, variance, shkewness, kurtosis, energy, entropy
mx=0.0
mn=0.0
device, decomposed=1

red= [255, 0 ,0 ,255,255,0 ,255,0 ]
green=[0 ,0 ,255,255,255,0 ,255,0 ]
blue= [0 ,255,0 ,0 ,255,0 ,0 ,0 ]

::: Reading the images
.....
READ_JPEG, 'C:\Users\Dell\Desktop\sarah_data\SVD\T2\IMG-0257-00001.jpg', im, /GRAYSCALE

im=BYTSCALE(im)
im=smooth(im,5)
si=size(im)
width=si[1]
height=si[2]
factor=1

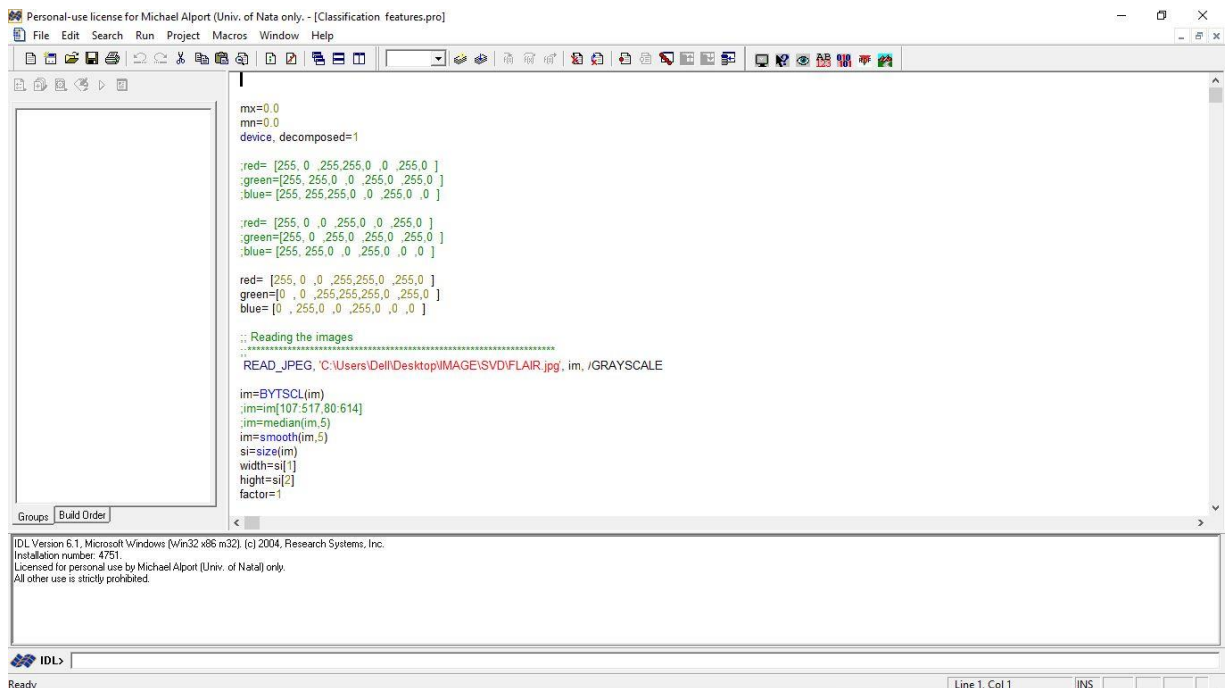
im2 = congrid(im, width*factor, height*factor)
window, 0, xsiz=width*factor, ysiz=height*factor
tvsc1, im2

.....
im4=im2
im4(*,*)=0
num = 20 ; number of classes including background i.e. classes + 1

IDL Version 6.1, Microsoft Windows [Win32; x86; m32] (c) 2004, Research Systems, Inc.
Installation number: 4751.
Licensed for personal use by Michael Alport (Univ. of Natal) only.
All other use is strictly prohibited.

IDL>
Ready Line 1, Col 1 INS
```

Appendix (C-1): classification features clicks program



```
Personal-use license for Michael Alport (Univ. of Natal only. - [Classification features.pro]
File Edit Search Run Project Macros Window Help
mx=0.0
mn=0.0
device, decomposed=1

:red= [255, 0 ,255,255,0 ,0 ,255,0 ]
:green=[255, 255, 0 ,0 ,255,0 ,255,0 ]
:blue= [255, 255, 255, 0 ,0 ,255,0 ,0 ]

:red= [255, 0 ,0 ,255,0 ,0 ,255,0 ]
:green=[255, 0 ,255,0 ,255,0 ,255,0 ]
:blue= [255, 255, 0 ,0 ,255,0 ,0 ,0 ]

red= [255, 0 ,0 ,255,255,0 ,255,0 ]
green=[0 ,0 ,255,255,255,0 ,255,0 ]
blue= [0 ,255,0 ,0 ,255,0 ,0 ,0 ]

::: Reading the images
.....
READ_JPEG, 'C:\Users\Dell\Desktop\IMAGE\SVD\FLAIR.jpg', im, /GRAYSCALE

im=BYTSCALE(im)
im=im[107:517,80:614]
im=median(im,5)
im=smooth(im,5)
si=size(im)
width=si[1]
height=si[2]
factor=1

IDL Version 6.1, Microsoft Windows [Win32; x86; m32] (c) 2004, Research Systems, Inc.
Installation number: 4751.
Licensed for personal use by Michael Alport (Univ. of Natal) only.
All other use is strictly prohibited.

IDL>
Ready Line 1, Col 1 INS
```

Appendix (C-2): classification features program (color map)

Appendix (D)

Appendix (D-1): first order statistical features equations, the histogram is a column vector h with each entry indexed by the grey level values and whose values is the number of voxels in the region of interest with that grey level value. Thus grey level value i appears within the ROI hi times.

1. Mean

$$\mu = \sum_{i=1}^{G_{max}} \{i \cdot h_i\}$$

2. Variance

$$\sigma^2 = \sum_{i=1}^{G_{max}} \{(i - \mu)^2 \cdot h_i\}$$

3. Skewness

$$s = \frac{1}{\sigma^3} \sum_{i=1}^{G_{max}} \{(i - \mu)^3 \cdot h_i\}$$

4. Kurtosis

$$k = \frac{1}{\sigma^4} \sum_{i=1}^{G_{max}} \{(i - \mu)^4 \cdot h_i\} - 3$$

5. Energy

$$Ene = \sum_{i=1}^{G_{max}} \{[h_i]^2\}$$

6. Entropy

$$Ent = - \sum_{i=1}^{G_{max}} \{h_i \cdot \ln[h_i]\}$$

Appendix (D-2): Higher order statistical features equations, Gray level values and gray level runs are denoted as keys of rows and columns, respectively, of the matrix, hence, the (i, j) -the entry in the matrix specifies the number of combinations whose gray level value is i and whose run length is j . By convention, we use P to denote a GLRLM, then P_{ij} is the (i, j) -the entry of the GLRLM. In addition, we use Nr to denote the set of different run lengths that actually occur in the ROI, and Ng the set of different gray levels exist in the ROI. And finally let N be

the number of total pixels in the ROI, then clearly we shall have the following ;

1.
$$N = \sum_{i \in N_g} \sum_{j \in N_r} j P_{ij}$$
2.
$$LRE = \sum_{i \in N_g} \sum_{j \in N_r} j^2 P_{ij} / \sum_{i \in N_g} \sum_{j \in N_r} P_{ij}$$
3.
$$SRE = \sum_{i \in N_g} \sum_{j \in N_r} \frac{P_{ij}}{j} / \sum_{i \in N_g} \sum_{j \in N_r} P_{ij}$$
4.
$$GLN = \sum_{i \in N_g} \left(\sum_{j \in N_r} P_{ij} \right)^2 / \sum_{i \in N_g} \sum_{j \in N_r} P_{ij}$$
5.
$$RLN = \sum_{j \in N_r} \left(\sum_{i \in N_g} P_{ij} \right)^2 / \sum_{i \in N_g} \sum_{j \in N_r} P_{ij}$$
6.
$$RP = \sum_{i \in N_g} \sum_{j \in N_r} P_{ij} / N$$
7.
$$LGRE = \sum_{i \in N_g} \sum_{j \in N_r} \frac{P_{ij}}{i^2} / \sum_{i \in N_g} \sum_{j \in N_r} P_{ij}$$
8.
$$HGRE = \sum_{i \in N_g} \sum_{j \in N_r} i^2 P_{ij} / \sum_{i \in N_g} \sum_{j \in N_r} P_{ij}$$
9.
$$SRLGE = \sum_{i \in N_g} \sum_{j \in N_r} \frac{P_{ij}}{i^2 j^2} / \sum_{i \in N_g} \sum_{j \in N_r} P_{ij}$$
10.
$$SRHGE = \sum_{i \in N_g} \sum_{j \in N_r} \frac{i^2 P_{ij}}{j^2} / \sum_{i \in N_g} \sum_{j \in N_r} P_{ij}$$
11.
$$LRLGE = \sum_{i \in N_g} \sum_{j \in N_r} \frac{j^2 P_{ij}}{i^2} / \sum_{i \in N_g} \sum_{j \in N_r} P_{ij}$$
12.
$$LRHGE = \sum_{i \in N_g} \sum_{j \in N_r} i^2 j^2 P_{ij} / \sum_{i \in N_g} \sum_{j \in N_r} P_{ij}$$

Characterization of Glioma on Brain Magnetic Resonance Images Using Texture Analysis

Sarah Suliman Mohammed^{1,2}, Mohammed Elfadeil Mohammed^{1,2}, Amal Sami Hegazi¹, Malaz Mohammed Ali³

¹ (Diagnostic radiology, College of medical radiological sciences / Sudan University of science and technology, Sudan)

²(National University-Sudan, College of radiography and medical imaging sciences, Khartoum, Sudan)

³(Al-Gad International Colleges for Applied Medical Sciences, Damam, Saudi Arabia)

Abstract:

Background: Texture analysis studies have been produced more often in oncology on the recent years; As it can increase the information that we can get from the radio-diagnostic images; here we took Glioma as it considered the most common malignant tumor of the brain; The study main concept is to use the texture analysis first order features for characterization of the Glioma which will give quantitative approach for the diagnosis.

Materials and Methods: In this cross sectional analytical study, the data was collected from Antalya medical center; it consists of 300 MR images for Glioma patients (50 T1, 100 T2, 100 FLAIR and 50 T1+C) age above 18years. After the images were selected the introduced to the it into the computer based software Interactive Data language (IDL) to extract the textural features (first order and higher order statistics) for gray matter, white matter and the Glioma; then the extracted features were entered to SPSS for analysis.

Results: For the first order statistics features the T2 weighted images shows the best differentiation of the glioma from normal brain tissues among all imaging sequences with accuracy = 99%, farther more the entropy texture feature in particular, demonstrated the best differentiation between the Glioma and the rest of classes; and it has the highest entropy in all imaging sequences. On the other hand the when using the higher order statistical features the MR imaging sequence that show the greatest discrimination accuracy is T1+C imaging sequence equal 93.6%, and the best higher order feature for classification of Glioma CLN textural feature which discriminates highly all classes in all imaging sequences; with the Glioma having the highest CLN in all imaging sequences.

Conclusion: Glioma were most different from the rest of brain tissues on T2 weighted images than the rest imaging sequences and with classification accuracy of 99% and sensitivity equal 98.2% when using first order statistical features and it can be diagnosed quantitatively from normal tissue by using the following equation:

$$\text{Glioma} = (19.977 \times \text{mean}) + (-.100 \times \text{variance}) + (1.830 \times \text{Kurtosis}) + (.053 \times \text{energy}) + (-2.363 \times \text{entropy}) - 217.467.$$

And when using the higher order statistical features the best discrimination was on T1+C images with accuracy = 94.8% and sensitivity equal 93.6% and it can be diagnosed quantitatively from normal tissue by using the following equation:

$$\text{Glioma} = (94.305 \times \text{SRE}) + (11.117 \times \text{LRE}) + (.009 \times \text{GLN}) + (79.843 \times \text{RP}) + (157.989 \times \text{LGRE}) + (-77.437 \times \text{SRLGE}) - 112.462$$

Key Word: Texture Analysis; Glioma; Magnetic Resonance Images; First Order Statistics; Higher order statistic.

Date of Submission: 20-02-2021

Date of Acceptance: 04-03-2021

I. Introduction

In neuroradiology the magnetic responses (MR) imaging give the best image resolution, soft-tissue differentiation and tumor delineation; also provide deferent kinds of images according to many physical factors for example: T1, T2 relaxation time and proton density of protons in tissue^{1,2}; then radiologists diagnosis this images according to their knowledge and experience; texture analysis increases the information that obtained from the images as it evaluate and computed the inter-relationships of the pixels^{3,4}; Texture analysis has many types on of them is the statistical based method which is depends on the pixel values, distribution, and spatial interrelationship in the defined region of interest; and it consist of First-order statistical texture analysis which is a histogram representation of image intensities in a predefined region of interest and calculates mean, variance, energy, skewness, entropy, uniformity, and kurtosis; While higher order statistical texture analysis

quantifies the image pattern on the basis of the spatial relationship or co-occurrence of the pixel value^{5,6}. Gliomas appears on magnetic resonance images as heterogeneous mass ,as it represent a mixture of solid tumor portions, necrosis and surrounding edema; the tumor portion have low signal intensity on T1-weighted images and as high signal intensity on T2/fluid attenuated inversion recovery (FLAIR) weighted images^{1,7}. The aim of the study is to characterize Glioma on brain magnetic resonance images using first order statistics texture features in Sudan.

II. Material And Methods

This analytical study of a case control type where normal T1, T2,T1+C and FLAIR MR Images of the brain taken as a reference was carried out at Antalya medical center and it was conducted from December 2018 to December 2020.

Study Design: Retrospective cross sectional analytical study

Study Location: At radiology department on Antalya medical center, Khartoum–Sudan.

Study Duration: December 2018 to December 2020.

Sample size: it consists of 300 MR images for Glioma patients (50 T1, 100 T2, 100 FLAIR and 50 T1 with contrast weighted images (T1+C))

Sample size calculation: convenient sample size

Subjects & selection method: The population of this study includes MR images for patients having Gliomas. The MR images were drawn from the picture archiving and communicating system (PACS) of Antalya medical center minutely and stored on computed disc the they was viewed by the Radiant, Ant- digital imaging and communication in medicine (DICOM) viewer in computer, to select the section of image that have the lesion on it and then this images uploaded it into the computer based software Interactive Data language (IDL) where the DICOM image converted to tagged image file format (TIFF) and the user then clicks on areas represents the white matter and lesion plaque.

Inclusion criteria:

1. Glioma patients
2. Either sex
3. Aged >18 years.

Exclusion criteria:

1. Patients having pathology other than Glioma..

Procedure methodology

The selected images uploaded it into the computer based software Interactive Data language (IDL) where the DICOM image converted to TIFF format and the user then clicks on areas represents the white matter, gray matter and Glioma . In these areas a window of 3×3 pixel was set and the first order statistics were extracted. Including the first order statistics features: mean, variance, skewness, kurtosis, energy and entropy. And a window of 6×6 pixel was set for higher order statistical features extraction which are Short Run Emphasis (SRE), Long Run Emphasis (LRE), Gray-Level Nonuniformity (GLN), Run-Length Nonuniformity (RLN), Run Percentage (RP), Low GrayLevel Run Emphasis (LGRE), High Gray-Level Run Emphasis (HGRE), Short Run Low Gray-Level Emphasis (SRLGE), Short Run High Gray-Level Emphasis (SRHGE), Long Run Low Gray-Level Emphasis (LRLGE), Long Run High GrayLevel Emphasis (LRHGE), These features were extracted for the predetermine classes (white matter, gray matter and lesion) for all lesion individually; then entered to SPSS for analysis.

Statistical analysis

Data was entered into SPSS version 20 (SPSS Inc., Chicago, IL) to generate a classification score using stepwise linear discriminate analysis; to select the most discriminate feature that can be used in the classification of white matter pathologies. Fisher exact tests were performed to test for differences in proportions of categorical variables between the groups; then scatter plot using discriminate function was generated as well as classification accuracy and linear discriminate function equation to differentiate between classes for unseen images.

III. Result

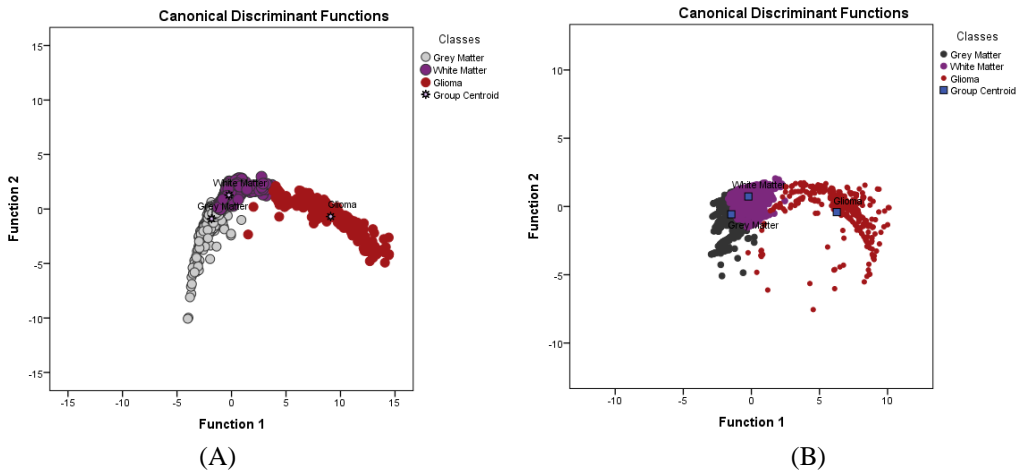


Figure no1: Scatter plot demonstrate the classification of brain tissues using linear discriminate analysis on T1 images for Glioma patients. First order features (A) and higher order features (B)

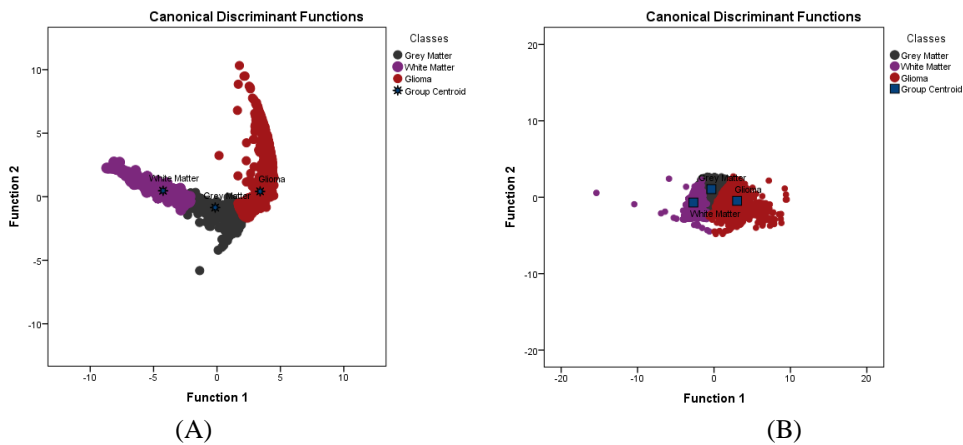


Figure no2: Scatter plot demonstrate the classification of brain tissues using linear discriminate analysis on T2 images for Glioma patients. First order features (A) and higher order features (B)

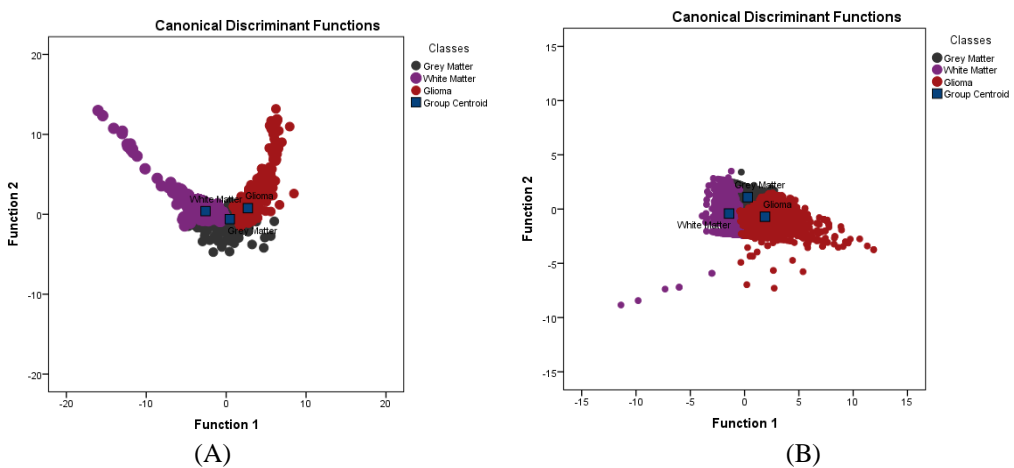


Figure no3: Scatter plot demonstrate the classification of brain tissues using linear discriminate analysis on FLAIR images for Glioma patients. First order features (A) and higher order features (B)

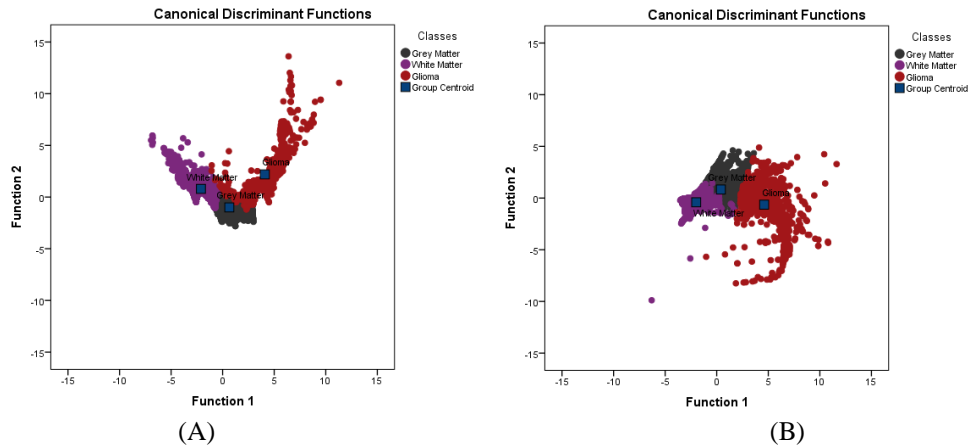


Figure no4: Scatter plot demonstrate the classification of brain tissues using linear discriminate analysis on T1+ C images for Glioma patients. First order features (A) and higher order features (B)

Table no1: Cross-tabulation shows the classification results of first order statistics using linear discriminate analysis on T1 images for Glioma patients.

Classes		Predicted Group Membership			Total
		Grey Matter	White Matter	Glioma	
Original	Grey Matter	99.8	.2	.0	100.0
	White Matter	6.5	93.5	.0	100.0
	Glioma	.4	4.0	95.6	100.0
a. 96.9% of original grouped cases correctly classified.					

Table no2: Cross-tabulation shows the classification results of first order statistics using linear discriminate analysis on T2 images for Glioma patients.

Classes		Predicted Group Membership			Total
		Grey Matter	White Matter	Glioma	
Original	Grey Matter	99.6	.4	.0	100.0
	White Matter	.9	99.1	.0	100.0
	Glioma	1.8	.0	98.2	100.0
a. 99.0% of original grouped cases correctly classified.					

Table no3: Cross-tabulation shows the classification results of first order statistics using linear discriminate analysis on FLAIR images for Glioma patients.

Classes		Predicted Group Membership			Total
		Grey Matter	White Matter	Glioma	
Original	Grey Matter	98.8	.8	.4	100.0
	White Matter	11.5	88.5	.0	100.0
	Glioma	16.9	.0	83.1	100.0
a. 92.2% of original grouped cases correctly classified.					

Table no4: Cross-tabulation shows the classification results of first order statistics using linear discriminate analysis on T1+C images for Glioma patients.

Classes		Predicted Group Membership			Total
		Grey Matter	White Matter	Glioma	
Original	Grey Matter	98.7	1.3	.0	100.0
	White Matter	7.7	92.3	.0	100.0
	Glioma	14.7	1.5	83.8	100.0
a. 94.8% of original grouped cases correctly classified.					

Table no5: Cross-tabulation shows the classification results of higher order statistics using linear discriminate analysis on T1 images for Glioma patients.

Classes		Predicted Group Membership			Total
		Grey Matter	White Matter	Glioma	
Original	Grey Matter	83.8	16.2	.0	100.0
	White Matter	11.5	88.5	.0	100.0
	Glioma	2.9	8.7	88.3	100.0
a. 86.3% of original grouped cases correctly classified.					

Table no6: Cross-tabulation shows the classification results of higher order statistics using linear discriminate analysis on T2 images for Glioma patients.

Classes		Predicted Group Membership			Total
		Grey Matter	White Matter	Glioma	
Original	Grey Matter	93.7	6.3	.0	100.0
	White Matter	7.3	92.7	.0	100.0
	Glioma	7.9	.9	91.3	100.0

a. 92.6% of original grouped cases correctly classified.

Table no7: Cross-tabulation shows the classification results of higher order statistics using linear discriminate analysis on FLAIR images for Glioma patients.

Classes		Predicted Group Membership			Total
		Grey Matter	White Matter	Glioma	
Original	Grey Matter	93.7	4.8	1.5	100.0
	White Matter	8.9	91.0	.1	100.0
	Glioma	7.9	10.7	81.4	100.0

a. 89.4% of original grouped cases correctly classified.

Table no8: Cross-tabulation shows the classification results tissues using linear discriminate analysis on T1+C images for Glioma patients.

Classes		Predicted Group Membership			Total
		Grey Matter	White Matter	Glioma	
Original	Grey Matter	92.4	7.6	.0	100.0
	White Matter	5.6	94.4	.0	100.0
	Glioma	6.2	.1	93.6	100.0

a. 93.6% of original grouped cases correctly classified.

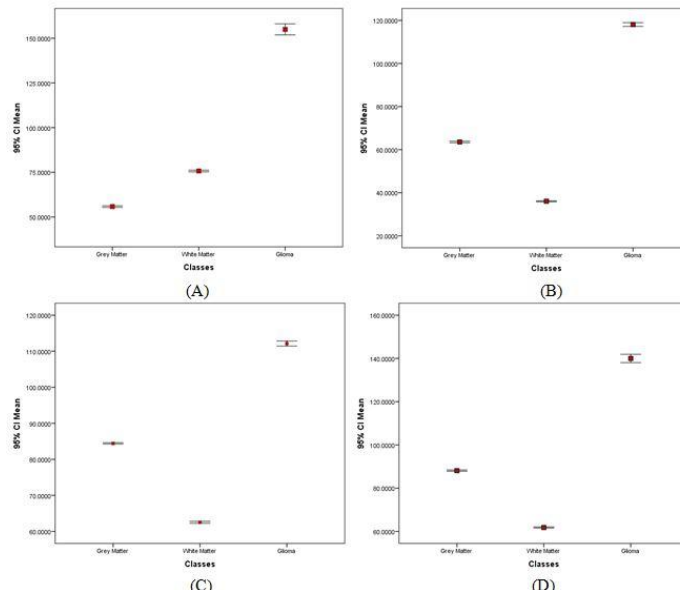


Fig 5: Error bar plot show the discriminate power of the Mean textural feature distribution for the selected classes on T1(A), T2(B), FLAIR(C) and T1+C(D) images for Glioma patients

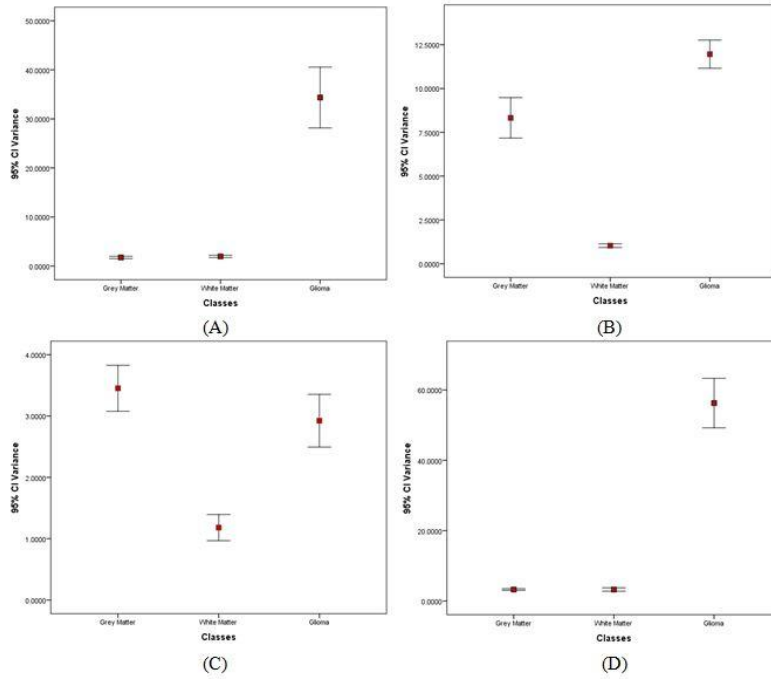


Fig 6: Error bar plot show the discriminate power of the Variance textural feature distribution for the selected classes on T1(A), T2(B), FLAIR(C) and T1+C(D) images for Glioma patients

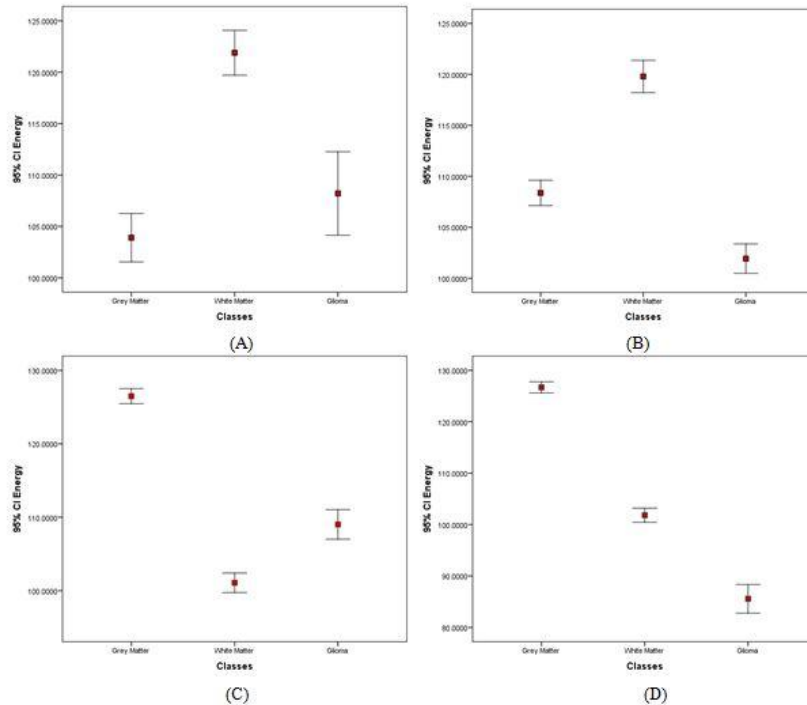


Fig 7: Error bar plot show the discriminate power of the Energy textural feature distribution for the selected classes on T1(A), T2(B), FLAIR(C) and T1+C(D) images for Glioma patients

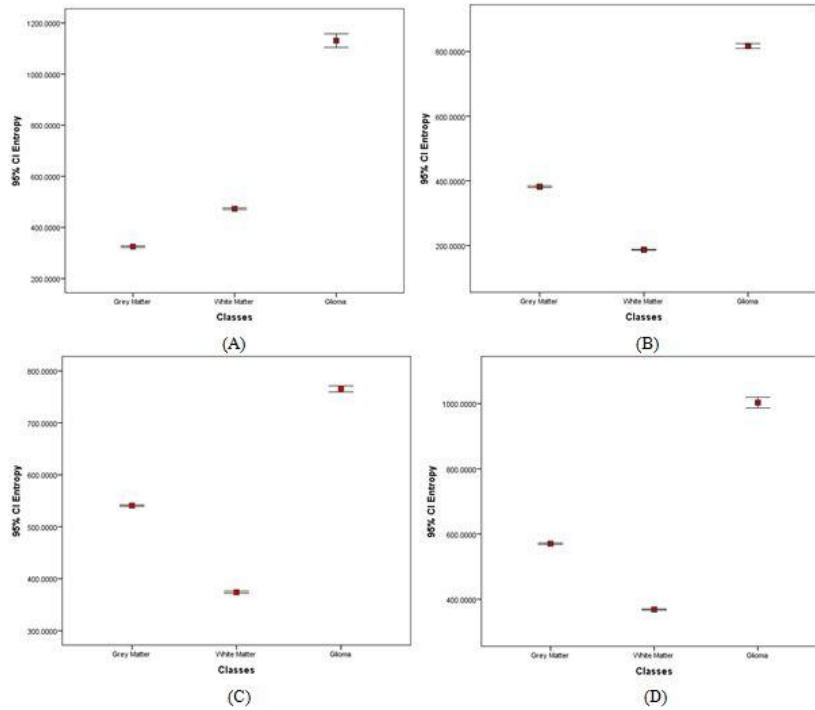


Fig 8: Error bar plot show the discriminate power of the Entropy textural feature distribution for the selected classes on T1(A), T2(B), FLAIR(C) and T1+C(D) images for Glioma patients

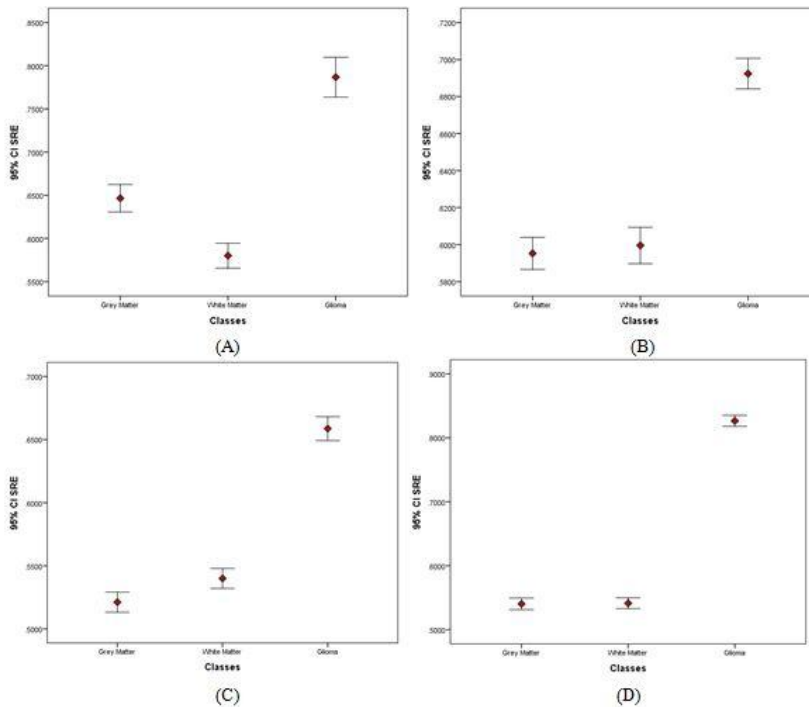


Fig 9: Error bar plot show the discriminate power of the SRE textural feature distribution for the selected classes on T1(A), T2(B), FLAIR(C) and T1+C(D) images for Glioma patients

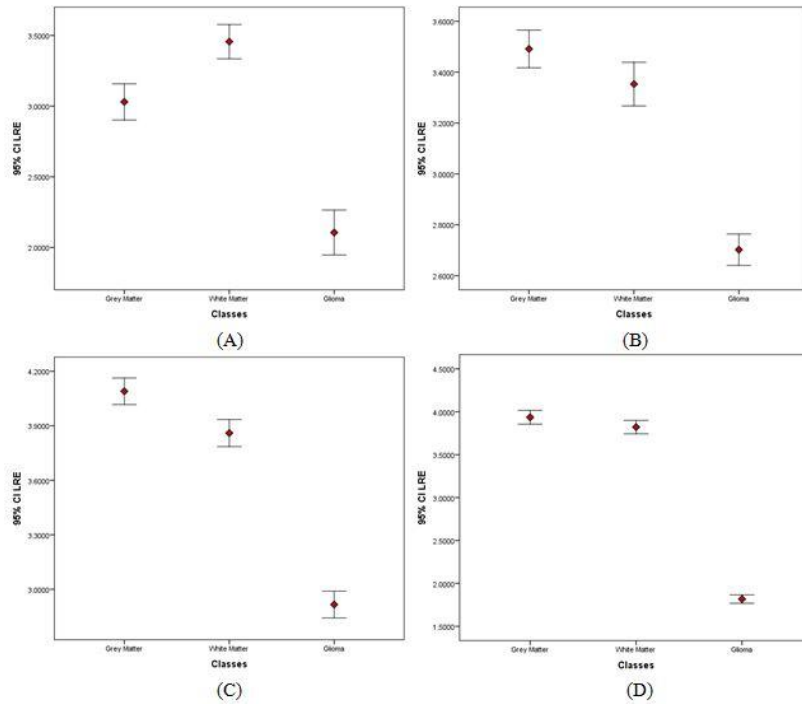


Fig 10: Error bar plot show the discriminate power of the LRE textural feature distribution for the selected classes on T1(A), T2(B), FLAIR(C) and T1+C(D) images for Glioma patients

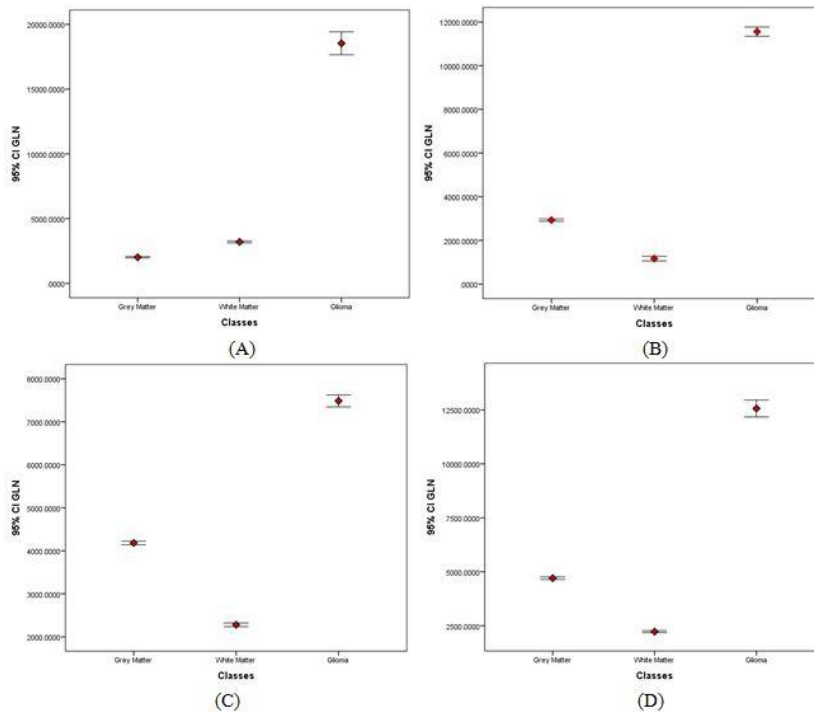


Fig 11: Error bar plot show the discriminate power of the GLN textural feature distribution for the selected classes on T1(A), T2(B), FLAIR(C) and T1+C(D) images for Glioma patients

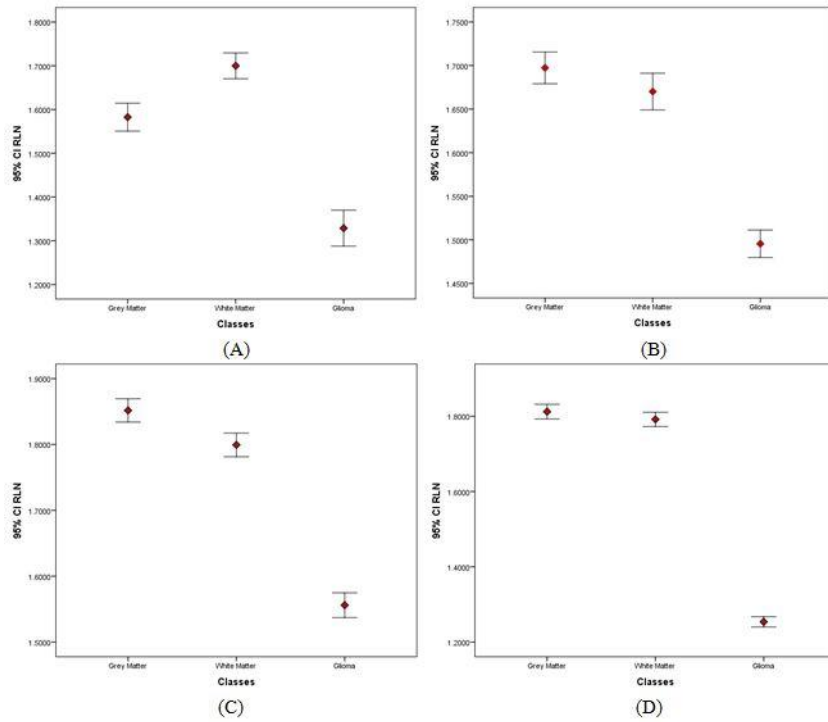


Fig 12: Error bar plot show the discriminate power of the RLN textural feature distribution for the selected classes on T1(A), T2(B), FLAIR(C) and T1+C(D) images for Glioma patients

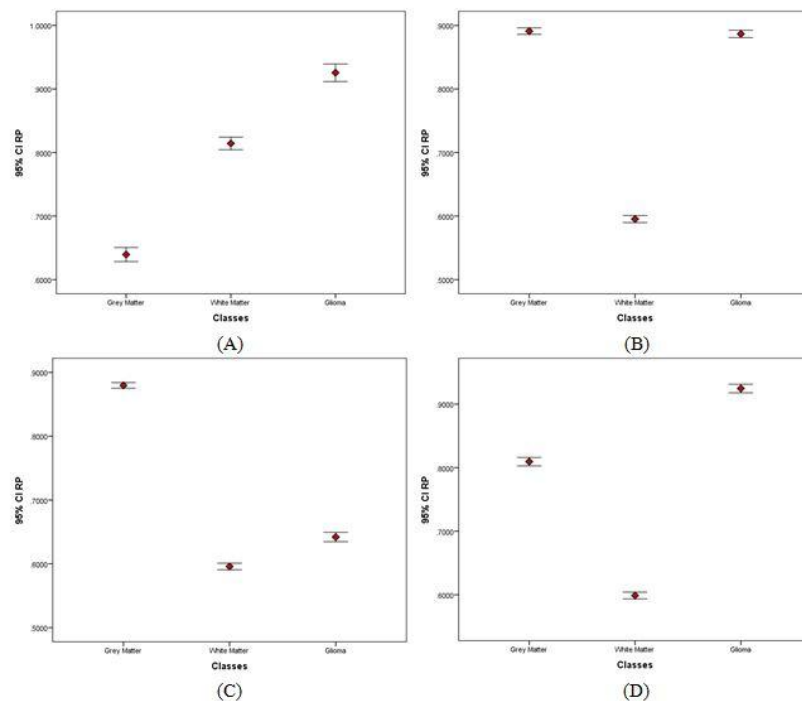


Fig 13: Error bar plot show the discriminate power of the RP textural feature distribution for the selected classes on T1(A), T2(B), FLAIR(C) and T1+C(D) images for Glioma patients

IV. Discussion

In this study there were three classes: gray matter, white matter and Glioma; from each one the First order statistical features and the higher order statistical features were extracted using IDL program; To classify the Glioma from normal brain tissue using linear discriminate analysis.

The result of classification using the first order and the higher order statistical features showed that Glioma is very different from the grey matter and white matter of the brain on T1, T2, T1+C and FLAIR images presented on Fig1 to Fig4; with classification accuracy using the first order textural features equal 99.0%, 96.9%, 94.8% and 92.2% on T2, T1, T1+C and FLAIR images respectively; and the sensitivity of detecting the Glioma in that order equal 98.2%, 95.6%, 83.8% and 83.1% shown from table1 to table4. While when using the higher order statistical features the highest accuracy was on T1+C then T2, FLAIR and lastly T1 images (=93.6%, 92.6%, 89.4% and 86.4% respectively); and sensitivity = 93.6%, 91.3%, 81.4% and 88.3% correspondingly. Table 5 to Table 8. Furthermore Tian et al also found that the T1+C was the best single sequence for glioma grading in MR texture analysis.

Firstly first order statistical features:

From fig5 when using the mean texture feature; the Glioma has the highest intensity in all imaging sequences; followed by grey matter then the white matter on T2, FLAIR and T1+C, while on T1 weighted images the white matter has higher intensity than the grey matter (as it contain fat).

Fig6 regarding the variance; Glioma had the highest variance on T2 weighted images followed by the grey matter and then the white matter; even though on T1 and T1+C have the highest variance, but there is an interference between the grey matter and white matter. While on FLAIR images the white matter has the highest variance and there is interference between the grey matter and the Glioma. Moreover Ditmer et al perform a study about detecting the accuracy grading the gliomas on MRI texture analysis and found that using the statistical parameter standard deviation at fine texture scale is the best to discriminate the gliomas grads with high a sensitivity and specificity on T1+C images. Also Skogen et al performed texture analysis using first order statistics using contrast enhancing MR images and found standard deviation parameters at a fine texture highly significant in distinguishing low grad gliomas from high grad gliomas

From fig7 When using the energy texture feature (contrast); on T2 images the Glioma has the highest energy (as a result to the presence of edema); and after the fluid attenuation on FLAIR images the Glioma has energy in between the grey matter highest and the white matter lowest than it. While on T1 images the white matter has the highest contrast, then then Glioma then the grey matter, and there is interference Glioma and the gray matter; after introducing contrast media to the patient on T1+C images the interference has gone; and the energy textural feature has discriminate well between the classes (the white matter has the highest energy followed grey matter and finally the Glioma which had the lowest energy).

Regarding the entropy texture feature, it highly differentiate between the Glioma and the rest of classes; it has the highest entropy followed by grey matter then the white matter on T2, FLAIR and T1+C images, but on T1 weighted images the white matter has entropy greater than the grey matter from fig8. Comparable Xie et al perform a study on dynamic contrast enhanced MRI texture analysis for glioma grading and observed that the entropy was able to differentiate glioma grades on T1+C images, same as declared by Soni et al that entropy values consistently exhibited promising results for differentiating low-grade gliomas from high-grade gliomas.

The skewness discriminate the Glioma in T1 and FLAIR images; on the T1 images the Glioma had the lowest skewness, while on FLAIR images the white matter had lowest skewness than the Glioma and the grey matter which had the highest skewness.

Secondly higher order statistical features:

SRE highly distinguished between the Glioma from the other classes in all MR imaging sequences and had the highest SRE value, followed by the grey matter then the white matter on the T1 and FLAIR images; but on the T1+C and T2 images there interference between the grey matter and white matter presented on fig9.

From fig10 LRG textural feature also differentiate well the Glioma from the remnant classes in all imaging sequences and it had the lowest LRG; moreover there is interference between the grey matter and the white matter on T2 and T1+C images.

CLN discriminates highly between all classes in all imaging sequences; and the Glioma had the highest CLN in all imaging sequences followed by the grey matter then the white matter on T2, T1+C and FLAIR images, but on T1 images followed by the white matter then the grey matter as presented in fig 11.

From fig 12 regarding RLN textural feature it discriminates the Glioma from the grey matter and the white matter in all imaging sequences, and it had the lowest value from all classes in all imaging sequences; but on T2 and T1+C images there interference the grey matter and white matter.

RP firstly for T1 and T1+C images it differentiates well between the Glioma and the rest of the classes, and the Glioma had the highest RP in both imaging sequences. While on FLAIR images the grey matter had the highest RP then the Glioma and then the white matter which has the lowest RP. Finally on the T2 images the white matter had the highest RP and there interference between the Glioma and the grey matter as presented on fig13.

Finally the LGRE textural feature it differentiate the Glioma from the normal tissue on T1 an T1+C images only, and it had the highest LGRE on both sequences, but the Glioma in the T1 images shows wide dispersion .

V. Conclusion

In conclusion Glioma can be diagnosed quantitatively from normal tissue by:

Firstly on the first order statistics:

*sensitivity equal to **98.2%** on **T2** images using the following equations:

$$\text{Glioma} = (19.977 \times \text{mean}) + (-.100 \times \text{variance}) + (1.830 \times \text{Kurtosis}) + (.053 \times \text{energy}) + (-2.363 \times \text{entropy}) - 217.467$$

$$\text{White matter} = (13.668 \times \text{mean}) + (-.053 \times \text{variance}) + (1.059 \times \text{Kurtosis}) + (.061 \times \text{energy}) + (-1.635 \times \text{entropy}) - 98.053$$

$$\text{Grey matter} = (17.800 \times \text{mean}) + (-.067 \times \text{variance}) + (1.781 \times \text{Kurtosis}) + (.053 \times \text{energy}) + (-2.123 \times \text{entropy}) - 163.923$$

*sensitivity equal to **95.6%** on **T1** images using the following equations:

$$\text{Glioma} = (20.230 \times \text{mean}) + (.277 \times \text{variance}) + (-5.500 \times \text{skewness}) + (.206 \times \text{energy}) + (-2.321 \times \text{entropy}) - 275.570$$

$$\text{White matter} = (23.640 \times \text{mean}) + (-.103 \times \text{variance}) + (-5.337 \times \text{skewness}) + (.219 \times \text{energy}) + (-2.851 \times \text{entropy}) - 238.220$$

$$\text{Grey matter} = (21.471 \times \text{mean}) + (-.129 \times \text{variance}) + (-4.689 \times \text{skewness}) + (.192 \times \text{energy}) + (-2.605 \times \text{entropy}) - 189.823$$

*sensitivity equal to **83.8%** on **T1+C** images using the following equations:

$$\text{Glioma} = (33.284 \times \text{mean}) + (.047 \times \text{variance}) + (.265 \times \text{energy}) + (-3.955 \times \text{entropy}) - 360.222$$

$$\text{White matter} = (31.523 \times \text{mean}) + (-.013 \times \text{variance}) + (.259 \times \text{energy}) + (-3.796 \times \text{entropy}) - 288.834$$

$$\text{Grey matter} = (35.007 \times \text{mean}) + (-.010 \times \text{variance}) + (.298 \times \text{energy}) + (-4.202 \times \text{entropy}) - 364.053$$

*sensitivity equal to **83.1%** on **FLAIR** images using the following equations:

$$\text{Glioma} = (43.313 \times \text{mean}) + (.456 \times \text{variance}) + (-1.354 \times \text{skewness}) + (.209 \times \text{energy}) + (-5.206 \times \text{entropy}) - 449.781$$

$$\text{White matter} = (39.778 \times \text{mean}) + (.426 \times \text{variance}) + (-1.425 \times \text{skewness}) + (.165 \times \text{energy}) + (-4.830 \times \text{entropy}) - 351.069$$

$$\text{Grey matter} = (43.227 \times \text{mean}) + (.471 \times \text{variance}) + (-1.642 \times \text{skewness}) + (.201 \times \text{energy}) + (-5.227 \times \text{entropy}) - 427.022$$

Secondly on the higher order statistics:

*sensitivity equal to **93.6%** on **T1+C** images using the following equations:

$$\text{Glioma} = (94.305 \times \text{SRE}) + (11.117 \times \text{LRE}) + (.009 \times \text{GLN}) + (79.843 \times \text{RP}) + (157.989 \times \text{LGRE}) + (-77.437 \times \text{SRLGE}) - 112.462$$

$$\text{White matter} = (98.729 \times \text{SRE}) + (10.535 \times \text{LRE}) + (.005 \times \text{GLN}) + (71.341 \times \text{RP}) + (-183.077 \times \text{LGRE}) + (-104.702 \times \text{SRLGE}) - 68.796$$

$$\text{Grey matter} = (99.810 \times \text{SRE}) + (10.712 \times \text{LRE}) + (.007 \times \text{GLN}) + (79.136 \times \text{RP}) + (-87.865 \times \text{LGRE}) + (-143.967 \times \text{SRLGE}) - 84.798$$

*sensitivity equal to **91.3%** on **T2** images using the following equations:

$$\text{Glioma} = (3018.801 \times \text{SRE}) + (-735.729 \times \text{LRE}) + (.010 \times \text{GLN}) + (4323.954 \times \text{RLN}) + (125.574 \times \text{RP}) - 3355.977$$

$$\text{White matter} = (3010.589 \times \text{SRE}) + (-734.551 \times \text{LRE}) + (.006 \times \text{GLN}) + (4315.083 \times \text{RLN}) + (105.704 \times \text{RP}) - 3307.723$$

$$\text{Grey matter} = (3024.061 \times \text{SRE}) + (-735.840 \times \text{LRE}) + (.008 \times \text{GLN}) + (4325.909 \times \text{RLN}) + (126.052 \times \text{RP}) - 3347.503$$

*sensitivity equal to **81.4%** on **FLAIR** images using the following equations:

$$\text{Glioma} = (204.564 \times \text{SRE}) + (.008 \times \text{GLN}) + (102.857 \times \text{RLN}) + (71.911 \times \text{RP}) - 181.097$$

$$\text{White matter} = (208.547 \times \text{SRE}) + (.005 \times \text{GLN}) + (103.777 \times \text{RLN}) + (73.037 \times \text{RP}) - 172.733$$

$$\text{Grey matter} = (210.897 \times \text{SRE}) + (.007 \times \text{GLN}) + (104.680 \times \text{RLN}) + (83.014 \times \text{RP}) - 187.687$$

*sensitivity equal to **88.3%** on **T1** images using the following equations:

$$\text{Glioma} = (91.169 \times \text{SRE}) + (8.573 \times \text{LRE}) + (.007 \times \text{GLN}) + (83.018 \times \text{RP}) + (-151.252 \times \text{LGRE}) - 108.927$$

$$\text{White matter} = (102.659 \times \text{SRE}) + (9.108 \times \text{LRE}) + (.004 \times \text{GLN}) + (85.814 \times \text{RP}) + (-273.059 \times \text{LGRE}) - 76.855$$

$$\text{Grey matter} = (102.199 \times \text{SRE}) + (9.358 \times \text{LRE}) + (.003 \times \text{GLN}) + (74.818 \times \text{RP}) + (-246.055 \times \text{LGRE}) - 67.418$$

References

- [1]. Grainger RG, Allison DJ, Baert A. Diagnostic radiology: A text book of medical imaging. sixth Edition. Churchill Livinstone. Bruno Graça Luis Curvo Semedo Miguel Seco Belarmino Gonçalves Cristina Marques Filipe Caseiro-Alves. 2015.
- [2]. VN, Pronin IN. Diagnostic neuroradiology. 2009
- [3]. Castellano G, Bonilha L, Li LM, Cendes F. Texture analysis of medical images. Clinical radiology. 2004 Dec 1;59(12):1061-9.
- [4]. Kassner A, Thornhill RE. Texture analysis: a review of neurologic MR imaging applications. American Journal of Neuroradiology. 2010 May 1;31(5):809-16.
- [5]. Kolosva ry M, Kellermayer M, Merkely B, et al. Cardiac computed tomography radiomics: a comprehensive review on radiomic techniques. J Thorac Imaging 2018;33:26-34

- [6]. Soni N, Priya S, Bathla G. Texture analysis in cerebral gliomas: a review of the literature. *American Journal of Neuroradiology*. 2019 Jun 1;40(6):
- [7]. Eisenberg RL, Johnson NM. *Comprehensive Radiographic Pathology*. sixth edition. Elsevier Health Sciences. 2016
- [8]. Tian Q, Yan LF, Zhang X, Zhang X, Hu YC, Han Y, Liu ZC, Nan HY, Sun Q, Sun YZ, Yang Y. Radiomics strategy for glioma grading using texture features from multiparametric MRI. *Journal of Magnetic Resonance Imaging*. 2018 Dec;48(6):1518-28.
- [9]. Ditmer A, Zhang B, Shujaat T, Pavlina A, Luibrand N, Gaskill-Shibley M, Vagal A. Diagnostic accuracy of MRI texture analysis for grading gliomas. *Journal of Neuro-oncology*. 2018 Dec;140(3):583-9.
- [10]. Skogen K, Schulz A, Dormagen JB, Ganeshan B, Helseth E, Server A. Diagnostic performance of texture analysis on MRI in grading cerebral gliomas. *European journal of radiology*. 2016 Apr 1;85(4):824-9.
- [11]. Xie T, Chen X, Fang J, Kang H, Xue W, Tong H, Cao P, Wang S, Yang Y, Zhang W. Textural features of dynamic contrast-enhanced MRI derived model-free and model-based parameter maps in glioma grading. *Journal of Magnetic Resonance Imaging*. 2018 Apr;47(4):1099-111.

Sarah Suliman Mohammed, et. al. "Characterization of Glioma on Brain Magnetic Resonance Images Using Texture Analysis ." *IOSR Journal of Dental and Medical Sciences (IOSR-JDMS)*, 20(03), 2021, pp. 30-41.

Characterization of White Matter Lesions on Brain Magnetic Resonance Images Using Texture Analysis

Sarah Suliman Mohammed^{1,2}, Prof. Mohammed Elfadil Mohammed^{1,2}, Amal Sami Hegazi¹, Malaz Mohammed Ali³

¹ (Diagnostic radiology, College of medical radiological sciences / Sudan University of science and technology, Sudan)

² (National University-Sudan, College of radiography and medical imaging sciences, Khartoum, Sudan)

³ (Al-Gad International Colleges for Applied Medical Sciences, Damam, Saudi Arabia)

Abstract:

Background: The lesions that affect white matter of the brain could be due to a variety of causes this study discusses the inflammatory, demyelinating, tumors and lesions found in normal ageing process. The main concept of this study was to use the texture analysis mainly first order features for classification and identification of these lesions which will give quantitative approach for the differential diagnosis between them.

Materials and Methods: In this analytical study, the data consist of 98 patients (18MS, 10 SVD and 70 Glioma) age above 18 years old. After the images were selected then by using function generated by computer based software Interactive Data language (IDL) in order to extract the predetermined features from gray matter, white matter, Glioma, MS and SVD lesions; then the extracted features were statistically analyzed.

Results: The result reveal that the SVD have been differentiated from the rest of the classes by sensitivity equal to 100.0% when using both the first and higher order statistics. In general the best first order textural feature for distinguishing between all classes was the energy. Farther more the best higher order features for differentiation between the three lesions are SRE, LRE, RLN and LGRE on T1+C MR Images.

Conclusion: Higher order statistics using linear discriminate analysis on T1+C MR Images for patients with Glioma, MS and SVD have higher discrimination accuracy (equal to 96.%) and with a sensitivity equal to 96.3%, 93.0 and 100.0% respectively than first order statistics.

Key Word: White Matter; Magnetic Resonance Imaging; Texture Analysis; Glioma; Multiple Sclerosis; Small Vessels Disease.

Date of Submission: 22-02-2021

Date of Acceptance: 07-03-2021

I. Introduction

The White matter formed of the axons of neurons and concenter the medullary core of the brain; the abnormalities that can affect it are varied; in this study Glioma, Multiple Sclerosis (MS) and Small Vessels Disease (SVD) were chosen as type of tumor, demyelinating and vascular respectively^{1,2}. First Gliomas, concenter the most common malignant brain tumors, reside of glial cells that still have the ability to multiply; they spread by direct extension and can cross from one cerebral hemisphere to the other through connecting white matter tracts³. While Multiple sclerosis (MS) is a chronic autoimmune disease that affects the central nervous system (primarily involve the spinal cord, optic nerves, and central white matter of the brain); MS attacks the myelinated axons, destroying the myelin and the axons to varying degrees (most common demyelinating disorder)^{3,4}. More over cerebral small vessel disease (SVD) is a generic term that refers to intracranial vascular disease based on various pathological and neurological processes, as well as a syndrome referring to different clinical manifestations and neuroimaging features caused by the structural changes of vascular and brain parenchyma⁵. In neuroradiology the magnetic responses imaging give the best image resolution and give deferent kinds of images according to many physical factors for example: T1, T2 relaxation time and proton density of protons in tissue⁶; then radiologists diagnosis this images according to their knowledge and experience; texture analysis increases the information that obtained from the images as it evaluate and computed the inter-relationships of the pixels^{7, 8}. The aim of the study is to characterize white matter lesions on brain magnetic resonance images using first order statistics texture features in Sudan.

II. Material And Methods

This analytical study was carried out on Antalya medical center and it was conducted from December 2018 to December 2020.

Study Design: analytical study

Study Location: at radiology department on Antalya medical center, Khartoum –Sudan.

Study Duration: December 2018 to December 2020.

Sample size: 98 patients.

Sample size calculation: convenient sample size

Subjects & selection method: The population of this study includes MR images for patients having: Small Vessels Disease (SVD), Multiple Sclerosis plaque (MS) as demyelinating diseases and Gliomas as a tumor. The MR images viewed by the Radiant, Ant . DICOM viewer in the computer, to select the section of image that have the lesion on it and then this images introduced it into the computer based software Interactive Data language (IDL) and the user then clicks on areas represents the grey matter, white matter, Glioma, MS and SVD lesion plaque.

Inclusion criteria:

1. Glioma, MS and SVD patients
2. Aged >18 years,

Exclusion criteria:

1. Patients having two types of lesions at the same time.

Procedure methodology

The selected images uploaded it into the computer based software Interactive Data language (IDL) and the user then clicks on areas represents the white matter, gray matter, Glioma, MS and SVD lesion plaque. In these areas a window of 3×3 pixel was set for the first order statistics features extraction, and a window of 6×6 pixel was set for the higher order features extraction; for the predetermine classes (white matter, gray matter and lesions). The first order statistical features included are the mean, variance, kurtosis, skewness, energy and entropy. More over the higher order statistical features are: Short Run Emphasis (SRE), Long Run Emphasis (LRE), Gray-Level Non-uniformity (GLN), Run-Length Non-uniformity (RLN), Run Percentage (RP), Low Gray Level Run Emphasis (LGRE), High Gray-Level Run Emphasis (HGRE), Short Run Low Gray-Level Emphasis (SRLGE), Short Run High Gray-Level Emphasis (SRHGE), Long Run Low Gray-Level Emphasis (LRLGE), Long Run High Gray Level Emphasis (LRHGE). Then these features were entered to SPSS for analysis.

Statistical analysis

Data was analyzed using SPSS version 20, using stepwise linear discriminate analysis to generate a classification score; to select the most discriminate feature that can be used in the classification of the lesions from each other. Fisher exact tests were performed to test for differences in proportions of categorical variables between the groups; then scatter plot using discriminate function was generated as well as classification accuracy and linear discriminate function equation.

III. Result

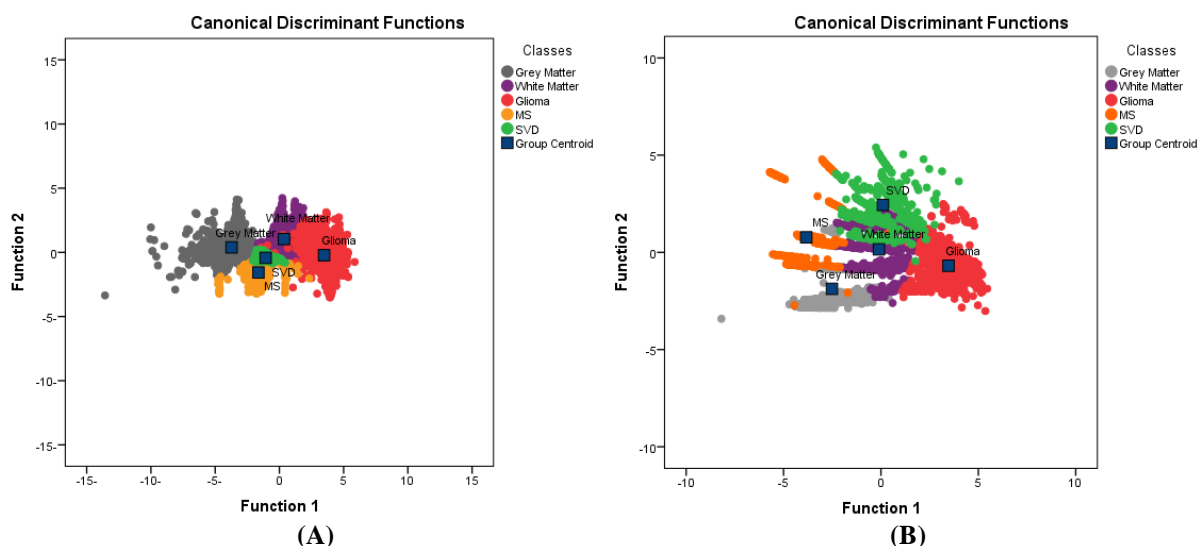


Figure no1: Scatter plots demonstrate the classification of white matter lesions using linear discriminate analysis on T1+C MR images for patients with Glioma, MS and SVD. First order features (A) and higher order features (B)

Table no1: Cross-tabulation shows the classification results of first order statistics using linear discriminate analysis on T1+C MR Images for patients with Glioma, MS and SVD.

Classes		Predicted Group Membership					Total
		Grey Matter	White Matter	Glioma	MS	SVD	
Original	Grey Matter	89.7	.0	.0	5.4	4.9	100.0
	White Matter	.0	87.3	.0	.0	12.7	100.0
	Glioma	.0	12.2	87.3	.0	.5	100.0
	MS	2.0	.3	.2	80.3	17.3	100.0
	SVD	.0	.0	.0	.0	100.0	100.0

a. 87.2% of original grouped cases correctly classified.

Table no2: Cross-tabulation shows the classification results of Higher order statistics using linear discriminate analysis on T1+C MR Images for patients with Glioma, MS and SVD.

Classes		Predicted Group Membership					Total
		Grey Matter	White Matter	Glioma	MS	SVD	
Original	Grey Matter	97.5	.0	.1	1.4	1.0	100.0
	White Matter	4.6	93.1	.0	2.3	.0	100.0
	Glioma	.0	3.0	96.3	.0	.6	100.0
	MS	.7	.0	.0	93.0	6.3	100.0
	SVD	.0	.0	.0	.0	100.0	100.0

a. 96.2% of original grouped cases correctly classified.

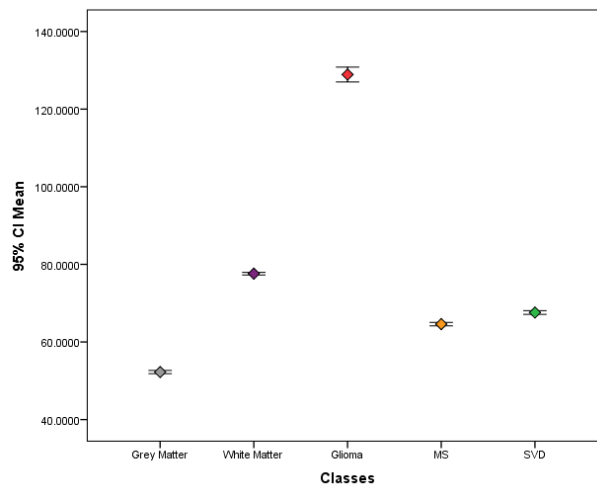


Fig 2: Error bar plot show the discriminate power of the Mean textural feature distribution for the selected classes on T1+C MR Images for patients with Glioma, MS and SVD.

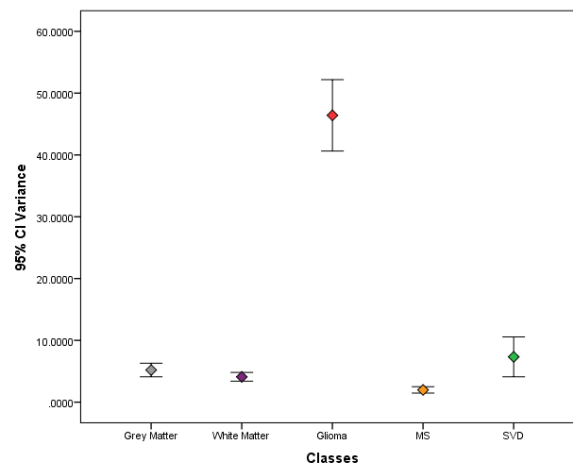


Fig 3: Error bar plot show the discriminate power of the Variance textural feature distribution for the selected classes on T1+C MR Images for patients with Glioma, MS and SVD.

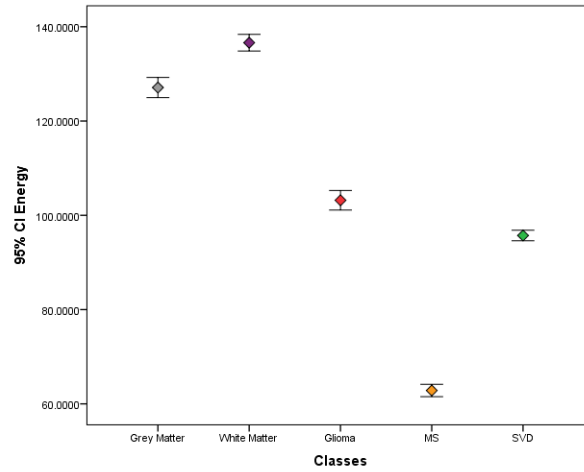


Fig 4: Error bar plot show the discriminate power of the Energy textural feature distribution for the selected classes on T1+C MR Images for patients with Glioma, MS and SVD.

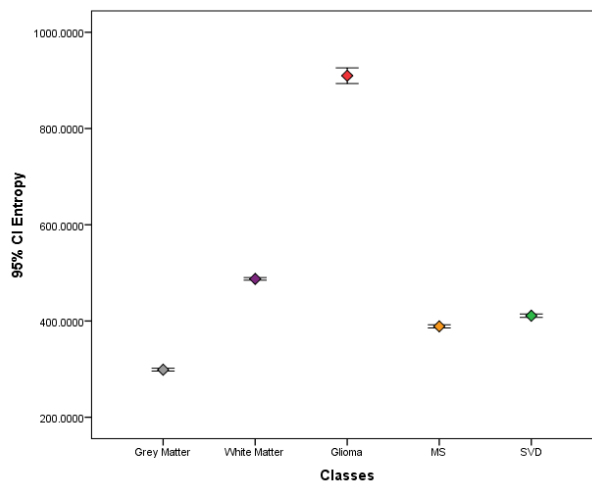


Fig 5: Error bar plot show the discriminate power of the Entropy textural feature distribution for the selected classes on T1+C MR Images for patients with Glioma, MS and SVD.

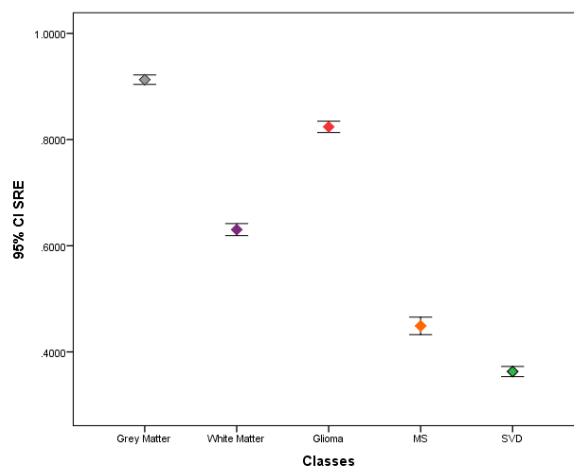


Fig 6: Error bar plot show the discriminate power of the SRE textural feature distribution for the selected classes on T1+C MR Images for patients with Glioma, MS and SVD.

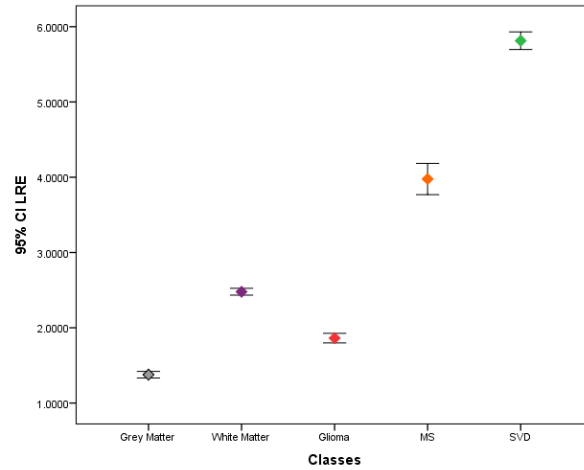


Fig 7: Error bar plot show the discriminate power of the LRE textural feature distribution for the selected classes on T1+C MR Images for patients with Glioma, MS and SVD.

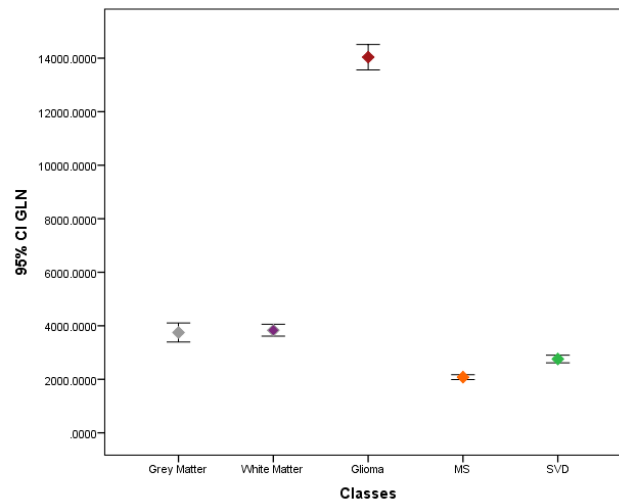


Fig 8: Error bar plot show the discriminate power of the GLN textural feature distribution for the selected classes on T1+C MR Images for patients with Glioma, MS and SVD.

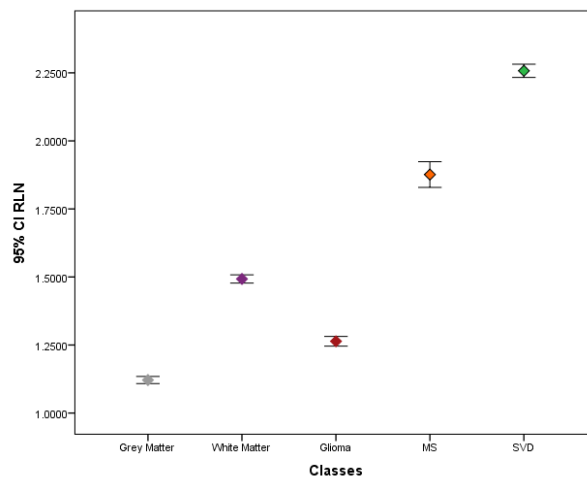


Fig 9: Error bar plot show the discriminate power of the RLN textural feature distribution for the selected classes on T1+C MR Images for patients with Glioma, MS and SVD.

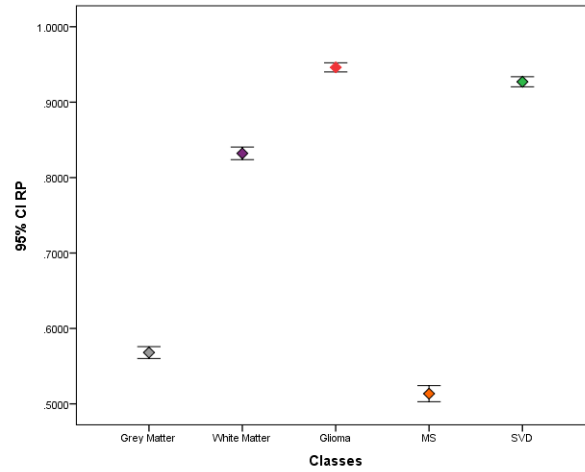


Fig 10: Error bar plot show the discriminate power of the RP textural feature distribution for the selected classes on T1+C MR Images for patients with Glioma, MS and SVD.

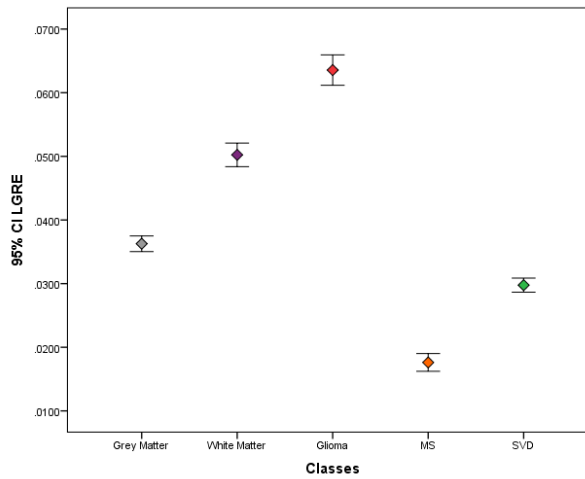


Fig 11: Error bar plot show the discriminate power of the LGRE textural feature distribution for the selected classes on T1+C MR Images for patients with Glioma, MS and SVD.

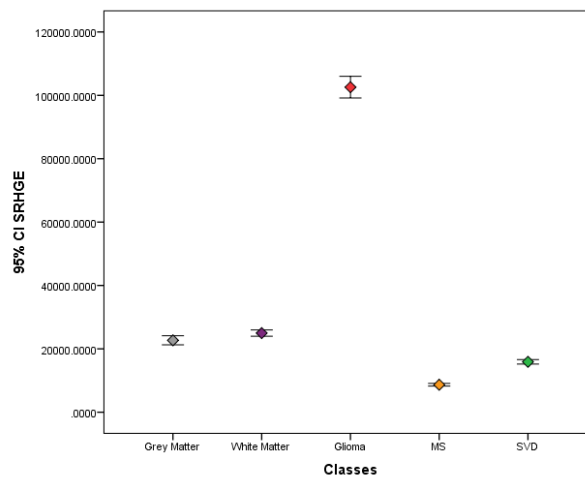


Fig 12: Error bar plot show the discriminate power of the SRHGE textural feature distribution for the selected classes on T1+C MR Images for patients with Glioma, MS and SVD.

IV. Discussion

The main aim of this study is to characterize white matter lesions (Glioma, Multiple Sclerosis (MS) and Small Vassals Disease (SVD)) on contrast enhanced T1weighted images (T1+C). The result of classification using the first order and the higher order statistical features showed that all classes are very different from each other as the center of each class (blue square) is away from the other on T1+C images presented on Fig1; with classification accuracy using the first order textural features equal 87.2%; and the sensitivity of detecting the Glioma, MS and SVD equal 87.3%, 80.3%, 100% respectively, shown from table1. While when using the higher order statistical features the accuracy was on T1+C equal 96.2%; and sensitivity equal 96.3%, 93.0% and 100% for the Glioma, MS and SVD correspondingly, as presented in Table 2

Fig 2 show the excellent discrimination of the mean textural feature between all classes, with the Glioma having the highest mean then white matter then SVD followed by MS and the grey matter have the lowest value. And when using the variance for discrimination presented on fig 3, it provide a well differentiation between the three lesions (Glioma, SVD and MS) with the Glioma having the highest value with showing wide-ranging; also there is interference between the white matter and the gray matter.

Regarding the energy textural feature which shows the best differentiation between all classes among all first order features, with the white matter having the highest energy followed by the grey matter then the Glioma then SVD, finally the MS having the lowest energy, as presented on fig 4. While fig 5 demonstrate that the entropy distinguished well between all classes with the Glioma having the highest value then the white matter, SVD, MS and the grey matter have the lowest value.

Fig6 show the result of the discrimination of the SRE textural feature and reveal that the grey matter have the highest value the Glioma, white matter, MS and SVD in that order with the lowest value. Also the LRE textural feature well differentiate between all classes, with the SVD have the highest value then the MS then the white matter followed by the Glioma and the grey matter have the lowest LRE value as presented in fig 7. Farther more GLN feature distinguished well between the Glioma, SVD and MS but there was interference between the grey matter and the white matter presented at fig 8.

From fig 9 the RLN feature differentiates well between all classes; with the SVD have the highest RLN value then the MS, white matter, Glioma and the grey matter have the lowest value. While regarding the RP feature have discriminate well between all classes, with the Glioma having the highest value while the MS having the lowest value, as presented at fig 10. Farther more the LGRE textural feature on fig 11 which show good differentiation between all classes, also the Glioma having the highest value while the MS having the lowest value.

Finally the SRHGE textural feature at fig 12 show an excellent discrimination between all classes; with the Glioma having the highest value then the white matter followed by grey matter then SVD lastly came MS.

V. Conclusion

In conclusion: the best first order textural feature for distinguishing between the classes is the energy, also the Glioma have the highest value in all first order statistics used on this study while the MS having the lowest vale in all. On the other hand the best higher order features for differentiation between the three lesions are SRE, LRE, RLN and LGRE; more over the best features for discrimination of Glioma from the rest are the GLN, LGRE and the SRHGE; with it having the highest value in each one of them. In case of MS the finest feature that differentiates it from the other lesions is the RP textural feature, as the MS having the lowest RP value among all classes. Finally regarding the SVD the best discrimination features are the LRE and the RLN; with SVD have the highest value on both. And they can be diagnosed quantitatively from normal tissue by using the following equations:

Firstly on the first order statistics with a sensitivity of Glioma, MS and SVD equal to 87.3%, 80.3% and 100.0% respectively on T1+C images using the following equations:

$$\text{Gray matter} = (30.456 \times \text{mean}) + (.004 \times \text{variance}) + (.212 \times \text{energy}) + (-3.580 \times \text{entropy}) - 275.748$$

$$\text{White matter} = (35.962 \times \text{mean}) + (.004 \times \text{variance}) + (.235 \times \text{energy}) + (-4.222 \times \text{entropy}) - 383.865$$

$$\text{Glioma} = (38.472 \times \text{mean}) + (.017 \times \text{variance}) + (.203 \times \text{energy}) + (-4.502 \times \text{entropy}) - 444.410$$

$$\text{MS} = (33.271 \times \text{mean}) + (.002 \times \text{variance}) + (.144 \times \text{energy}) + (-3.909 \times \text{entropy}) - 320.829$$

$$\text{SVD} = (34.054 \times \text{mean}) + (.005 \times \text{variance}) + (.184 \times \text{energy}) + (-4.000 \times \text{entropy}) - 339.144$$

Secondly on the higher order statistics with a sensitivity of Glioma, MS and SVD equal to 96.3%, 93.0 and 100.0% respectively on T1+C images using the following equations:

$$\text{Gray matter} = (4206.520 \times \text{SRE}) + (-923.092 \times \text{LRE}) + (.003 \times \text{GLN}) + (5584.293 \times \text{RLN}) + (291.112 \times \text{RP}) + (-1216.916 \times \text{LGRE}) + (-.001 \times \text{SRHGE}) - 4470.826$$

$$\text{White matter} = (4147.347 \times \text{SRE}) + (-917.456 \times \text{LRE}) + (.004 \times \text{GLN}) + (5544.808 \times \text{RLN}) + (307.985 \times \text{RP}) + (-1110.208 \times \text{LGRE}) + (-.001 \times \text{SRHGE}) - 4405.856$$

Glioma = (4174.123× SRE) + (-920.189 × LRE) + (.006× GLN) + (5567.667 × RLN)+ (326.898× RP) +(-1035.968× LGRE) +(-.001× SRHGE) -4484.550

MS = (4128.016× SRE) + (-919.006× LRE) + (.002× GLN) + (5550.632 × RLN)+ (258.220× RP) +(-1090.199× LGRE) +(-.001× SRHGE) -4363.774

SVD = (4211.840× SRE) + (-925.650× LRE) + (.004× GLN) + (5612.975× RLN)+ (320.730× RP) +(-1157.571× LGRE) +(-.001× SRHGE) -4540.311

References

- [1]. Grainger RG, Allison DJ, Baert A. Diagnostic radiology: A text book of medical imaging. sixth Editon. Churchill Livinstone. Bruno Graça Luis Curvo Semedo Miguel Seco Belarmino Gonçalves Cristina Marques Filipe Caseiro-Alves. 2015.
- [2]. Barkhof F, Scheltens P. Imaging of white matter lesions. *Cerebrovascular Diseases*. 2002;13(Suppl. 2):21-30.
- [3]. Eisenberg RL, Johnson NM. *Comprehensive Radiographic Pathology-E-Book*. Elsevier Health Sciences; 2015 Jul 29.
- [4]. Goldenberg MM. Multiple sclerosis review. *Pharmacy and Therapeutics*. 2012 Mar;37(3):175.
- [5]. Li Q, Yang Y, Reis C, Tao T, Li W, Li X, Zhang JH. Cerebral small vessel disease. *Cell transplantation*. 2018 Dec;27(12):1711-22.
- [6]. VN, Pronin IN. *Diagnostic neuroradiology*. 2009
- [7]. Castellano G, Bonilha L, Li LM, Cendes F. Texture analysis of medical images. *Clinical radiology*. 2004 Dec 1;59(12):1061-9.
- [8]. Kassner A, Thornhill RE. Texture analysis: a review of neurologic MR imaging applications. *American Journal of Neuroradiology*. 2010 May 1;31(5):809-16.

Sarah Suliman Mohammed, et. al. "Characterization of White Matter Lesions on Brain Magnetic Resonance Images Using Texture Analysis ." *IOSR Journal of Dental and Medical Sciences (IOSR-JDMS)*, 20(03), 2021, pp. 57-64.